Durham E-Theses

Finite-size Effects in Holography

CHUNLEN, SUPHAKORN

How to cite:

CHUNLEN, SUPHAKORN (2013) *Finite-size Effects in Holography*, Durham theses, Durham University. Available at Durham E-Theses Online: http://etheses.dur.ac.uk/9494/

Use policy

Finite-size Effects in Holography

Suphakorn Chunlen

A thesis presented for the degree of
Doctor of Philosophy

Centre for Particle Theory
Department of Mathematical Sciences
University of Durham
England

December 2013

Dedicated to

Dad, Mum and My Family

Finite-size Effects in Holography

Suphakorn Chunlen

Submitted for the degree of Doctor of Philosophy
December 2013

Abstract

We study holography in the sense of the anti-de Sitter/conformal field theory (AdS/CFT) correspondence, where the field theory lives in a compact space. We first review some aspects of the AdS/CFT duality. We then discuss our work on finite-size corrections to the drag force exerted on a quark in the quark-gluon plasma. Interestingly, the finite-size effects yield a drag force with decreased magnitude, which is opposite to what is seen in many situations with Newtonian fluids. We then turn to meson excitations in a holographic description of $\mathcal{N} = 2$ supersymmetric Yang-Mills theory at finite size. In contrast to other related systems reported in the literature, the first meson excitation is an $SO(4)$ charged scalar meson instead of a vector. Intriguingly, there is also a cross-over between the vector and scalar meson spectra as a function of the system size. Finally, we discuss the extension of this system with a magnetic Kalb-Ramond field. We find intriguing new structure in the phase diagram of the system, and investigate possible causes for an apparent mass gap in the spectrum.

Declaration

The work in this thesis is based on research carried out at the Centre for Particle Theory, the Department of Mathematical Sciences, England. No part of this thesis has been submitted elsewhere for any other degree or qualification and it is all my own work unless referenced to the contrary in the text.

Chapter 1, 2 and 3 are review. Chapter 4 contains my work [1] in collaboration with Kasper Peeters and Marija Zamaklar. Chapter 5 and 6 are substantially based on [2] and [3] respectively, which are my work with Kasper Peeters, Pichet Vanichchapongjaroen and Marija Zamaklar. Some parts in [1–3] have been reproduced in this thesis with the permission of the authors.

Acknowledgements

First and foremost I would like to thank my supervisor Dr. Kasper Peeters. His brilliant academic guidance, useful strategy advice and patience allow this PhD to be real. I have benefited greatly from his wide range of excellent skills, knowledge and reputation.

I would like to thank Dr. Marija Zamaklar, whom I would consider my second supervisor, for a lot of academic discussions with great insight and intuition that help us identify the effective direction of the work.

I also thank Pichet Vanichchapongjaroen, who is one of my best friends, housemates and collaborators, for teaching me lots of useful advanced maths stuff, for being a great knowledge source and for mutually forming an interesting idea generator when we have discussion.

I would like to thank the faculty staffs, postdocs and my fellow friends who taught me and guided me through the academic knowledge and some bits about British culture. Also, thank Dr. Simon Gentle for some suggestions about and proofreading the introduction chapter.

Thank Aj. Phithak Kongsing for the effort of helping me understand Physics in the beginning, and thank all of my teachers since the start of my study.

Thank all of my friends who made my life in Durham much more enjoyable, less depressed, wonderful and feel like home.

I would like to thank the Royal Thai Government for having given me the DPST scholarship since undergraduate.

Thank my family for their unconditional love and support.

Thank Dad Udorn for inspiring me to love science and being patient enough to handle all of my curious and possibly annoying scientific questions about everything

around me when I was young.

Thank Mum Amara for much moral support and the methods to improve my powers of concentration and my efforts that help me through the tough periods of the postgraduate study and the thesis preparation.

Thank Aunt Siraya for a lot of useful high-tech materials and some vital computer skills in the beginning.

Also, thank my brother Jiraphat and my sister Napaluck for such great times in Thailand!

Last but not least, thank my grandparents for putting a lot of hard efforts to support their children's educations among the very discouraging situation. This shaped my parents and somehow it has passed to me.

Contents

List of Figures

List of Tables

Chapter 1

Introduction

In its everyday meaning, holography is a technique used to encode a three-dimensional object in a two-dimensional surface called a hologram. This hologram contains the information of the light rays coming from the object. In the absence of the object, one can reconstruct its three-dimensional image by viewing the hologram in a certain way. Similarly, holography in the original sense of gravitational physics is the way to map the degrees of freedom of a black hole to its horizon via the Bekenstein-Hawking entropy formula. Furthermore, in the anti-de-Sitter/conformal field theory (AdS/CFT) correspondence, which we explain in a later chapter, the term holography means that physics (a gravity theory) in a $(d + 1)$-dimensional spacetime (the bulk) is mapped to the dual physics (a field theory) in the dual d-dimensional spacetime (the boundary). This final meaning is the focus of this thesis.

The concept of the AdS/CFT correspondence was introduced by Maldacena in 1997 [7]. It allows us to compute field theory quantities at strong coupling using the weakly-coupled gravity description. As we have briefly stated, AdS/CFT provides a duality between the gravity and the field theories. The most well-studied example is the duality between type IIB superstring theory in $AdS_5 \times S^5$ spacetime and $\mathcal{N} = 4$ supersymmetric Yang-Mills (SYM) theory on the boundary of AdS_5. Although the AdS/CFT correspondence is still a conjecture, the qualitative results from its application are usually sensible when compared to those from experiments.

String theory was first developed in the late 1960s to understand hadrons. A hadron is a group of quarks glued together by gluons. Both the quarks and the

gluons interact with each other by the strong interaction. However, the attempt to understand hadrons using string theory directly has not yet been successful. The theory of quantum chromodynamics (QCD) is used instead to explain the hadron. In string theory, a one-dimensional object called a string replaces the point-like particle. Different oscillation modes of the string represent different types of particles. The graviton is automatically included in the set of string oscillation modes. This makes the string theory a theory of gravity.

Without incorporating the theory of supersymmetry, a string theory can only describe bosonic particles. As a result, the theory has a tachyon that leads to an instability. A theory with supersymmetry possesses a symmetry between the number of bosons and fermions. The new particles required to allow this symmetry are called superpartners. Including supersymmetry in string theory, one is also able to describe fermions. Such a theory has no tachyon and is renamed a superstring theory. There are five different types of superstring theory depending on the boundary conditions and the GSO projection [8]. These are: type I, type IIA, type IIB, $SO(32)$ heterotic and $E_8 \times E_8$ heterotic string theories. Let us focus on the type IIB superstring theory as this will always be the theory on the gravity side in this thesis. In the Neveu-Schwarz-Neveu-Schwarz (NS-NS) sector, this theory has the field content: $g_{\mu\nu}$ (rank two symmetric traceless tensor, the graviton), $B_{\mu\nu}$ (rank two antisymmetric tensor) and ϕ (scalar, the dilaton). In the Ramond-Ramond (R-R) sector the field content is: $C^{(0)}$ (pseudo-scalar, the axion), $B'_{\mu\nu}$ (rank two antisymmetric tensor) and $C^{(4)}$ (R-R four form). In the low energy limit, type IIB superstring theory becomes type IIB supergravity.

$\mathcal{N} = 4$ SYM theory is a non-Abelian gauge theory with $\mathcal{N} = 4$ supersymmetry, where $\mathcal{N}$ is the number of left-handed Weyl spinor supercharges. A Weyl spinor has two components which are complex numbers, so the total number of real supercharges is $4\mathcal{N}$. The supercharges are anti-commuting generators used to transform bosons/fermions into fermions/bosons. In $3 + 1$-dimensional Minkowski spacetime, $\mathcal{N} = 4$ supersymmetry is the maximally extended supersymmetry with the spin of the particle being no more than one. Therefore, this theory does not contain gravity. $\mathcal{N} = 4$ SYM has fields A_μ (gauge bosons), ϕ^I (real scalar fields), ψ^a_α (chiral fermions)

and $\bar{\psi}_{\dot{\alpha}a}$ (anti-chiral fermions), where $I = 1\ldots 6$, $a = 1\ldots 4$ and $\alpha, \dot{\alpha} = 1, 2$. The supersymmetry restricts the particles to transform in the same representation of the gauge group (the adjoint) and to have the same mass. By gauge invariance, the gauge fields have to be massless, therefore all particles in the theory are massless. The theory has a further global symmetry group $SO(6)_R \sim SU(4)_R$ (also dubbed 'R-symmetry') where the irreducible representations of dimension four and six are associated with the fermions and the scalars, respectively. The theory also has conformal symmetry under the group $SO(2, 4)$ composed of

- Translation ($x^\mu \to x^\mu + a^\mu$, $a^\mu = $ constant)

- Lorentz Transformation ($x^\mu \to \Lambda^\mu_\nu x^\nu$, $\Lambda^\mu_\nu = $ constant and $\eta_{\mu\nu}\Lambda^\mu_\alpha \Lambda^\nu_\beta = \eta_{\alpha\beta}$)

- Dilation ($x^\mu \to kx^\mu$, $k = $ constant)

- Special Conformal Transformation ($x^\mu \to \frac{x^\mu - x_\nu x^\nu b^\mu}{1 - 2b_\sigma x^\sigma + b_\rho b^\rho x_\alpha x^\alpha}$, $b^\mu = $ constant)[1].

Due to the conformal symmetry, $\mathcal{N} = 4$ SYM theory in flat spacetime does not have any scales left to set a phase transition despite a change from zero/finite to finite/zero temperature. However, by the symmetries this theory would be enough to understand "simple" particle physics. This thesis will consider $\mathcal{N} = 4$ SYM theory by the holographic method with additional scales. Specifically, we will consider $\mathcal{N} = 4$ SYM theory on S^3 with a quark mass, and the radius of the S^3 and the quark mass provide scales. Some phase transitions are then expected to appear.

The goal of many high energy physicists in this area is to explain all the properties of the QCD. However, we are still far from achieving that at present. QCD is still hard to analyse theoretically. QCD is a theory explaining the strong nuclear force. It has an $SU(3)$ gauge symmetry. The gauge invariant Lagrangian of QCD is

$$\mathcal{L}_{QCD} = \bar{\psi}\left(i\slashed{D} - m\right)\psi - \frac{1}{2}tr\left(G_{\mu\nu}G^{\mu\nu}\right), \tag{1.0.1}$$

---

[1]The special conformal transformation can also be viewed as the composition of an inversion $x^\mu \to \frac{x^\mu}{x_\nu x^\nu}$ and a translation, so it is simpler to replace the inversion with the special conformal transformation in the bullet.

where $\not{D} \equiv \gamma^\mu D_\mu = \gamma^\mu \left(\partial_\mu - ig A_\mu \right)$, $G_{\mu\nu} \equiv G_{\mu\nu}^{(a)} t_a = \left(\partial_\mu A_\nu^{(a)} - \partial_\nu A_\mu^{(a)} + g f^{abc} A_\mu^{(b)} A_\nu^{(c)} \right) t_a$, $A_\mu = A_\mu^{(a)} t_a$, $t_a = \lambda_a/2$, λ_a are Gell-Mann matrices and γ^μ are the gamma matrices. QCD particles consist of quarks ψ and gluons A_μ associated by the $SU(3)$ colour symmetry. The quarks transform in the fundamental representation while the gluons transform in the adjoint representation of the $SU(3)$ as shown in the following

$$\psi(x) \to U(x)\psi(x),$$
$$A_\mu(x) \to U(x) \left(A_\mu(x) - \frac{i}{g} U^\dagger(x) \partial_\mu U(x) \right) U^\dagger(x), \tag{1.0.2}$$

where $U(x) = \exp\left(-i\theta_a(x) t_a \right)$ and $\theta_a(x)$ are real functions. This yields transformations of the other elements in the Lagrangian as

$$D_\mu \psi(x) \to U(x) D_\mu \psi(x),$$
$$G_{\mu\nu}(x) \to U(x) G_{\mu\nu}(x) U^\dagger(x). \tag{1.0.3}$$

This shows that the QCD Lagrangian is invariant under the gauge transformation. As well as the quark mass m, QCD has an energy scale called Λ_{QCD}. In QCD, Λ_{QCD} is the renormalisation scale at which the coupling becomes order one. This scale is used to characterise the low and high energy regimes. For example, the high energy regime has the energy $E \gg \Lambda_{QCD}$. This arises from the dependence of the coupling parameter on the energy scale, called the running of the coupling parameter. The energy scale dependence is obtained from renormalisation of loop diagrams and is encoded in a form of a beta function

$$\beta(g) \equiv \mu \frac{\partial g}{\partial \mu}, \tag{1.0.4}$$

where g and μ are the coupling parameter and the energy scale, respectively. If the beta function vanishes, it means the theory is scale-invariant. Of course, in 3+1-dimensional spacetime $N = 4$ SYM has the vanishing beta function. For quantum electrodynamics (QED), at one-loop the beta function is positive, so the coupling parameter changes in the same direction as the energy scale. For QCD on the other hand, the one-loop beta function is negative when the number of flavours $N_f \le 16$, so for example at high energy the coupling parameter is small. This leads to a QCD strange property called aymptotic freedom. Actually, QCD has two strange behaviours:

- Confinement: The force between two quarks is stronger when the distance between the two increases. This means we have to use an infinite amount of energy to completely separate the quarks. By experiments, people believe this is true since free quarks have not yet been found in the universe. In general, both quarks and gluons exhibit confinement. They satisfy a rule that can be understood by introducing the colour charges. The statement of confinement is then that the quarks and gluons are always bounded together to form colourless particles.

- Asymptotic Freedom: In the high energy regime, the interaction between quarks and gluons is very weak.

The colour charge is a quantity analogous to the electric charge in electromagnetism. The difference is that colour charge has three different types, i.e. red, green and blue, while there is only one type for the electric charge. The positive/negative electric charges are analogous to, for example, red/anti-red colour charges. The result of combining red, green and blue colour charges together is white or colourless colour charge. Obviously, if we combine for example blue and anti-blue colour charges, we will also have a colourless colour charge. Exploiting asymptotic freedom, one can analyse QCD in the high energy regime using perturbation methods. However, at the low energy regime, the interaction is strongly coupled, so non-perturbative tools are needed. One of the best tools is lattice QCD. Lattice QCD is a non-perturbative approach to compute observables in QCD. It represents spacetime as a lattice of finite points. On the analytical side, this makes the computation of the partition function from the path integral very simple. By contrast, a very large number of configurations and very small lattice spacing are required to obtain the accurate results on the numerical side. As a result, a very large amount of resources and time are required to perform the computation. As the partition function from the path integral is always computable in lattice QCD, in principle one can compute any observable quantities in QCD. However, due to the sign problem[2] in which the

---

[2]In more detail, the sign problem in QCD arises from the factor $\exp(-S)$ in the path integral, where S is the action in the Euclidean signature. Introducing a chemical potential adds an imag-

path integral is over a highly oscillatory function, it is very difficult for lattice QCD to accurately compute observables at low temperature and high density.

Let us consider an alternative approach to the lattice QCD. Since QCD is difficult to examine analytically, it is better to play with a toy model that is quite similar to but is simpler than QCD. Then we will continue to find a way to modify the toy model so that it becomes more and more similar to QCD. The toy model we are considering is $\mathcal{N} = 4$ SYM theory. This theory is similar to QCD; for example both QCD and $\mathcal{N} = 4$ SYM posses non-Abelian gauge symmetries. Furthermore, the $\mathcal{N} = 4$ SYM theory is simpler than the QCD since all particles are massless and in the adjoint representation, whereas in QCD a quark is massive and in the fundamental representation. Also, in $\mathcal{N} = 4$ SYM the particle content is so finely tuned that the beta function vanishes both perturbatively [9, 10] and non-perturbatively [11] while the one in QCD is not. This is the main difference between QCD and $\mathcal{N} = 4$ SYM. Nonetheless, the toy model $\mathcal{N} = 4$ SYM theory is yet not easy to analyse at strong coupling because it is non-perturbative. The AdS/CFT correspondence helps us in this step. From the duality, the $\mathcal{N} = 4$ SYM theory is said to correspond to the type IIB superstring theory in the dual spacetime. As a result of the duality, the coupling constants of the two theories are related by inverse proportion: one theory at strong coupling is dual to the other one at weak coupling and vice versa. One takes this advantage to study the type IIB superstring theory at weak coupling (i.e. at perturbative regimes) and calculate physical quantities and then map them to the dual non-perturbative $\mathcal{N} = 4$ SYM theory.

The first application of the AdS/CFT correspondence we will consider is the drag force in the quark-gluon plasma (QGP). The drag force is the key to explain why the quark-antiquark pair production near the boundary of the QGP does not lead to two antiparallel jets in the collider. Rather, it leads to only one jet in observation. The QGP is a matter state. It has been experimentally produced in the Relativistic

---

inary part to the action causing the factor $\exp(-S)$ to oscillate. Since the Euclidean action is inversely proportional to the temperature, the factor $\exp(-S)$ will oscillate most highly when the temperature is low and/or the chemical potential or the density is high. This leads to the sign problem.

Heavy Ion Collider (RHIC) and in the Large Hadron Collider (LHC) [12]. It consists of quarks and gluons for which the strong interaction is very weak due to the very high energy densities and temperature. The quarks in QGP are deconfined. This means they are not allowed to exist in bound states. The colour charge of the particle in QGP is screened. This is why it is called a plasma. To understand the QGP, one could think about applying the lattice QCD [13–15]. However, the drag force or the energy loss rate are examples of equilibrium rate quantities, so directly extracting those quantities from the partition function obtained in the lattice QCD is impossible [16]. We have already discussed how the $\mathcal{N} = 4$ SYM theory and QCD are quite similar. Using $\mathcal{N} = 4$ SYM theory to study the drag force will give us some qualitative and some quantitative results. Since this process is strongly coupled, directly calculating the quantities in field theory side is very hard to do. By using AdS/CFT duality, one finds it easier to do the calculation.

To make the toy model $\mathcal{N} = 4$ SYM theory more similar to QCD, one can consider adding particles in the fundamental representation to the theory ('quarks'). On the gravity theory side, this is achieved by adding coincident D7-branes to the bulk. By doing this, at least half of the supersymmetry is broken. This results in supersymmetry breaking in the field theory side as well, so the field theory is $\mathcal{N} = 2$ SYM theory. A quark is modelled by a string with one end ending on a D7-brane and the other end ending on a D3-brane. The quark mass is then the shortest length of the string or the shortest distance between the D7-brane and the D3-brane. As long as the quark is massless the field theory is still conformal, and we can use the AdS/CFT correspondence. However, when the quark is massive, it seems that we cannot use the AdS/CFT duality but one claims the correspondence is still true by gauge/gravity duality, a generalisation of AdS/CFT [17].

Gauge/gravity duality is right now the strongest conjecture in the AdS/CFT family. It states that given a quantum theory of gravity in a $d + 1$-dimensional spacetime of which the asymptopia is an AdS spacetime, there is always a gauge theory, which is equivalent to the gravity theory, located in the boundary of the $d + 1$-dimensional spacetime. We know that QCD is a gauge theory. One combines these aspects with an important fact that, even before people invented holography,

't Hooft found a relation between the large N_c expansion of double line Feynman diagrams and the genus expansion in perturbative string theory suggesting that QCD has a string description. Combined with the fact that QCD is well-defined at large N_c, many people have started to believe QCD has a dual holographic description.

Introducing a scale to a theory may result in a phase transition or in some interesting phenomena. In fact, phase transitions do need scales to set the transition points. For example, let us consider water. Without any scale quantities, water molecules are like massless point particles. The interaction between the molecules cannot be determined. Adding scale quantities such as the shape, the atomic and bonding information, we can determine the interaction by, for example, the mass and the charge distribution of the molecule. The bound states between molecules are likely to form solid and liquid states, and there is eventually at least one point beyond which the bonding between the water molecules completely breaks down resulting in a gaseous phase. Let us go back to QCD. Examples of the QCD phase diagram are shown in figure 1.1. In that figure we see there are at least three
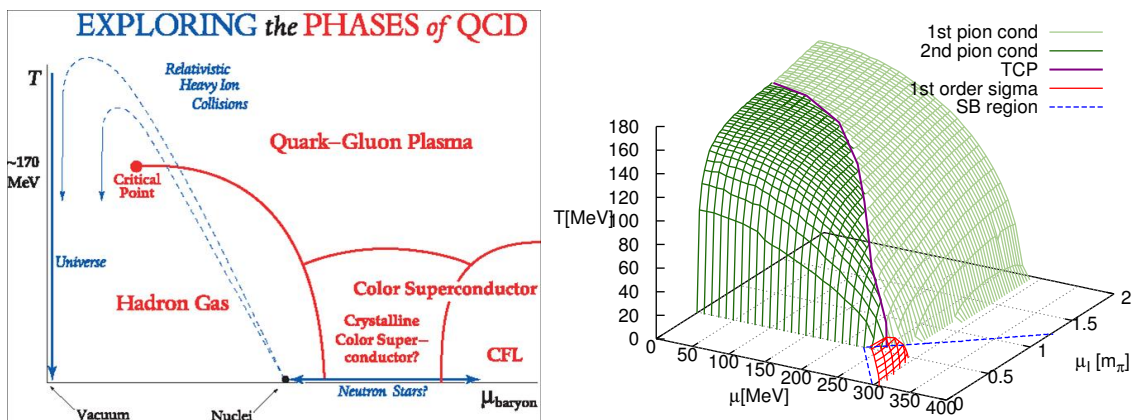
Figure 1.1: Left: [4] A sketch of the phase diagram of QCD, where the vertical and horizontal axes represent temperature and baryon chemical potential, respectively. Right: [5] A QCD phase diagram from extended mean-field approximation, where T, μ and μ_I represent temperature, baryon chemical potential and isospin chemical potential, respectively.

scales: temperature and baryon and isospin chemical potentials. In our work, we will consider adding a finite size to the QCD-like model $\mathcal{N} = 4$ and $\mathcal{N} = 2$ SYM,

and some interesting behaviours are expected to appear. Including a finite size to the system will yield a more realistic result. For example, the quark-gluon plasma in a collider always has a size, which is not infinite. Furthermore, much research on holographic $\mathcal{N} = 2$ SYM theory have been done by, for example, adding finite isospin chemical potential, temperature, magnetic field to the theory. Fewer of them have been done by including a finite size (see [6, 18]), which is our main topic.

In this thesis, we will study various aspects of the holographic $\mathcal{N} = 4$ and $\mathcal{N} = 2$ SYM theories on the compact space S^3. For $\mathcal{N} = 4$ SYM, we study the drag force in QGP with a finite-size correction at finite temperature. For $\mathcal{N} = 2$ SYM, we consider the influence of the isospin chemical potential and the magnetic NS-NS two-form (magnetic Kalb-Ramond) field on the scalar, vector and $SO(4)$ charged scalar meson spectra and new ground states. We find the finite-size correction to the theory in the non-compact case by considering the theory in the planar limit of S^3, yielding the space $\mathbb{R}^3$. Incorporating the effects of finite size leads to many interesting results.

This thesis is organised as follows.

In chapter 2, we review some aspects of basic string theory. We begin this review with a study of the fundamental string action. We then review D-branes and how to get the Dirac-Born-Infeld (DBI) action. We also mention the Wess-Zumino part of the D-brane action. Then we exhibit the duality between open and closed strings which plays an important role in anti-de Sitter/conformal field theory (AdS/CFT) correspondence. We then review the AdS/CFT correspondence in more detail in both non-compact and compact worldvolumes.

In chapter 3, we review the AdS/CFT correspondence with flavour. Following [19, 20], we review how the addition of D7-branes in the gravity theory (type IIB supergravity) is dual to adding quarks to the dual field theory ($\mathcal{N} = 4$ SYM). As we have mentioned, adding the D7-branes breaks at least half of the supersymmetry, and the dual field theory is $\mathcal{N} = 2$ SYM. We review the probe limit of the embedded D7-branes in which the backreaction is safely neglected. We finally review the D7-brane renormalisation which is important in determining the on-shell action and various holographic quantities.

In chapter 4, we present our work [1] in which the holographic drag force was computed in five-dimensional global AdS spacetime. The underlying theory is $\mathcal{N} = 4$ SYM. The drag force is exerted on a holographic quark, which is modelled by a string hanging from the boundary of the AdS spacetime [21–25]. The drag force is computed in a static condition, i.e. the string moving at a constant velocity. We compare the result with the infinite-size limit.

In chapter 5, we present the work in our paper [2]. We consider the influence of the isospin chemical potential in $\mathcal{N} = 2$ SYM theory in the finite size model. We study $\mathcal{N} = 2$ SYM on the compact space S^3 from the dual gravitational perspective, i.e. the type IIB superstring theory on $AdS_5 \times S^5$ with D7-branes embedded in its topological $AdS_5 \times S^3$. The isospin chemical potential is included by turning on a gauge field on the D7-branes. We consider the effect of this chemical potential on the vector, scalar and charged scalar meson spectra and new ground states in $\mathcal{N} = 2$ SYM theory in the compact size case. We compare the result with that of non-compact size.

In chapter 6, we discuss our work in progress [3]. We find the effect of an external magnetic field on $\mathcal{N} = 2$ SYM theory in the compact size model. As in chapter 5, we study the $\mathcal{N} = 2$ SYM via its dual type IIB superstring theory on $AdS_5 \times S^5$ in which the D7-branes are embedded. We add the external magnetic field by turning on a Kalb-Ramond field (or B-field) with a specified ansatz that satisfies the equations of motion from first principles. We analyse the influence of the external magnetic field on the charged scalar, vector and scalar meson spectra and new ground states.

In chapter 7, we summarise what we have done and conclude with the results from chapters 4, 5 and 6 based on the knowledge of chapters 2 and 3. We also propose future plans and some open questions.

Chapter 2

AdS/CFT Correspondence

In this chapter a short introduction of string theory are made followed by some aspects of D-branes. The duality of open and closed strings are mentioned leading to a main idea of AdS/CFT correspondence. It then discusses some materials of AdS/CFT correspondence.

2.1 A Short Introduction to Basic String Theory

String theory was formulated in 1960s with the purpose to explain the strong nuclear force. However, as a candidate of the theory of the strong interaction it was abandon due to the existence of the graviton, and then it turns out to be a theory of gravity. The string theory models the particle by a string with a finite length. The string is described by the action

$$S = -T \int d\tau d\sigma \sqrt{-\det\left(G_{\mu\nu}\frac{\partial X^\mu}{\partial \sigma^a}\frac{\partial X^\nu}{\partial \sigma^b}\right)}, \qquad (2.1.1)$$

where $T = 1/(2\pi\alpha')$ is the string tension, X^μ is the spacetime coordinates, $\sigma^a = (\tau, \sigma)$ is the world-sheet coordinates, and $G_{\mu\nu}$ is the spacetime metric. This action is called Nambu-Goto action. This action has a good interpretation because it indicates the extremal area of the string world-sheet. However, the square root in the action serves the difficulty in its quantisation. This problem is eliminated by using an equivalent action. This action is Polyakov action giving the same equations

of motion as Nambu-Goto one's. The Polyakov action is [26]

$$S_{\text{Polyakov}} = -\frac{T}{2} \int d^2\sigma G_{\mu\nu} \sqrt{-h} h^{ab} \partial_a X^\mu \partial_b X^\nu, \tag{2.1.2}$$

where h_{ab} is a world-sheet metric, $h^{ab} = (h^{-1})_{ab}$ and $h = \det(h_{ab})$. To convince that this action is equivalent to Nambu-Goto action, one shows this by using the equation of motion for h_{ab}

$$\begin{aligned}
T_{ab} &= -\frac{2}{T\sqrt{-h}} \frac{\delta S_{\text{Polyakov}}}{\delta h^{ab}} \\
&= G_{\mu\nu} \partial_a X^\mu \partial_b X^\nu - \frac{1}{2} G_{\mu\nu} h_{ab} h^{cd} \partial_c X^\mu \partial_d X^\nu = 0
\end{aligned} \tag{2.1.3}$$

or

$$G_{\mu\nu} \partial_a X^\mu \partial_b X^\nu = \frac{1}{2} G_{\mu\nu} h_{ab} h^{cd} \partial_c X^\mu \partial_d X^\nu. \tag{2.1.4}$$

Taking the square root of minus determinant of both two sides of (2.1.4), one proves the Nambu-Goto and Polyakov actions are equivalent by

$$\sqrt{-\det\left(G_{\mu\nu} \partial_a X^\mu \partial_b X^\nu\right)} = \frac{1}{2} G_{\mu\nu} \sqrt{-h} h^{ab} \partial_a X^\mu \partial_b X^\nu. \tag{2.1.5}$$

The Polyakov action has conformal invariance in $h_{ab} \to e^\phi h_{ab}$ as the energy-momentum tensor in (2.1.3) vanishes implying it is traceless. Then we are free to choose the world-sheet metric to be flat $h_{ab} = \eta_{ab}$, so the Polyakov action is simplified

$$S_{\text{Polyakov}} = -\frac{T}{2} \int d^2\sigma G_{\mu\nu} \partial_a X^\mu \partial^a X^\nu. \tag{2.1.6}$$

At quantum level, the theory posses tachyons which shows instability of the theory. To remove tachyons, one imposes supersymmetry. This results the fermion is therefore included into the action

$$S = -\frac{T}{2} \int d^2\sigma G_{\mu\nu} \left(\partial_a X^\mu \partial^a X^\nu + \bar\psi^\mu \rho^a \partial_a \psi^\nu\right). \tag{2.1.7}$$

This action is in Ramond-Neveu-Schwarz (RNS) formalism. ρ^a in the action is the two-dimensional Dirac matrices, satisfying the algebra

$$\{\rho^a, \rho^b\} = 2\eta^{ab}. \tag{2.1.8}$$

The spinor ψ^μ in the action represents the fermionic field, satisfying the anti-commutation relation

$$\{\psi^\mu, \psi^\nu\} = 0. \tag{2.1.9}$$

The conformal transformation $h_{ab} \rightarrow e^\phi h_{ab}$ in general provides anomaly in quantum theory. One treats this by fixing the spacetime dimension D to be ten. The action (2.1.7) yields the equations of motion

$$\partial_a \partial^a X^\mu = 0, \tag{2.1.10}$$

$$\rho^a \partial_a \psi^\mu = 0, \tag{2.1.11}$$

where the first one is for the bosonic part and the second one is for the fermionic part. One views the equation for the bosonic part as a wave equation

$$\left(\frac{\partial^2}{\partial \sigma^2} - \frac{\partial^2}{\partial \tau^2} \right) X^\mu = 0. \tag{2.1.12}$$

In general, the string has finite length. One has to deal with the boundary conditions to complete the variational problem. When we vary the action in (2.1.7) with $X^\mu \rightarrow X^\mu + \delta X^\mu$, it results the change in the action by

$$\delta S = T \int d\tau d\sigma \partial_a \left(G_{\mu\nu} \eta^{ab} \partial_b X^\nu \right) \delta X^\mu - T \int d\tau \left[G_{\mu\nu} \frac{\partial X^\mu}{\partial \sigma} \delta X^\nu \right]_{\sigma=\sigma_1}^{\sigma=\sigma_2}. \tag{2.1.13}$$

To satisfy the variational principle, each term on the right hand side has to vanish independently. The first term yields the equations of motion of the string. The second term is the boundary term. For simplicity let us choose the boundary points of the string as $\sigma_1 = 0$ and $\sigma_2 = \pi$. For the second term to be zero, there are a few cases yielding that. Those cases are

- Imposing the periodic boundary conditions $X^\mu(\tau, \sigma) = X^\mu(\tau, \sigma + \pi)$,

- Applying the the Neumann boundary conditions $\frac{\partial X^\mu}{\partial \sigma}\big|_{\sigma=0} = \frac{\partial X^\mu}{\partial \sigma}\big|_{\sigma=\pi} = 0$ for all μ's,

- Using the Dirichlet boundary conditions $\delta X^\mu = 0$, and $X^\mu(\tau, 0) = X^\mu_{\sigma_0} =$ constant and $X^\mu(\tau, \pi) = X^\mu_{\sigma_\pi} =$ constant for $\mu = 1, \ldots, D-p-1$, and applying the Neumann boundary conditions for the remaining $p+1$ coordinates.

The first case is the case for the closed string. The second and the third cases are the cases for the open strings. For the third case, $X^\mu_{\sigma_0}$ and $X^\mu_{\sigma_\pi}$ also indicate the position of Dp-branes or D-branes with p spatial dimensions.

2.2 D-branes

D-branes are not only hyperplanes in which the open strings must end but also physical objects having their own properties. In superstring theory, D-branes are electric and magnetic sources of Ramond-Ramond (R-R) differential forms. More specifically, the Dp-brane carries an R-R charge by acting as a source of a $(p+1)$-form gauge field. The D-branes are stable in superstring theory because they carry R-R charges that are conserved. However, not all D-branes are stable in a particular one of the type II superstring theory. For type IIA superstring theory, the D-branes with even spatial dimensions are stable i.e. D0-, D2-, D4-, D6- and D8-branes. For type IIB superstring theory the D-branes with odd spatial dimensions are stable i.e. D(-1)-, D1-, D3-, D5- and D7-branes. D(-1)-branes are localised in both space and time; they are also called D-instantons. For D9-branes, they must fill all ten dimensional spacetime; with this fact, they cannot carry conserved charges, so D9-branes are unstable in both type IIA and IIB superstring theory. In general, Dp-branes or particularly their world volumes can be electrically coupled to $(p+1)$-form gauge fields. One shows this by the integral of the $(p+1)$-form gauge field over the world volume of the Dp-brane

$$S = Q_p \int A_{p+1} = \frac{Q_p}{[(p+1)!]^2} \int d^{p+1}\sigma \sqrt{-g} A_{\mu_1 \ldots \mu_{p+1}} \frac{\partial x^{\mu_1}}{\partial \sigma^{a_0}} \ldots \frac{\partial x^{\mu_{p+1}}}{\partial \sigma^{a_p}} \epsilon^{a_1 \ldots a_p}, \quad (2.2.14)$$

where g is the determinant of the pull-back metric on the Dp-brane and Q_p is the Dp-brane charge. From the geometry point of view, in D-dimensional spacetime we know that a Dp-brane can be surrounded by an S^{D-p-2}. The charge of the Dp-brane is then described by the Gauss' law integrating over a hypersurface surrounding the Dp-brane

$$Q_p = \int_{S^{D-p-2}} F, \quad (2.2.15)$$

where F is the $(D-p-2)$-form field determined by both $F = *dA_{p+1}$ and $F = dA_{D-p-3}$. For the first one or $F = *dA_{p+1}$, it means the Dp-brane carry the electric charge under the $(p+1)$-form gauge field. For the second, it says the Dp-brane carry the magnetic charge under the $(D-p-3)$-form gauge field. The Dp-brane and the Dq-brane are said to be magnetic dual if one carries the electric/magnetic charge under the a form gauge field and the other one carry magnetic/electric charge under

the same form gauge field. Mathematically, it is $p + 1 = D - q - 3$ or $p + q = D - 4$. In ten dimensional spacetime, Dp-branes are magnetic dual to D$(6-p)$-branes. Now we will consider only the case of ten dimensions. Given a Ramond-Ramond (R-R) p-form gauge field, the Dp brane is electrically coupled to this gauge field and has an electric charge Q_p while the D$(6-p)$ brane is magnetically coupled and has a magnetic charge Q_{6-p}. Their charges satisfy the Dirac quantisation condition in a generalised version

$$Q_p Q_{6-p} = 2\pi n, \quad n \in \mathbb{Z}. \tag{2.2.16}$$

In type II superstring theories, it turns out that there are only R-R p-form gauge fields in which $p = 0, 1, 2, 3, 4$. For this reason, the Dp-branes with $p \leq 3$ have electric charges under the R-R gauge fields, and the Dp-branes with $p \geq 4$ have magnetic charges. D-branes also have tension. The tension of a D-brane is roughly its energy per unit volume. One determines the tension T_{Dp} of a Dp-brane as a recurrence relation [27, 28]

$$T_{Dp} = \frac{T_{D(p-1)}}{2\pi\sqrt{\alpha'}}, \tag{2.2.17}$$

given that the tension of D-string or D1-brane is related to the fundamental string tension by

$$T_{D1} = \frac{T}{g_s} = \frac{1}{2\pi g_s \alpha'}. \tag{2.2.18}$$

By analogy with the action of the string, the Dp-brane action would be simply guessed as the minimisation of its world-volume

$$S_{Dp} = -T_{Dp} \int d^{p+1}\xi \sqrt{-\det(g_{ab})}, \tag{2.2.19}$$

where $g_{ab} = G_{\mu\nu} \frac{\partial X^\mu}{\partial \sigma^a} \frac{\partial X^\nu}{\partial \sigma^b}$ is the induced metric on the Dp-brane. Unlike the string, this is not complete yet; the D-brane possesses more degrees of freedom. For example, the D-brane can have open strings ended on it, so it has open string degrees of freedom. The D-brane action that includes the open string degrees of freedom in arbitrary energy levels is still unknown. However, at low enough energy $E \ll 1/\alpha'^2$ or in other words, at the string length near zero, one found the open string degrees of freedom on the D-brane is described by the $U(1)$ gauge field living on the D-brane. Including this into the action, one has a more generalised version of the D-brane

action

$$S_{Dp} = -T_{Dp} \int d^{p+1}\xi \, e^{-\Phi} \sqrt{-\det(P[G]_{ab} + kF_{ab})}, \qquad (2.2.20)$$

where k is a constant to correct the dimension and $F_{ab} = \partial_a A_b - \partial_b A_a$ is the field strength of the $U(1)$ gauge field. Note that there is the dependence of $e^{-\Phi}$ since it is the open string tree level action. This determines the string coupling constant, $g_s = e^{<\Phi>}$. Next, let us consider the combination of Neveu-Schwarz-Neveu-Schwarz (NS-NS) 2-form field or the closed string field $B_{\mu\nu}$ and the $U(1)$ gauge field or the open string field A_μ in the string action [27]

$$Q = \frac{i}{2\pi\alpha'} \int_{\mathcal{M}} B + i \int_{\partial\mathcal{M}} A. \qquad (2.2.21)$$

This quantity is invariant under the gauge transformation

$$A_\mu \to A_\mu + \partial_\mu \lambda, \qquad (2.2.22)$$

and also the tensor gauge transformation

$$B_{\mu\nu} \to B_{\mu\nu} + \partial_\mu \zeta_\nu - \partial_\nu \zeta_\mu,$$
$$A_\mu \to A_\mu - \frac{\zeta_\mu}{2\pi\alpha'}. \qquad (2.2.23)$$

Note that the two transformations in (2.2.23) have to be done together; otherwise (2.2.21) will not be invariant. Obviously, the action (2.2.20) is invariant under the gauge transformation (2.2.22). However, if we apply the tensor gauge transformation to the action, the term F_{ab} will change to $F_{ab} - (\partial_a \zeta_b - \partial_b \zeta_a)/(2\pi\alpha')$ that leaves the action not invariant. There is a situation that we cannot neglect the background NS-NS 2-form B field, which is transformed under the tensor gauge transformation (2.2.23). As a result, the D-brane action should include the dependence of the B-field and should be invariant under the tensor gauge transformation. Since the B-field has the same length dimension as the metric tensor, it is natural to change G to $G + B$ in the D-brane action in (2.2.20). Considering both the transformations in (2.2.22) and (2.2.23), we then find that the combination

$$B_{\mu\nu} + 2\pi\alpha' F_{\mu\nu} \qquad (2.2.24)$$

is invariant under the both transformations. This determines the constant k in (2.2.20). Therefore, the D-brane action is changed to

$$S_{Dp} = -T_{Dp} \int d^{p+1}\xi \, e^{-\Phi} \sqrt{-\det(P[G+B]_{ab} + 2\pi\alpha' F_{ab})}. \qquad (2.2.25)$$

This action is call Dirac-Born-Infeld (DBI) action. We have mentioned that the D-brane can be coupled to R-R gauge fields; the dependence of those fields also needs to be included in the action. One finds that it is contributed to the D-brane action in the form of the Chern-Simons term

$$S_{CS} = Q_p \int \left[\left(\bigoplus_q C_q \right) \wedge e^{B+2\pi\alpha'F} \right]_{\text{choose only }(p+1)\text{-form}}, \qquad (2.2.26)$$

where C_q is the R-R q-form. The D-brane action then has two parts which are the Dirac-Born-Infeld part and the Chern-Simons (or Wess-Zumino) part. The action is written as

$$S_{Dp} = S_{DBI} + S_{WZ}, \qquad (2.2.27)$$

where

$$S_{DBI} = -T_{Dp} \int d^{p+1}\xi\, e^{-\phi} \sqrt{-\det\left(P[G+B]_{ab} + 2\pi\alpha'F_{ab}\right)}, \qquad (2.2.28)$$

$$S_{WZ} = Q_p \int \left[\left(\bigoplus_q C_q \right) \wedge e^{B+2\pi\alpha'F} \right]_{\text{choose only }(p+1)\text{-form}}, \qquad (2.2.29)$$

with $Q_p = T_{Dp}$ [28]. For multiple D-branes, the generalisation is quite straightforward. The open strings have more degrees of freedom i.e. it can also end on two different D-branes. The gauge fields associated to the open string degrees of freedom in the low energy limit are then turned to non-Abelian gauge fields. The generalised version of the action for multiple D-branes is

$$S_{DBI} = -T_{Dp} \int d^{p+1}\xi\, e^{-\phi} Str \sqrt{-\det\left(P[G+B]_{ab} + 2\pi\alpha'F_{ab}\right)}, \qquad (2.2.30)$$

$$S_{WZ} = T_{Dp} \int \left[\left(\bigoplus_q C_q \right) \wedge tr\left(e^{B+2\pi\alpha'F} \right) \right]_{\text{choose only }(p+1)\text{-form}}, \qquad (2.2.31)$$

where Str is a symmetrised trace having a property

$$Str(A_1 A_2 \ldots A_N) = \frac{1}{N!} tr\left(\sum_{i_1,i_2,\ldots,i_N=1}^{N} |\epsilon_{i_1 i_2 \ldots i_N}| A_{i_1} A_{i_2} \ldots A_{i_N} \right). \qquad (2.2.32)$$

The DBI action with the symmetrised trace prescription was introduced in [29]. This action looks intuitively right, however, it is correct up to the fourth order of F as the action starts to deviate from open string computations at the order F^6 [30].

2.3 Duality between Open and Closed Strings

The fact that the open strings must end on D-branes makes us always consider open strings and D-branes at the same time. To see the open and closed string duality, let us consider an open string ended on two different D-branes as illustrated in figure 2.1. When the open string swifts and makes a span of a cylindrical-like shape
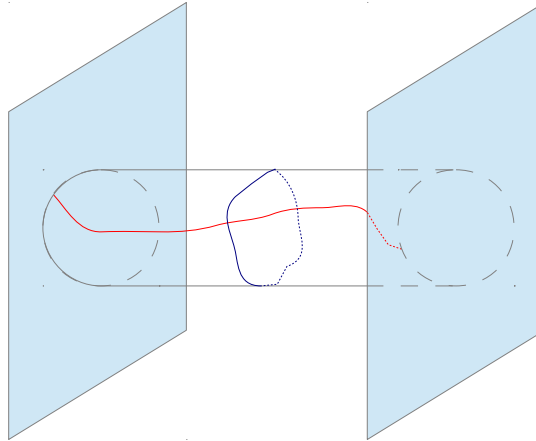
Figure 2.1: A diagram shows an example of the open and closed string duality, where the two cyan parallelograms depict the D-branes and the red and the blue curves are an open string and a closed string respectively. When the open string, connected between the two D-branes, sweeps around to form the cylindrical(-like) world sheet, this world sheet can also be seen as the closed string moving from one D-brane to the other. The converse is also true if we start from the closed string.

as in the right figure, one can think of an equivalent situation that the D-branes are exchanging a closed string. Both situations yield the same picture. This is an example of the duality between open and closed strings. This leads to the AdS/CFT correspondence.

2.4 AdS/CFT Correspondence

In 1997, Maldacena proposed a conjecture that relates the string theory on an Anti-de-Sitter (AdS) spacetime with the conformal field theory on the corresponding spacetime [7]. For example, the type IIB superstring theory on $AdS_5 \times S^5$ was

shown to correspond to $\mathcal{N} = 4$ supersymmetric Yang-Mills theory on the corresponding four dimensional spacetime. Later in 1998, the more concrete version of the correspondence was published [17]. These state the dictionary of the correspondence

$$Z_{\text{string theory}} = Z_{CFT}, \tag{2.4.33}$$

where Z is the partition function. Based on D3-branes, the open and closed string duality (see figure 2.1 for an illustration) is able to explain the Maldacena conjecture [31]. At low energy, the open string sector of a stack of N_c D3-branes has the symmetry $U(N_c) = SU(N_c) \times U(1)$. One can factor out the $U(1)$ as it associates to the centre of mass motion of the D3-branes. The background theory is the superstring theory in type IIB; it has 32 supercharges. The supersymmetry on the D3-branes is only half of the one on the background theory, so the number of supercharges on the D3-branes is 16. The number of supercharges and the number of degrees of freedom of the transverse fluctuation of the D3-branes match with ones of the $\mathcal{N} = 4$ super-Yang-Mills (SYM) theory. Therefore the open string sector at low energy of the N_c D3-branes is the $\mathcal{N} = 4$ SYM theory. For the closed string sector, let us consider the D3-brane metric in ten dimensional spacetime [32]

$$ds^2 = H_3(r)^{-\frac{1}{2}} \left(-dt^2 + d\vec{x}^2\right) + H_3(r)^{\frac{1}{2}} \left(dr^2 + r^2 d\Omega_5^2\right), \tag{2.4.34}$$

where $H_3(r) = 1 + \frac{R^4}{r^4}$, $R^4 = 4\pi g_s N_c \alpha'^2$ and $\vec{x}$ represents (x^1, x^2, x^3) of $\mathbb{R}^3$. The low energy limit of the theory can be achieved by taking the zero string length limit $\alpha' \to 0$ while keeping r/α' fixed [7]. As a result, the geometry is effectively viewed as a near horizon limit $r \ll R$ so that the factor '1' in $H_3(r)$ can be neglected and the metric is

$$ds^2 = \frac{r^2}{R^2} \left(-dt^2 + d\vec{x}^2\right) + \frac{R^2}{r^2} \left(dr^2 + r^2 d\Omega_5^2\right). \tag{2.4.35}$$

This metric describes the geometry of $AdS_5 \times S^5$ in Poincaré coordinates with the radii of AdS_5 and S^5 being equal. The AdS_5 and S^5 geometries have the isometry groups $SO(2,4)$ and $SO(6)$ respectively, and so do their metrics. Furthermore, we know that the D3-brane world volume is electrically and magnetically coupled to the R-R 4-form gauge field. The 5-form field strength has to be self-dual with the

form of

$$F_5 = f_5(r)(1 + *)dr \wedge dt \wedge dx^1 \wedge dx^2 \wedge dx^3, \tag{2.4.36}$$

where $*$ is the Hodge dual operator in (9+1)-dimensional spacetime and $f_5(r) = \frac{\partial}{\partial_r} H_3(r)^{-1}$. This five-form satisfies

$$\int_{S^5} F_5 = N_c. \tag{2.4.37}$$

Now that we are considering the D3-branes, so the theory associated with them is type IIB superstring theory. At the near-horizon limit of the D3-branes, the string theory approaches the low-energy limit that is the type IIB supergravity (SUGRA). The open string description of the stack of N_c D3-branes at low energy is then the type IIB SUGRA.

The strongest form of AdS/CFT conjecture is that string theories compactified on the AdS spacetime always have their dual field theories. It is very hard to test the statement in general as we still do not know how to quantise the string theory in a curved spacetime with R-R fields [33]. As we have mentioned, an example of the correspondence is the duality between the type IIB superstring theory in the Poincaré patch of $AdS_5 \times S^5$ spacetime and the $\mathcal{N} = 4$ $SU(N_c)$ SYM theory on $\mathbb{R}_t \times \mathbb{R}^3$. To make it more simple to test, the weaker form states the correspondence with the restriction, the 't Hooft limit. This takes the value $N_c \to \infty$ while keeping the 't Hooft constant $\lambda = g_{YM}^2 N_c$ fixed. In this case, the gravity side is the string theory in semiclassical limit where the coupling $g_s \to 0$. g_s is the string coupling constant related to the Yang-Mills coupling constant by $g_{YM}^2 = 2\pi g_s$. In the field theory side, the large N_c limit restricts all the non-planar diagram contributions. In even more weaker form, the correspondence is considered in the limit that $\lambda \to \infty$. In this limit, the gravity side is reduced from the type IIB superstring theory to the type IIB SUGRA where the inverse string tension $\alpha' \to 0$, and the field theory side is strongly coupled $\mathcal{N} = 4$ $SU(N_c)$ SYM theory. In our work, only this form of the correspondence will be considered.

2.4.1 The Dictionary of the AdS/CFT Correspondence

It is obvious that the theory in the gravity side lives in the spacetime with the dimensions higher than the spacetime in which the theory in the field theory side lives by one. The additional dimension in the gravity side will play an important role for the mapping between the two theory. Indeed the additional dimension is the radial direction which makes the correspondence holographic [34]. In order to see how the radial direction is related to the field theory side, let us consider the action of a free massless scalar in $3 + 1$-dimensions

$$S = \int d^4x (\partial\phi)^2. \tag{2.4.38}$$

This action is invariant under the transformations

$$\begin{aligned} x &\to e^\alpha x, \\ \phi &\to e^{-\alpha}\phi, \end{aligned} \tag{2.4.39}$$

where α is a real number. We know that the coordinate x has the dimension of length and ϕ has the dimension of energy. This transformation is the dilatation and, therefore, the energy scaling. Applying the transformation to the AdS_5 part, which is also the coordinates of the field theory side, of (2.4.35), we have

$$ds^2 = \frac{r^2 e^{2\alpha}}{R^2}\left(-dt^2 + d\vec{x}^2\right) + \frac{R^2}{r^2}\left(dr^2 + r^2 d\Omega_5^2\right). \tag{2.4.40}$$

As we have mentioned, the metric (2.4.35) has the isometry $SO(2,4)$ which is the conformal group in $3 + 1$-dimension where the dilatation is one of its elements. Therefore, we expect (2.4.35) to be invariant under the dilatation transformation. This automatically requires the radial coordinate to be transformed as

$$r \to e^{-\alpha}r \tag{2.4.41}$$

to preserve the invariance. Thus, it is sensible to think that the additional dimension in the gravity side corresponds to the energy scale in the field theory side.

One has further developed the AdS/CFT correspondence to establish a map between the fields of SUGRA in the isomorphic representation of the $SO(6)$ global symmetry and the $\mathcal{N} = 4$ SYM gauge invariant operators in a particular irreducible

representation of the $SU(4)$ R-symmetry [17, 35]. The five-dimensional SUGRA fields are results of the Kaluza-Klein reduction on the internal five-sphere S^5. To simply visualise the field-operator map, let us consider the action of a massive scalar field in the AdS_{d+1} spacetime [33, 36]

$$S = \int d^d x \, dr \, \sqrt{-G} \left(G^{\mu\nu} \partial_\mu \phi \, \partial_\nu \phi - m^2 \phi^2 \right), \tag{2.4.42}$$

where m is the mass of the scalar field and r is the radial coordinate of the AdS_{d+1} spacetime. The corresponding equation of motion has the solution in the asymptotic (large-r) form as

$$\phi(r, x) = r^{\Delta - d} \phi_0(x) + r^{-\Delta} \langle \mathcal{O}(x) \rangle \tag{2.4.43}$$

with

$$\Delta = \frac{d}{2} + \sqrt{\frac{d^2}{4} + m^2 R^2}, \tag{2.4.44}$$

where R is the AdS radius. Under the dilatation transformation, the supergravity field $\phi(u, x)$ is invariant, so the fields $\phi_0(x)$ and $\langle \mathcal{O}(x) \rangle$ need to have the length dimensions $4 - \Delta$ and Δ respectively. According to [35], the fields $\phi_0(x)$ and $\langle \mathcal{O}(x) \rangle$ may be recognised as respectively the source and the vacuum expectation value (vev) of the gauge theory operator $\mathcal{O}$ in the dual field theory. Note that

$$\int d^d x \, \phi_0(x) \langle \mathcal{O}(x) \rangle \tag{2.4.45}$$

is invariant under the global symmetry of the group $SO(2, 4)$ [36]. The exact form of the AdS/CFT correspondence may be proposed as [17, 35]

$$\langle e^{\int d^d x \, \phi_0(x) \langle \mathcal{O}(x) \rangle} \rangle_{\text{CFT}} = \mathcal{Z}_{\text{SUGRA}} \left[\phi_0(x) \right], \tag{2.4.46}$$

in which

$$\mathcal{Z}_{\text{SUGRA}} \left[\phi_0(x) \right] = \lim_{\epsilon \to 0} \mathcal{Z}_{\text{SUGRA}} \left[\phi_0(1/\epsilon, x) = \epsilon^{d - \Delta} \phi_0(x) \right]. \tag{2.4.47}$$

This means the generating functional of the gauge invariant operators in the conformal field theory coincides with the tree level diagrams' generating functional in supergravity.

The correspondence equation (2.4.46) has been checked by comparing correlation functions of $\mathcal{N} = 4$ quantum field theory with classical correlation functions on

the AdS_d spacetime. In gravity side, this can be done only at the large 't Hooft coupling $\lambda \to \infty$ due to the validity of the tree level approximation. Therefore, using the formula from the gravity side will always yield the correspondence where the field theory is strongly coupled. Also, the direct comparison is not possible if the correlation functions neither satisfy non-renormalisation theorem nor depend on the coupling [33]. This applies to the two- and three-point functions of 1/2 BPS operators in particular [37, 38].

For finite temperature, the geometry of the gravity theory dual to the $\mathcal{N} = 4$ SYM at finite temperature is AdS_5-Schwarzschild$\times S^5$ [39], where the metric is

$$ds^2 = -\left(\frac{r^2}{R^2} - \frac{8GM}{3\pi r^2}\right)dt^2 + \frac{dr^2}{\frac{r^2}{R^2} - \frac{8GM}{3\pi r^2}} + \frac{r^2}{R^2}d\vec{x}^2 + R^2 d\Omega_5^2. \tag{2.4.48}$$

Here M is the mass of the black hole and G is the Newton constant. The black hole has the Hawking temperature

$$T = R^{1/2}\left(\frac{8GM}{3\pi}\right)^{1/4}, \tag{2.4.49}$$

which can be obtained by Wick rotation to Euclidean time and then compactifying the time direction of which the period is recognised as $1/T$. The Hawking temperature and the entropy of the black hole are identified with the temperature and the entropy of the dual field theory respectively [39, 40].

For compact spacetime, we simply generalise the $AdS_5 \times S^5$ in (2.4.35), which is in Poincaré coordinates, to the global $AdS_5 \times S^5$ where the metric is

$$ds^2 = -\left(1 + \frac{r^2}{R^2}\right)dt^2 + \frac{dr^2}{1 + \frac{r^2}{R^2}} + r^2 d\Omega_3^2 + R^2 d\Omega_5^2. \tag{2.4.50}$$

For the finite temperature version, applying Wick rotation to (2.4.50) can be done, but it is not thermodynamically preferred when the temperature increases beyond a certain value called Hawking-Page temperature [41]. The phase transition is occurred and the preferred geometry is AdS_5-Schwarzschild$\times S^5$ [39], where the metric is

$$ds^2 = -\left(1 + \frac{r^2}{R^2} - \frac{8GM}{3\pi r^2}\right)dt^2 + \frac{dr^2}{1 + \frac{r^2}{R^2} - \frac{8GM}{3\pi r^2}} + r^2 d\Omega_3^2 + R^2 d\Omega_5^2. \tag{2.4.51}$$

Note that the geometry of the AdS_5 at the asymptotic region ($r \to \infty$) is $\mathbb{R}_t \times S^3$. Although the global $AdS_5 \times S^5$ does not arise from any near-horizon configurations of

any D-branes, it is believed that the gravity theory living in this geometry will have its dual field theory living in the boundary. We also presume that the dictionary (2.4.46) is still valid in the compact spacetime.

Chapter 3

AdS/CFT with Flavour

Originally, the AdS/CFT correspondence does not have the fields that transforms in the fundamental representation. All the fields are transformed in the adjoint one. This should not be a problem when we consider a system that has only, for example, gluons. However, the QCD system actually has both gluons and quarks. The quark transforms in the fundamental representation. Therefore, using the original AdS/CFT correspondence to explain a QCD-like system, having quarks, is obviously unsuccessful. Fortunately, one has been modified the AdS/CFT correspondence so that the fields in the fundamental representation involves [19]. This is very useful when describing the system in strongly coupled regimes, in which the perturbative approach does not work.

3.1 Adding the Flavour

In the gauge/gravity duality, the most simple way to have fields transformed in the fundamental representation is to include the D7-branes in the gravity side [19,42,43]. We will denote N_f as the number of the D7-branes embedded in the spacetime. For the stacks of N_f D7-branes and N_c D3-branes, a stable choice is that they are embedded in the directions as shown in the table 3.1. This brane embedding has $SO(4) \times SO(2)$ symmetry in the directions normal to the D3-branes. The $SO(4)$ and $SO(2)$ are isometries of the rotations in $\{x^4, x^5, x^6, x^7\}$ and $\{x^8, x^9\}$ respectively. For the supersymmetry, at least one-half of the supersymmetry will be broken by

	x^0 or t	x^1	x^2	x^3	x^4	x^5	x^6	x^7	x^8	x^9
D3	$\times$	$\times$	$\times$	$\times$						
D7	$\times$	$\times$	$\times$	$\times$	$\times$	$\times$	$\times$	$\times$		

Table 3.1: The embedding directions of the D3- and D7-branes in (9+1)-dimensional Minkowski spacetime, where x^0 and the other x^i's denote the temporal and spatial directions respectively.

adding D-branes [20]. In general, adding D-branes will exactly preserve half of the supersymmetry if one D-brane fills in four or eight directions in which the other does not extend [27, 44, 45]. Therefore, the embedding in the table 3.1 preserves one-fourth, where the first one-half is from adding the D3-branes and the second one-half is the result of adding the D7-branes, of the total supersymmetry of the type IIB superstring theory, so the total number of real supercharges is $4\mathcal{N} = 8$. Adding the D7-branes allows two more types of open strings i.e. the open strings ending on only D7-branes (7-7 strings) and the open strings ending on both D3- and D7-branes (3-7 strings). The 3-7 strings generate the $\mathcal{N} = 2$ hypermultiplets in addition to the multiplet of the $\mathcal{N} = 4$ SYM from the 3-3 strings. The dual field theory is then expected to be $\mathcal{N} = 2$ SYM. For the 7-7 strings, we can neglect their effects in our works since, in the large N_c and short string length $\alpha' \to 0$ limits with fixed 't Hooft coupling $\lambda = g_{YM}^2 N_c$ and N_f, the 7-7 strings decouple from the system and do not have any interactions with the 3-3 and 3-7 strings [33]. The separation between the D3- and D7-branes determines the minimum length or the energy of the 3-7 strings. Let's say the separation is L; one finds that the mass of the $\mathcal{N} = 2$ hypermultiplet is related to the distance by $m_q = L/(2\pi\alpha')$ [44].

3.2 The D7-brane Probe Limit

We will look at the low-energy closed string description of the AdS/CFT correspondence with the additional D7-branes. In the original AdS/CFT correspondence, the gravity side of the low-energy closed string description, which is supergravity, has the D3-branes as sources for the metric and the self-dual five-form, F_5. Now with

the D7-branes added in, the metric will have these branes as additional sources. The D7-branes also source the axion-dilaton or a (pseudo-)scalar field. Unfortunately, the supergravity solution for the D3/D7 brane intersection for general values of N_c and N_f is still unknown. However, Considering the case $N_f \ll N_c$, one can neglect the effect of the D7-branes to the supergravity solution [19, 44]. For example, for the case $N_c \to \infty$ and just a few N_f, the D3-branes will dominantly source the metric, and the effect of the D7-branes to the metric is then like a drop in the ocean. Let us consider this more precisely. The D3-branes source the five-form and the metric with a strength $g_s N_c$. The axion-dilaton and also the metric are sourced by the D7-branes with a strength $g_s N_f$. For the 't Hooft limit, i.e. $g_s \to 0$ and $N_c \to \infty$ with fixed $\lambda = 2\pi g_s N_c$, the strength from the D3-branes becomes finite while the one from the D7-branes will vanish and then can be safely ignored. Therefore, we can consider the D7-branes as spacetime filling branes. The spacetime filling brane is a brane of which the world-volume dimension is the same as the one of the background spacetime [46]. The spacetime filling brane cannot have a net charge in order to avoid tadpoles, and one drains the D7-brane charge by wrapping the D7-branes around a trivial cycle with no flux [19]. In our case, the background spacetime is $AdS_5 \times S^5$ with the S^5 thought to be an internal sphere. The D7-brane is considered spacetime filling only in the AdS_5 part. The remaining three directions of the D7-brane are embedded in the internal topological $S^3 \subset S^5$, where the net charge is drained. Let us consider the field theory side. We know that using the $N_f \ll N_c$ and 't Hooft limits are equivalent to working in the quenched approximation, where the fermion loops in Feynman diagrams are neglected [36]. We will consider the D7-branes only in the probe limit from now on. Therefore, in gravity side for the non-compact case the D3-branes source the metric so that it become the Poincaré $AdS_5 \times S^5$ on which the gravity theory is the type IIB supergravity. For the compact case, like what we state in the chapter 2, we simply change the Poincaré $AdS_5 \times S^5$ to the global one, which is its covering, and assume the correspondence is still hold.

3.3 The Dictionary of the Flavour Brane

Let us review how the dictionary of the probe brane is constructed. The original AdS/CFT correspondence arises from the duality between open and closed strings. In contrast, the work [19] conjectures that with the probe brane added in the correspondence will also have the new duality which is between the open and the other open strings. This means fluctuations of the probe D7-brane in the gravity theory are mapped to gauge invariant operators in the dual field theory.

Let us look at the dynamics of the coincident N_f D7-brane. In low energy dynamics, the action of the D7-brane is composed of DBI and Chern-Simons actions as

$$S_{D7} = -T_{D7}N_f \int d^8\xi \sqrt{-\det\left(P[G]_{ab} + 2\pi\alpha' F_{ab}\right)} + \frac{(2\pi\alpha')^2}{2} T_{D7}N_f \int P[C_4] \wedge F \wedge F,$$
(3.3.1)

where the D7-brane tension is $T_{D7} = 1/((2\pi)^7 g_s \alpha'^4)$. We consider the global $AdS_5 \times S^5$ with the metric

$$ds^2 = -\left(1 + \frac{r^2}{R^2}\right)dt^2 + \frac{dr^2}{1 + \frac{r^2}{R^2}} + r^2 d\bar{\Omega}_3^2 + R^2 d\Omega_5^2,$$
(3.3.2)

where

$$d\Omega_5^2 = d\theta_1^2 + \sin^2\theta_1 d\phi_1^2 + \cos^2\theta_1 d\Omega_3^2,$$
(3.3.3)

$$d\Omega_3^2 = d\theta^2 + \sin^2\theta d\phi^2 + \cos^2\theta d\psi^2.$$
(3.3.4)

For convenience, we will use $\chi = \sin\theta_1$. We consider the D7-brane embedding ansatz

$$\chi = \chi(r),$$
$$\phi_1 = const.$$
(3.3.5)

With this ansatz the on-shell action of the D7-brane is

$$S_{D7} = -T_{D7}\mathcal{T}N_f \frac{R^3}{8}(2\pi)^4 \int dr \, r^3(1 - \chi(r)^2)$$
$$\times \sqrt{4(1 - \chi(r)^2) + \left(R^2 + 2r\left(r + \sqrt{r^2 + R^2}\right)\right)\chi'(r)^2}, \quad (3.3.6)$$

where $\mathcal{T} \equiv \int dt$. After we obtain the equation of motion, we consider the expansion of the field $\chi(r)$ near boundary $r \to \infty$ which is

$$\chi(r) = \frac{C_1}{r} + \frac{C_2}{r^3} + \frac{C_1 R^2}{2r^3}\log\left(\frac{R}{r}\right) + \mathcal{O}(r^{-4}).$$
(3.3.7)

This expansion is similar to (2.4.43) with the additional logarithmic term. As we have mentioned, the separation between the D3- and D7-branes determines the mass of the hypermultiplet or the quark. From the geometry, the distance between the D3- and D7-branes is given by

$$L = \lim_{r \to \infty} \frac{1}{2} \left(r + \sqrt{r^2 + R^2} \right) \chi(r) = C_1. \tag{3.3.8}$$

Thus C_1 in the expansion (3.3.7) is identified with the quark mass in the dual gauge theory. The explicit formula is $m_q = C_1/(2\pi\alpha')$, where m_q is the bare quark mass. In the same way as in (2.4.43), we would expect C_2 in (3.3.7) to be directly related to the vev of the quark mass; however, due to the presence of the logarithmic term one needs to renormalise C_2. We will consider the renormalisation in the next section.

3.4 Flavour Brane Renormalisation

Let us consider the on-shell D7-brane action in (3.3.6). The equation from this action indeed has $\chi(r) = 0$ as the trivial solution, which is actually mapped to the hypermultiplet with zero mass. For the case of the trivial solution; the on-shell action is then

$$S_{D7} = -T_{D7} \mathcal{T} N_f \frac{R^3}{4} (2\pi)^4 \int_0^\infty dr \, r^3. \tag{3.4.9}$$

We see this action diverges due to the upper limit of the integration. In other words, the action is divergent in the IR[1], so we need to regularise it to cancel the divergence. There are many regularisation schemes we can choose. We will use the cut-off regularisation scheme. In general, this scheme does not preserve the covariance, but if we use the appropriate counterterms, the covariance and the other symmetries will still be preserved [47, 48]. Before we apply the cut-off regularisation, it is convenient to use Fefferman-Graham coordinates [49], of which the radial coordinate z is related to r by

$$z = \frac{R}{r + \sqrt{r^2 + R^2}}. \tag{3.4.10}$$

---

[1]We will use the convention that the UV and the IR are regions at small (around AdS centre) and large (around AdS boundary) r respectively.

Here the AdS centre and boundary are located at $z = 1$ and $z = 0$ respectively. In this coordinate, applied the cut-off regularisation, the action (3.4.9) is then

$$S_{D7,reg} = T_{D7}\mathcal{T}N_f \frac{R^7}{64}(2\pi)^4 \int_\epsilon^1 dz \, \frac{(1-z^2)^3(1+z^2)}{z^5}. \tag{3.4.11}$$

Whether this is integrable or not, we only consider the expansion of it around the AdS boundary in which we will trace the divergence, so we have

$$S_{D7,reg} = T_{D7}\mathcal{T}N_f \frac{R^7}{64}(2\pi)^4 \left(\frac{1}{4\epsilon^4} - \frac{1}{\epsilon^2} + \mathcal{O}(\epsilon^0) \right), \tag{3.4.12}$$

where ϵ is treated as a very small positive number. (3.4.12) leaves divergence terms, and one might think of using the additive inverse as the counterterm would solve the problem, but this does not preserve the covariance. The counterterms to cancel the divergence that leave the covariance preserved are [47, 48, 50]

$$
\begin{aligned}
L_1 &= -\frac{1}{4}\sqrt{-\gamma}, \\
L_2 &= \frac{R^2}{48}\sqrt{-\gamma}R_\gamma, \\
L_3 &= -\frac{R^4}{32}\log\epsilon\sqrt{-\gamma}\left(R_{ij}R^{ij} - \frac{1}{3}R_\gamma^2 \right),
\end{aligned}
\tag{3.4.13}
$$

where R_{ij} and R_γ is the Ricci tensor and the Ricci scalar respectively, computed from the metric γ_{ij}. The counterterms are obtain from the geometry at the slice $z = \epsilon$; this is indeed to preserve the covariance [47]. Let γ_{ij} be the metric at the slice $z = \epsilon$ of the D7-brane embedding metric in the AdS_5 part[2]. For the trivial embedding $\chi(z) = 0$, the D7-brane embedding metric is

$$ds^2 = -\frac{(1+z^2)^2}{4z^2}dt^2 + R^2\frac{dz^2}{z^2} + \frac{R^2}{4z^2}(1-z^2)^2 d\bar{\Omega}_3^2 + R^2 d\Omega_3^2. \tag{3.4.14}$$

At the slice $z = \epsilon$, we have (with the $S^3 \subset S^5$ dropped)

$$ds^2 = \gamma_{ij}dx^i dx^j = -\frac{(1+\epsilon^2)^2}{4\epsilon^2}dt^2 + \frac{R^2}{4\epsilon^2}(1-\epsilon^2)^2 d\bar{\Omega}_3^2, \tag{3.4.15}$$

---

[2]For the S^5 part, all the directions are compact, so integrating over those directions will always yield a finite number. Since the directions in AdS_5 and S^5 have separated covariance groups, we can drop the S^5 part when we do the renormalisation without any influences to the whole covariance.

so the substituted counterterms are

$$L_1 = -R^3 \frac{(1-\epsilon^2)^3(1+\epsilon^2)}{128\epsilon^4} \sin\left(2\bar{\theta}\right),$$

$$L_2 = R^3 \frac{1-\epsilon^4}{64\epsilon^2} \sin\left(2\bar{\theta}\right), \tag{3.4.16}$$

$$L_3 = 0.$$

We bring these counterterms to be subtracted from the action in (3.4.12) yielding

$$S_{D7,\,sub} = S_{D7,\,reg} + 2\pi^2 T_{D7} \mathcal{T} N_f R^4 \int d\bar{\theta} d\bar{\phi} d\bar{\psi} \sum_i L_i$$

$$= -\frac{\pi^4}{4} T_{D7} \mathcal{T} N_f R^7 \epsilon^2 + \mathcal{O}(\epsilon^4), \tag{3.4.17}$$

where $(\bar{\theta}, \bar{\phi}, \bar{\psi})$ are the coordinates of the $\bar{S}^3 \subset AdS_5$. We see all the divergent terms are gone. Finally, we limit the cut-off parameter to the value representing the AdS boundary giving the renormalised action

$$S_{D7,\,ren} = \lim_{\epsilon \to 0} S_{D7,\,sub}. \tag{3.4.18}$$

For the non-trivial solution $\chi(z) \neq 0$, we do the same thing, but it will give additional divergent terms. More counterterms are then needed. The additional counterterms are [48, 50]

$$L_4 = \frac{1}{2}\sqrt{-\gamma}\,\chi(\epsilon)^2,$$

$$L_5 = -\frac{5}{12}\sqrt{-\gamma}\,\chi(\epsilon)^4, \tag{3.4.19}$$

$$L_6 = \frac{R^2}{12}\sqrt{-\gamma}R_\gamma\,\chi(\epsilon)^2 \log\chi(\epsilon).$$

The expansion of χ in z-coordinate near the AdS boundary is

$$\chi(z) = \frac{2C_1}{R}z + \left(\frac{2C_1}{R} + \frac{8C_2}{R^3}\right)z^3 + \frac{4C_1}{R}z^3 \log(2z) + \mathcal{O}(z^4), \tag{3.4.20}$$

where C_1 and C_2 are the same as ones in (3.3.7). Using this expansion along with the on-shell action in (3.3.6) and then applying the cut-off regularisation, we have the regulated action as

$$S_{D7,\,reg} = -T_{D7}\mathcal{T}N_f \frac{R^3}{8}(2\pi)^4 \left(\frac{R^4}{32}\frac{1}{\epsilon^4} - \frac{R^4 + 2C_1^2 R^2}{8}\frac{1}{\epsilon^2} - 2C_1^2 R^2 \log(\epsilon) + 2C_1^2 R^2 \right.$$

$$+ \frac{12C_2^2}{R^2} - \frac{8C_1^3 C_2}{R^2} + 3C_1^2 R^2 \log^2(2) + C_1^2 R^2 \log(64) - 2C_1^4$$

$$\left. + 12C_1 C_2 - 2C_1^4 \log(4) + 12C_1 C_2 \log(2) + \frac{7R^4}{32} + \mathcal{O}(\epsilon^0)\right). \tag{3.4.21}$$

The renormalised action is then

$$
S_{D7,ren} = -T_{D7}\mathcal{T}N_f \frac{R^3}{8}(2\pi)^4 \left[2C_1^2 R^2 + \frac{12C_2^2}{R^2} - \frac{8C_1^3 C_2}{R^2} + 3C_1^2 R^2 \log^2(2) \right.
$$
$$
+ C_1^2 R^2 \log\left(\frac{256 C_1}{R}\right) - \frac{17 C_1^4}{6} + 14 C_1 C_2 - 4C_1^4 \log(2)
$$
$$
\left. + 2C_1 C_2 \log(64) + (\text{terms not depending on } C_1 \text{ and/or } C_2) \right]. \quad (3.4.22)
$$

The vev of the operator $\mathcal{O}$ dual to a field χ is computed from [47, 48, 50]

$$
\langle \mathcal{O} \rangle = \lim_{\epsilon \to 0} \left(\frac{\epsilon^{-\Delta}}{\sqrt{-\gamma}} \frac{\delta S_{D7,sub}}{\delta \chi(\epsilon)} \right) = \frac{1}{\sqrt{-\tilde{g}_{(0)}}} \frac{\delta S_{D7,ren}}{\delta \chi_{(0)}}, \quad (3.4.23)
$$

where $\chi_{(0)} = C_1$ which is the coefficient corresponding to $\phi_0(x)$ in (2.4.43), and $\tilde{g}_{(0)}$ is the determinant of the metric $\tilde{g}_{(0),ij}$ obtained from the metric (3.4.14) with the part $S^3 \subset S^5$ dropped by

$$
ds^2 = -\frac{(1+z^2)^2}{4z^2}dt^2 + R^2\frac{dz^2}{z^2} + \frac{R^2}{4z^2}(1-z^2)^2 d\bar{\Omega}_3^2
$$
$$
= R^2\frac{dz^2}{z^2} + \frac{1}{z^2}\tilde{g}_{ij}dx^i dx^j
$$
$$
\quad (3.4.24)
$$

and the expansion near AdS boundary

$$
\tilde{g}_{ij} = \tilde{g}_{(0),ij} + \tilde{g}_{(2),ij}z^2 + \cdots. \quad (3.4.25)
$$

Finally, we obtain the vev from the field χ as

$$
\langle \mathcal{O} \rangle = -T_{D7}\mathcal{T}N_f \frac{R^3}{8}(2\pi)^4 \left[C_2 + \frac{C_1 R^2}{4} - \frac{1}{2}C_1 R^2 \log\left(\frac{C_1}{R}\right) \right] = -T_{D7}\mathcal{T}N_f \frac{R^3}{8}(2\pi)^4 \tilde{C}_2,
$$
$$
\quad (3.4.26)
$$

where C_1 and C_2 are the coefficients in the expansion (3.3.7), and $\tilde{C}_2$ are a renormalised value of C_2. This formula will be used to find the quark condensate in chapter 6. Unlike the original AdS/CFT correspondence, the vev does not only depends on C_2 but also depends on C_1.

Chapter 4

Jet Quenching

In this chapter we study the finite-size correction to the drag force applied to a quark moving in the QGP. We will follow through our work in [1]. We finally compare the result with the infinite size case.

4.1 Introduction

Many researches on holography have contributed to study the process in QGP, successfully created in RHIC [51–54] and LHC [55], in the strongly coupled regime. The fact that the quark-antiquark pair created near the boundary of QGP does not yield two back-to-back jets but leads to only one observed jet in the collider draws much attention. To give a qualitative explanation, one explains that the quark moving through QGP has its energy loss because of its interaction with the medium. This explanation is intuitively correct and easy to understand. However, as we have mentioned before, the drag force or the energy loss rate is a thermodynamically inequilibrium quantity, so directly calculating the quantitative drag force from lattice QCD is difficult. Having done it in the holographic way, in the work of [16,56], they modelled the quark in the strongly coupled QGP by an open string of which one end is on the boundary of the AdS spacetime and the other end is inside the AdS black hole horizon. This is illustrated in figure 4.1.

The string acts as a meson of which the quark and the anti-quark are located at the end points. The vertical lengths of the string measured from each end point to
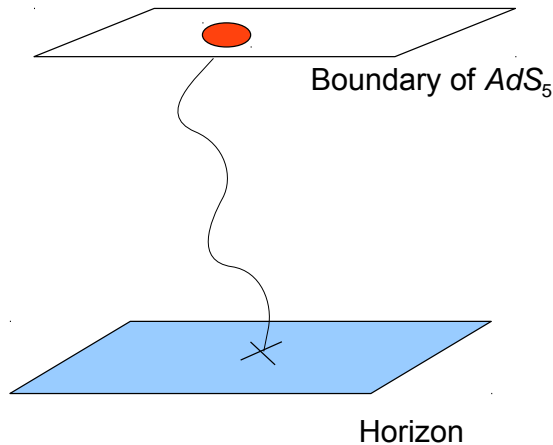
Figure 4.1: A holographic stringy model for the infinitely massive quark moving in strongly coupled QGP in infinite size where the underlying field theory is $\mathcal{N} = 4$ SYM in $\mathbb{R}_t \times \mathbb{R}^3$

the bottom represent each quark mass [57]. In this case the vertical length of the string is infinite, and so is the quark mass on the boundary. As the quark mass is infinite, it makes sense that they set the quark to have a constant velocity. While the quark is moving, the string attached to the quark is simply dragged and also exerts the reaction to the quark at the end point. They then calculated the drag force from there. This work studied the system in infinite size.

In reality, the QGP in the collider cannot have infinite size. The quark-antiquark pair propagating in the QGP should feel the effect of the QGP size. To study this we use the same holographic model of the quark and calculate drag force as in the work of [56], but rather than study it in the Poincaré AdS spacetime as done in the work, we will consider it in the global AdS spacetime. The holographic model picture is roughly illustrated in figure 4.2

The physical scales we have in the theory are the AdS radius R and the temperature T, so the only one possible dimensionless scale is TR. There is a limit that the global AdS spacetime will become the Poincaré one. That limit is the large black hole limit where the black hole horizon is taken to be very larger than the AdS radius or the sphere radius. The limit of large black hole translates to the limit of the dimensionless quantity as $TR \to \infty$. In fact the limit $TR \to \infty$ can be interpreted
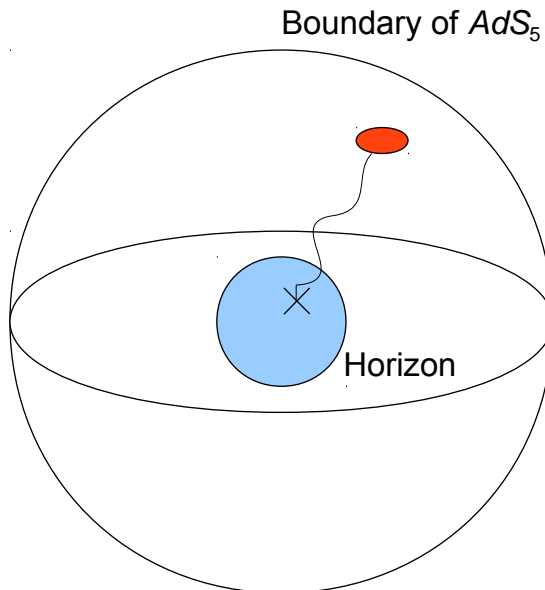
Figure 4.2: A holographic model for the infinitely massive quark moving in strongly coupled QGP with finite volume. The underlying theory is $\mathcal{N} = 4$ SYM on $\mathbb{R}_t \times S^3$.

as fixed volume and infinite temperature, or fixed temperature and infinite volume. We will interpret the limit as the latter one. We will find the finite-size effects of any observables by the expansion of them with respect to the quantity TR.

4.2 Dragged String in a Global AdS Black Hole[1]

Working in the gravity side, we will consider the system in the global AdS_5-Schwarzschild spacetime which has the metric:

$$ds^2 = -h(r)dt^2 + \frac{1}{h(r)}dr^2 + r^2 \left(d\theta^2 + \cos^2 \theta \left(d\phi^2 + \cos^2 \phi d\chi^2 \right) \right),$$

$$r_0^2 = \frac{8GM}{3\pi}, \qquad h(r) = 1 + \frac{r^2}{R^2} - \frac{r_0^2}{r^2},$$

(4.2.1)

where G is the gravitational constant, M is the mass of the black hole, R is the radius of the AdS spacetime and r is the radial coordinate. This AdS spacetime has the boundary at $r \to \infty$. The geometry at the boundary is $\mathbb{R}_t \times S^3$, in which the

---

[1]During the completion of this project, we became aware of the work [58] which has some overlap with the results in this section.

dual field theory lives. The black hole horizon at $r = r_H$ where

$$r_H = R\sqrt{\frac{\sqrt{1 + 4\frac{r_0^2}{R^2}} - 1}{2}}, \qquad r_0 = r_H\sqrt{1 + \frac{r_H^2}{R^2}}. \tag{4.2.2}$$

The black hole temperature is [59]

$$T = \frac{r_H}{\pi R^2}\left(1 + \frac{R^2}{2r_H^2}\right). \tag{4.2.3}$$

When the temperature goes down below $T_{HP} = 3/(2\pi R)$, the system undergoes a first-order phase transition where the system prefers the pure AdS_5 spacetime [39,41] with the metric

$$ds^2 = -\left(1 + \frac{r^2}{R^2}\right)dt^2 + \frac{1}{1 + \frac{r^2}{R^2}}dr^2 + r^2\left(d\theta^2 + \cos^2\theta\left(d\phi^2 + \cos^2\phi d\chi^2\right)\right). \tag{4.2.4}$$

The temperature can still be identified from the radius of the periodic time circle. With this phase transition in the bulk spacetime, the corresponding field theory encounters a deconfinement-to-confinement phase transition. This is in the sense that at $T > T_{HP}$ the free energy of the system is of order N_c^2 and at $T < T_{HP}$ it is of order one. We have two scale quantities in the boundary field theory i.e. the temperature T and the AdS radius R. Therefore, the dimensionless physical parameter is only TR. Investigating the finite-volume effect, we will fix the temperature and use the limit of the quantity $TR \to \infty$ as the large volume limit.

In comparison with the infinite-size case, we compare the global AdS_5-Schwarzschild spacetime with the Poincaré AdS_5-Schwarzschild spacetime with the metric

$$ds^2 = \frac{r^2}{R^2}\left(-\left(1 - \frac{r_H^4}{r^4}\right)dt^2 + d\vec{x}^2\right) + \frac{R^2}{r^2}\frac{dr^2}{1 - \frac{r_H^4}{r^4}}. \tag{4.2.5}$$

Instead of having $\mathbb{R}_t \times S^3$ as the boundary, the Poincaré AdS-Schwarzschild spacetime has the boundary geometry as $\mathbb{R}_t \times \mathbb{R}^3$. In the large black hole limit $r_H \gg R$, (4.2.1) will reduce to (4.2.5).

We model the dragged string in the global AdS spacetime by the embedding

$$\theta = \omega\tau + f(\rho), \tag{4.2.6}$$

where τ and ρ are the string world-sheet coordinates, we choose $\tau = t$ and $\rho = r$ and $f(\rho)$ is a non-trivial embedding profile function. Substituting this into the

Nambu-Goto action, we have the string action

$$S = \int d\tau d\rho \sqrt{1 + \rho^2 f'^2(\rho)h(\rho) - \frac{\rho^2\omega^2}{h(\rho)}}. \tag{4.2.7}$$

Our dynamical variables are $f(\rho)$ and $f'(\rho)$. We see that the action does not depends on $f(\rho)$, so the canonical momentum $\pi_f = \frac{\partial S}{\partial f'}$ is conserved. With the help of this conserved quantity, we can identify f' that is

$$f'(\rho) = \frac{\pi_f}{\rho h(\rho)} \sqrt{\frac{\rho^2\omega^2 - h(\rho)}{\pi_f^2 - \rho^2 h(\rho)}}, \tag{4.2.8}$$

and the string action turns a lot more simple

$$S = \int d\tau d\rho \, \rho \sqrt{\frac{\rho^2\omega^2 - h(\rho)}{\pi_f^2 - \rho^2 h(\rho)}}. \tag{4.2.9}$$

We require the action to be real, so if there happens to be a sign change in the numerator/denominator inside the square root, there has to be the sign change in the denominator/numerator as well at the same time. We suppose the sign change occurs at $\rho = \rho_*$, so we have

$$\rho_*^2\omega^2 - h(\rho_*) = 0 \qquad \text{and} \qquad \pi_f^2 - \rho^2 h(\rho) = 0. \tag{4.2.10}$$

Solving these, we get

$$\pi_f = \omega R^2 \frac{-1 \pm \sqrt{1 + 4\frac{r_0^2}{R^2}(1 - \omega^2 R^2)}}{2(1 - \omega^2 R^2)}, \tag{4.2.11}$$

of which the plus sign has to be chosen, for in the case of pure AdS spacetime ($r_0 = 0$) no dissipation occurs and the drag force should vanish.

We compute the drag force exerted on the string by the momentum flow along the string down to the horizon. The flow of the momentum is [56]

$$\frac{dp_\theta}{dt} = \sqrt{-g}P^\rho{}_\theta, \qquad P^a{}_\mu \equiv -\frac{1}{2\pi\alpha'}G_{\mu\nu}g^{ab}\partial_b X^\nu, \tag{4.2.12}$$

where $P^a{}_\mu$ is the spacetime energy momentum world-sheet current, $G_{\mu\nu}$ is the spacetime metric and g_{ab} is the world-sheet metric. Using (4.2.11), (4.2.12) and the metrics, we eventually have the drag force in the global case

$$\frac{dp_\theta}{dt} = -\frac{1}{2\pi\alpha'}\pi_f. \tag{4.2.13}$$

4.3 Comparison with the Infinite-size Case

The drag force in the infinite-size case done in [56] using the Poincare AdS spacetime. The string embedding is given by

$$x = vt + \xi(r), \tag{4.3.14}$$

and the canonical momentum

$$\pi_\xi = \frac{r_H^2}{R^2} \frac{v}{\sqrt{1 - v^2}}. \tag{4.3.15}$$

The drag force in this case is

$$\frac{dp_x}{dt} = -\frac{1}{2\pi\alpha'}\pi_\xi = -\frac{r_H^2}{2\pi\alpha' R^2} \frac{v}{\sqrt{1 - v^2}} = -\pi\tilde{T}^2 \sqrt{\frac{\lambda}{2}} \frac{v}{\sqrt{1 - v^2}}, \tag{4.3.16}$$

where $R^4 = 2\lambda\alpha'^2$, $\tilde{T} = \frac{r_H}{\pi R^2}$ and λ is the 't Hooft coupling.

To compare this drag force to the one in finite-size case, we use the large black hole limit

$$\rho_H \gg R. \tag{4.3.17}$$

This limit makes the boundary S^3 become a flat $\mathbb{R}^3$. For some dimensional analysis, the phase space coordinates (θ, π_f) in the global case are to compare with $(x/R, \pi_\xi R)$ in the Poincaré case, and the angular velocity ω is to compare with the linear one $v = \omega R$. We can expand the drag force in (4.2.13) in the order of dimensionless volume scale TR as

$$\frac{dp_\theta}{dt} = -\pi T^2 \sqrt{\frac{\lambda}{2}} \frac{\omega R^2}{\sqrt{1 - \omega^2 R^2}} \left[1 - \frac{1 + \sqrt{1 + \omega^2 R^2}}{2\pi^2\sqrt{1 - \omega^2 R^2}} \left(\frac{1}{TR}\right)^2 + \frac{1}{8\pi^2} \frac{3\omega^2 R^2 - 2}{1 - \omega^2 R^2} \left(\frac{1}{TR}\right)^4 + \cdots \right].$$
$$\tag{4.3.18}$$

This can be viewed as

$$\frac{1}{R}\frac{dp_\theta}{dt} = \frac{dp_x}{dt} \left[1 - \frac{1 + \sqrt{1 + v^2}}{2\pi^2\sqrt{1 - v^2}} \left(\frac{1}{TR}\right)^2 + \frac{1}{8\pi^2} \frac{3v^2 - 2}{1 - v^2} \left(\frac{1}{TR}\right)^4 + \cdots \right], \tag{4.3.19}$$

where the RHS is the translational drag force in the finite-size case and the LHS is the expansion in the large volume limit with the leading order agreeing with the result in the infinite-size case.

To see whether the finite-size effect in this model is significant for the experiment at RHIC or not, let us first use the International System of Units (SI) for the

temperature T and the size R by changing

$$TR \rightarrow \left(\frac{k_B}{\hbar c}\right) T_{real} R_{real}, \tag{4.3.20}$$

where the Boltzmann constant $k_B = 1.381 \times 10^{-23}$ J/K, the reduced Planck constant $\hbar = 1.055 \times 10^{-34}$ J-s and the speed of light in vacuum $c = 2.998 \times 10^8$ m/s. Unless stated otherwise, T_{real} and R_{real} will have units of Kelvin (K) and metre (m), respectively. We compute the difference of the drag force in infinite and finite size cases in a percentage by

$$\begin{aligned}\%\text{Difference} &= \frac{\text{Drag force in infinite size} - \text{Drag force in finite size}}{\text{Drag force in infinite size}} \times 100\% \\ &= \frac{\frac{dp_x}{dt} - \frac{1}{R}\frac{dp_\theta}{dt}}{\frac{dp_x}{dt}} \times 100\%.\end{aligned}$$

$$\tag{4.3.21}$$

We will focus on an ultra-relativistic quark having $v = 0.999(c)$. The plot of T_{real} vs R_{real} of the QGP is shown in figure 4.3 of which the curve gives %Difference $= 5\%$ that is quite significant for the data observed in the experiment. The QGP at RHIC
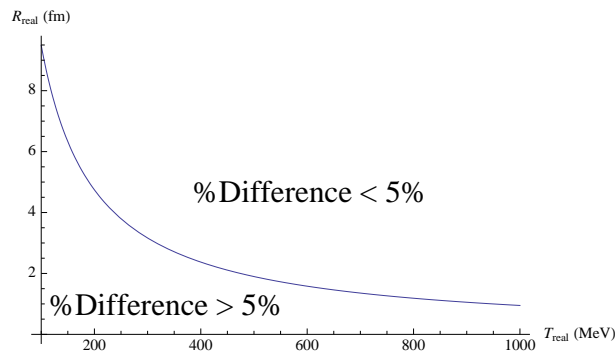
Figure 4.3: A plot of T_{real} vs R_{real} of the QGP where the curve gives %Difference $= 5\%$. The regions above and below the curve give %Difference $< 5\%$ and %Difference $> 5\%$, respectively.

has temperature around 4×10^{12} K or 345 MeV. At this value, we read off the QGP size from figure 4.3 as 2.75 fm. This means if the size of the QGP produced in RHIC is less than about $2-3$ fm, one should really consider the finite-size effect.

4.4 Discussion

We finally have the finite-size correction to the quark energy loss. From (4.3.19), the leading correction term is negative. It means the drag force in QGP is lower in magnitude when the QGP has finite size. This contradicts many of the Newtonian fluids [60, 61].

When we work in the experimental units for the temperature and the length, the size of the QGP that the finite-size effect becomes significant is in the same order of magnitude as ones discussed in some related literature [62–64]. This means that finite-size effects predicted by the AdS/CFT correspondence could be relevant to obtain agreement with experimental data.

It is possible to believe that the decrease of the drag force arises because the system is in a non-boundary space. In this case it is S^3. This somehow quantises the energy, and some of the hydrodynamical modes are suppressed. This possibly makes the magnitude of the drag force in the finite-size QGP smaller than the one in the infinite size. It is interesting to investigate the finite-size effects in other strongly coupled holographic systems to see if the related features arise.

Chapter 5

Meson Spectra and New Ground States with an Isospin Chemical Potential

As done in our paper [2], we analyse the meson fluctuations and new ground states of the $\mathcal{N} = 2$ SYM theory at strong coupling in compact space, S^3, with the influence of an isospin chemical potential by using AdS/CFT correspondence. For large enough values of the chemical potential the system shows an instability. Unlike other related models, the first unstable mode is from a global $SO(4)$ charged scalar rather than from a vector. One then construct the new ground state to cure the instability. In addition, the fluctuation spectrum yields a cross-over behaviour as a function of the temperature.

5.1   Introduction

Many models of QCD suggest that with a sufficiently high isospin chemical potential the meson condensation will occur. When the value of the chemical potential reaches the order of the lightest meson mass in the model, the condensation is expected to happen. If the chemical potential increases further to the order of mass of the next heavier particle, the condensation will take place again and so on. While it is easy to understand intuitively, direct computation from the first principle is difficult.

Adding scales to the theory, we expect some interesting or unusual effects to happen as well as we have mentioned in the previous chapters. We are interested to add the volume scale to the model. The model we are considering is the D3/D7 system. First without the D7 part, in the non-compact case, its ambient spacetime is the Poincaré patch of $AdS_5 \times S^5$. The Poincaré patch arises from the near horizon limit of the supergravity solution of the N_c coincident D3-brane, where $N_c \to \infty$. To add the finite volume scale, this can be done by replacing the Poincaré patch with the global $AdS_5 \times S^5$. The finite size scale we obtain is the radius of the AdS spacetime and the five-sphere which are constrained to be equal by the supersymmetric reason. In contrast to the Poincaré patch, the global $AdS_5 \times S^5$ is not obtained from the near horizon limit of any D-brane configurations, but it is believed that the correspondence is still valid. For the finite temperature case beyond the Hawking-Page temperature, the bulk spacetime changes a little bit by having a Schwarzschild black hole at the centre. The temperature of the dual field theory side is thus the Hawking temperature of the black hole.

We want to study the mesonic excitations in the model. To do that, it is needed to add the matter to the field theory side. This is holographically equivalent to adding the D7-brane to the gravity side. As we have seen in the previous chapters, adding the D7-brane breaks the supersymmetry from $\mathcal{N} = 4$ to $\mathcal{N} = 2$. It includes the matter in fundamental representation, called the quark. The internal symmetries of the field theory side are interpreted from the isometry of the internal three-sphere. They are a global $SO(4)$ R-symmetry and an $SU(N_f)$ flavour symmetry, where N_f is the number of the D7-brane. The chemical potential associated to each of the symmetries can be introduced. In our work we will choose the chemical potential associated to the flavour symmetry.

5.2 Holography with a Dual S^3

5.2.1 Brane Embeddings in Global $AdS_5 \times S^5$ and AdS_5-Schwarzschild

As mentioned in the previous chapters, an example of the AdS/CFT correspondence is the duality between the string theory of type IIB in the Poincaré patch of $AdS_5 \times S^5$ spacetime and the $\mathcal{N} = 4$ SYM theory at zero temperature on $\mathbb{R}_t \times \mathbb{R}^3$. This is for the infinite-size case. However, for the compact case it is strongly believed that the type IIB string theory on the global $AdS_5 \times S^5$ is dual to the $\mathcal{N} = 4$ SYM theory on $\mathbb{R}_t \times S^3$.

The metric of the global $AdS_5 \times S^5$ spacetime is

$$ds^2 = -\left(1 + \frac{r^2}{R^2}\right) dt^2 + \frac{dr^2}{1 + \frac{r^2}{R^2}} + r^2 d\Omega_3^2 + R^2 d\Omega_5^2. \tag{5.2.1}$$

This is called the thermal AdS spacetime. It is only valid at the temperature from zero to Hawking-Page temperature as we have mentioned in chapter 2. For the higher temperature, the system prefers the spacetime to be AdS_5-Schwarzschild$\times S^5$ of which the metric is

$$ds^2 = -\left(1 + \frac{r^2}{R^2} - \frac{r_0^2}{r^2}\right) dt^2 + \frac{dr^2}{1 + \frac{r^2}{R^2} - \frac{r_0^2}{r^2}} + r^2 d\Omega_3^2 + R^2 d\Omega_5^2, \tag{5.2.2}$$

where $r_0^2 = 8GM/(3\pi)$, G is the Newton constant and M is the mass of the black hole. The temperature of the black hole is

$$T = \frac{r_H}{\pi R^2}\left(1 + \frac{R^2}{2r_H^2}\right), \tag{5.2.3}$$

where

$$r_H = R\sqrt{\frac{\sqrt{1 + 4\frac{r_0^2}{R^2}} - 1}{2}}. \tag{5.2.4}$$

This temperature will play a role as the temperature in the gauge theory. The dimensionless quantity is TR, and we will later on expand our results for large values of this parameter, interpreting this limit as one at finite temperature and large volume [48, 50], so that a comparison with results in the Poincaré patch can be made.

Introducing D7-probe branes in this geometry corresponds, in the holographic language, to adding flavour hypermultiplets to $\mathcal{N} = 4$ SYM on the sphere S^3. A study of various D-brane probes, in particular D7-probe branes, in these geometries was performed in [48, 50]. It was found that at zero (and low) temperature, there are two possible D7-brane embeddings in this dual geometry. The first type of embeddings are those in which the D7-brane completely fills the AdS_5 space and wraps the $S^3 \subset S^5$ which is equatorial (i.e it is a D-brane with vanishing extrinsic curvature). The second type of embeddings are those in which the D7-brane wraps a non-maximal $S^3 \subset S^5$ which shrinks along the radial direction of AdS_5 and becomes zero before the brane reaches the origin of AdS_5. The first series is dual to the $\mathcal{N} = 2$ SYM theory with massless hypermultiplets, while for the second class the hypermultiplet is massive, and its mass is related to the distance at which the D7-brane "stops" before the origin of the AdS_5. Interestingly, as the "quark" mass is varied a topology changing phase transition occurs [48]. It was further analysed in detail in [50] that this phase transition is actually third order, unlike most of the phase transition associated to probe branes in holographic duals, which are usually first order.

In the high temperature phase, the situation is similar to that in infinite volume. One finds that Lorentzian and black hole embeddings exhaust all possibilities. As for infinite volume, these correspond to D7-branes that stay outside the horizon or reach the black hole horizon respectively.

In this research we will be studying various D-brane embeddings in the presence of an "isospin" chemical potential. For that purpose, instead of using the coordinates (5.2.1), it will be useful to use another set of coordinates given by

$$ds^2 = -\frac{u^2}{R^2} \left(1 + \frac{R^2}{4u^2}\right)^2 dt^2 + u^2 \left(1 - \frac{R^2}{4u^2}\right)^2 d\bar{\Omega}_3^2 + \frac{R^2}{u^2}(du^2 + u^2 d\Omega_5^2), \quad (5.2.5)$$

which is related to (5.2.1) via the coordinate change

$$u = \frac{1}{2}(r + \sqrt{r^2 + R^2}). \quad (5.2.6)$$

In these coordinates the origin of the AdS space is at $u = R/2$, while the boundary is an S^3 at $u \to \infty$. We will also use

$$ds^2 = -\frac{1}{4z^2} \left(1 + z^2\right)^2 dt^2 + \frac{R^2}{4z^2} \left(1 - z^2\right)^2 d\bar{\Omega}_3^2 + R^2 \frac{dz^2}{z^2} + R^2 d\Omega_5^2, \quad (5.2.7)$$

which is related to the previous coordinates by $z = R/(2u)$. Let us also note that in the z coordinate the origin of AdS space is at $z = 1$, while the boundary is at $z = 0$.

Similarly for the system at finite temperature in addition to metric (5.2.2) we will also use (u, t) coordinates,

$$\mathrm{d}s^2 = -\frac{2\rho_H^2}{uR^2}\frac{F(u)}{W(u)}\mathrm{d}t^2 + 2\frac{\rho_H^2}{u}W(u)\mathrm{d}\bar{\Omega}_3^2 + \frac{R^2}{4u^2F(u)}\mathrm{d}u^2 + R^2\mathrm{d}\Omega_5^2, \tag{5.2.8}$$

where

$$F(u) = 1 - u^2, \quad \frac{\rho_H^4}{R^4} = \frac{1}{16} + \frac{r_0^2}{4R^2}, \quad W(u) = 1 - \frac{uR^2}{4\rho_H^2}. \tag{5.2.9}$$

Note here that the variable u is dimensionless and ranges from $u \in [0, 1]$, where the horizon is at $u = 1$, and the boundary is at $u = 0$. The Hawking temperature of this black hole is

$$T = \frac{\sqrt{2}\rho_H}{\pi R^2 \sqrt{1 - \frac{R^2}{4\rho_H^2}}}. \tag{5.2.10}$$

For numerical investigation it turns out that another form of the metric at finite T will also be useful.[1] If we change coordinates as

$$v = \frac{1 - u}{1 - \frac{uR^2}{4\rho_H^2}} \qquad \Lambda = \frac{8\rho_H^2}{4\rho_H^2 + R^2}, \tag{5.2.11}$$

then the metric becomes

$$\mathrm{d}s^2 = -\frac{v(\Lambda - v)}{(1 - v)(2 - \Lambda)}\mathrm{d}t^2 + \frac{\Lambda - 1}{(2 - \Lambda)(1 - v)}R^2\mathrm{d}\bar{\Omega}_3^2 + \frac{\Lambda - 1}{4(1 - v)^2 v(\Lambda - v)}R^2\mathrm{d}v^2 + R^2\mathrm{d}\Omega_5^2, \tag{5.2.12}$$

where

$$\mathrm{d}\Omega_3^2 = \frac{1}{4}(\mathrm{d}\alpha^2 + \mathrm{d}\beta^2 + \mathrm{d}\gamma^2 + 2\cos\beta\,\mathrm{d}\alpha\,d\gamma). \tag{5.2.13}$$

In these coordinates $v = 0$ is the horizon while $v = 1$ is the boundary, and Λ is function of the temperature given by

$$\Lambda = \frac{4(\pi TR)^2}{3(\pi TR)^2 - \sqrt{(\pi TR)^2\left(-2 + (\pi TR)^2\right)}}. \tag{5.2.14}$$

---

[1]This is related to the fact that the solutions at vanishing bare quark mass can be related to Heun functions in these coordinates.

5.2.2 Chemical Potentials and Homogeneous Solutions

In this section we will construct solutions which correspond to adding a chemical potential associated to the global $SU(2)$ flavour symmetry. This symmetry originates from the fact that we are considering two coinciding D7-probe branes. In addition to the $SU(2)$ symmetry, our systems also exhibits another global $SO(4)$ symmetry associated to the residual global isometry of the system of probes. In principle one could also consider switching on a chemical potential which is associated to this symmetry group, as it was done in e.g. [65]. However, our prime interest will be the physically more relevant $SU(2)$ group, which has direct analogue with the $SU(2)$ flavour symmetry group in the Sakai-Sugimoto model [66].

In order to turn on a chemical potential corresponding to this global $SU(2)$ "isospin" symmetry, let us consider two coincident D7-branes, which for simplicity have equatorial embedding $\theta = 0$, so that the induced metric on the D7-branes is

$$\mathrm{d}s^2 = -\frac{u^2}{R^2}\left(1 + \frac{R^2}{4u^2}\right)^2 \mathrm{d}t^2 + \frac{R^2}{u^2}\mathrm{d}u^2 + u^2\left(1 - \frac{R^2}{4u^2}\right)^2 \mathrm{d}\bar{\Omega}_3^2 + R^2\mathrm{d}\Omega_3^2. \quad (5.2.15)$$

In other words, the D7-probes fill out the full AdS_5 space, as well as a maximal $S^3 \subset S^5$. We should note that there are two S^3 factors present on the world-volume of the brane, one $\bar{\Omega}_3$ which is dual to the boundary S^3 and another one S^3 in S^5, which is part of the global symmetry group.

As explained in [67,68], in order to turn on a chemical potential we need to turn on the A_0 component of the gauge field, such that it satisfies the boundary condition

$$A_0(x, z \to 0) \to \mu_I\tau^3, \quad (5.2.16)$$

where $\tau^a = \sigma^a/2$ and σ^a are Pauli matrices. As a first guess for finding the ground state of the system in the presence of this chemical potential, we consider the homogeneous ansatz

$$A = A_0^{(3)}(u)\tau^3\,\mathrm{d}t\,, \quad (5.2.17)$$

so that the DBI action becomes

$$S = -T_{D7}8\pi^4R^3\int\mathrm{d}z\sqrt{-g(z)}\left[1 + \frac{\pi^2R^4}{2\lambda}\left(\partial_z A_0^{(3)}(z)\right)^2 g^{tt}(z)g^{zz}(z)\right]^{1/2}. \quad (5.2.18)$$

The equation of motion for the field $A_0(z)$ can be integrated once, yielding

$$\partial_z(A_0^{(3)}(z)R) = \frac{4cz(1+z^2)}{\sqrt{(1-z^2)^6 + 32\frac{c^2\pi^2}{\lambda}z^6}} \,, \tag{5.2.19}$$

where c is an integration constant. We are looking for a physical configuration which is smooth and differentiable everywhere. Specifically, we require that the field A_0 and its derivatives are smooth at the origin of AdS space. However, by expanding the right hand side of the above equation near the origin of AdS space one sees that the radial derivative of the A_0 field is non-vanishing. In other words, it is not possible to obtain any nontrivial (different from a constant solution) homogeneous solution which is smooth at the origin. This observation persists also for the Yang-Mills truncation of the DBI action, and it also holds in the Poincaré limit (see [67]). Hence as the starting configuration for our fluctuation analysis we will use a homogeneous solution with non-zero isospin potential, given by

$$A_0 = a_0\tau^3 \,, \qquad a_0 = \text{const.} \,. \tag{5.2.20}$$

This solution implies that at zero temperature, the homogeneous background does not lead to generation of an isospin density.

Above the Hawking-Page transition, the situation is similar. The homogeneous ansatz yields a first order differential equation,

$$\partial_u A_0^{(3)}(u) \left(1 - \frac{uR^2}{4\rho_H^2}\right)^2 = a_0 \,, \tag{5.2.21}$$

where a_0 is an integration constant. This is solved by

$$A_0^{(3)}(u) = \frac{\mu_I(1-u)}{1 - \frac{uR^2}{4\rho_H^2}} \,, \tag{5.2.22}$$

where we have imposed the boundary condition that $A_0(u \to 0) = \mu_I$ at the boundary, and also required vanishing of A_0 at the horizon of the black hole in AdS space. In contrast to the low temperature situation, we see that there is now a non-vanishing isospin density present, even for this homogeneous system.

5.3   Perturbative Analysis of the Homogeneous Vacuum at $T = 0$

While the homogeneous and isotropic solution which was discussed in the previous section is a legitimate solution to the equations of motion, we expect that for large enough values of the chemical potential this configuration will become unstable and "decay" into another, presumably non-homogeneous or non-isotropic ground state. Our expectations are based on a similar analysis which was previously performed for the Sakai-Sugimoto model in [66]. A major difference, however, with respect to the analysis of that paper is that we are now dealing with a field theory on a compact space. In the present section we will discuss the perturbative stability analysis at $T = 0$, which from a technical perspective largely follows the meson spectrum analysis of [18]; we recall some elements of that construction for completeness and in order to be able to compare with the finite temperature analysis which is to follow in section 5.4.

5.3.1   Scalar Fluctuations at Zero Temperature

We will start the perturbative analysis of the homogeneous solution (5.2.20) by considering scalar perturbations. By scalars we here mean scalars in the dual theory that are also scalars from the point of view of the D7-probe, i.e. gauge theory scalar fields which are uncharged under the $SO(4)$. Some of the scalars in the dual gauge theory originate from the components of the gauge field on the D7-probe and will be analysed in the next section. Our starting point is the flat (i.e. maximal) D7-probe embedding with the world-volume field (5.2.20) turned on. The induced metric on the world-volume was written in (5.2.15). Since the D7-probe brane is filling out the full AdS_5 space and wrapping a maximal S^3 in S^5, there are only two transverse scalars to the brane world-volume, and they are within the S^5. To see which scalars these are, let us write the metric on S^5 as

$$\mathrm{d}s_5^2 = R^2(\mathrm{d}\theta^2 + \sin^2\theta\,\mathrm{d}\phi^2 + \cos^2\theta\,\mathrm{d}\Omega_3^2)\,. \tag{5.3.23}$$

Instead of using the (θ, ϕ) coordinates it will be more convenient to introduce coordinates

$$w_1 = R \sin \theta \cos \phi \quad w_2 = R \sin \theta \sin \phi, \tag{5.3.24}$$

so that the metric on S^5 becomes

$$ds_5^2 = \left(1 - \frac{w_1^2 + w_2^2}{R^2}\right) d\Omega_3^2 + dW^2(w_1, w_2). \tag{5.3.25}$$

Here dW^2 is a complicated expression in terms of w_1, w_2, which however significantly simplifies for $w_1 = 0, w_2 = w$, as it then becomes

$$dW^2(w_1, w_2) \rightarrow \frac{dw^2}{1 - \frac{w^2}{R^2}}. \tag{5.3.26}$$

It can easily be checked from the equations of motion that it is indeed consistent to set one of the w_1, w_2 to zero.[2] We expect that the first instability will appear already for the lowest lying (S-wave) mode on the dual gauge theory sphere $\bar{S}^3$, which is also a singlet on $S^3 \subset S^5$. Therefore, when looking for the instabilities in the system, we will look at the fluctuation which is a function of only the time and u-coordinates. Let us define the fluctuation variable as

$$\Psi(t, u) = \delta w_2(t, u). \tag{5.3.27}$$

The induced metric on the D7-brane becomes

$$ds^2 = -\frac{u^2}{R^2}\left(1 + \frac{R^2}{4u^2}\right)^2 dt^2 + u^2\left(1 - \frac{R^2}{4u^2}\right)^2 d\bar{\Omega}_3^2$$

$$+ \frac{R^2}{u^2}du^2 + R^2\left(1 - \frac{\Psi(t, u)^2}{R^2}\right)d\Omega_3^2 + \left(\frac{\partial\Psi(t, u)}{\partial t}dt + \frac{\partial\Psi(t, u)}{\partial u}du\right)^2. \tag{5.3.28}$$

We next need to write down the action for the scalar fluctuation to leading order in α'. A subtle point here is that all scalars are in the adjoint representation of the $SU(2)$ group on the world-volume of two D7-branes. The approach we adopt here to write the action, is to first treat all scalars as Abelian and derive the action for the fluctuation by linearising the DBI action. In the last step we then promote all

---

[2]The fluctuation in the other direction leads to the same spectrum, so we will not comment on it any further (though we should emphasise that this is a property of the equatorial embedding not shared by non-zero bare quark mass embeddings).

fields to be in the adjoint representation by introducing an overall trace in front of the action (for more on this and other approaches, see e.g. [69, 70]).

Following these steps we end up with the action governing the scalar fluctuations,

$$S = -T_{D7} \frac{4\pi^6 R^4}{\lambda} \int \mathrm{d}u \mathrm{d}t \, u^3 \left(1 + \frac{R^2}{4u^2}\right) \left(1 - \frac{R^2}{4u^2}\right)^3$$

$$\times \left[-\frac{R^2}{2} \left(\frac{4u}{4u^2 + R^2}\right)^2 D_t \Psi^{(a)} D_t \Psi^{(a)} + \frac{u^2}{2R^2} \partial_u \Psi^{(a)} \partial_u \Psi^{(a)} - \frac{3}{2} \frac{\Psi^{(a)}\Psi^{(a)}}{R^2}\right] . \quad (5.3.29)$$

Since we expect that an instability will appear in the gauge direction orthogonal to the background field A_0, we make the ansatz for the fluctuation field to be

$$\Psi(t, u) = e^{-i\omega t} \left(\Psi^{(1)}_\omega(u)\tau^1 + \Psi^{(2)}_\omega(u)\tau^2\right) , \quad (5.3.30)$$

where we have focused on one Fourier mode.

The equations of motion for the components $\Psi^{(1)}_\omega$ and $\Psi^{(2)}_\omega$ are coupled, but can be decoupled by changing variables as

$$\Psi^{(\pm)}_\omega(u) = \Psi^{(1)}_\omega(u) \pm i\Psi^{(2)}_\omega(u) . \quad (5.3.31)$$

The equations of motion for the components $\Psi^{(\pm)}$ are

$$\frac{\partial_u(\sqrt{-g}g^{uu}\partial_u\Psi^{(\pm)}_\omega)}{\sqrt{-g}g^{uu}} - \frac{g^{tt}}{g^{uu}} \left(\omega \pm A^{(3)}_0\right)^2 \Psi^{(\pm)}_\omega + \frac{3}{R^2 g^{uu}}\Psi^{(\pm)}_\omega = 0 , \quad (5.3.32)$$

which for the specific metric on the D7-brane world-volume become

$$\partial_u^2 \Psi^{(\pm)}_\omega + \frac{\partial_u \left(u^5 \left(1 + \frac{R^2}{4u^2}\right)\left(1 - \frac{R^2}{4u^2}\right)^3\right)}{u^5 \left(1 + \frac{R^2}{4u^2}\right)\left(1 - \frac{R^2}{4u^2}\right)^3} \partial_u \Psi^{(\pm)}_\omega$$

$$+ \left[\frac{R^4}{u^4 \left(1 + \frac{R^2}{4u^2}\right)^2} \left(\omega \pm \mu\right)^2 + \frac{3}{u^2}\right] \Psi^{(\pm)}_\omega = 0 . \quad (5.3.33)$$

These equations can be solved by reducing them to Schrödinger form. A very similar equation has been analysed in [18] for the determination of the mesonic spectrum on the world-volume of a probe $D7$ brane at $T = 0$, in global AdS space. Following steps similar to those in [18], and focusing on modes which are constant both on the $S^3 \subset S^5$ and on the gauge theory $\bar{S}^3$, we obtain for the spectrum of fluctuations

$$(\mu + \omega)R = \pm(3 + 2n) \quad n = 0, 1, 2, \dots . \quad (5.3.34)$$

Here n is the main quantum number. We see that the key effect of the non-vanishing chemical potential is to shift the frequency $\omega \to \omega + \mu$. Because of this we see that for large enough chemical potential $\mu > \mu_{\text{crit}} = 3/R$, the frequency of the lowest lying mode becomes zero, signalling that the homogeneous solution potentially becomes unstable at this value of the chemical potential, and a condensate of the scalar might form.

5.3.2   Vector Fluctuations at Zero Temperature

Following the perturbative analysis in the scalar sector, we now turn our attention to vectors. We again expect unstable modes, but would like to know whether or not they occur before the instability of the scalar sector. An analysis of the vector mode spectrum was performed in infinite volume limit (on the Poincaré patch) in [71] and then later extended to non-zero chemical potential in [68, 70, 72]. At finite volume and vanishing temperature and chemical potential the spectrum can be found in [18]. The upshot of the analysis of [71] is that the lowest lying supermultiplet consists of two transverse scalars describing the transverse fluctuations of the D7-brane in the S^5, one scalar which originates from the vector component in the internal $S^3 \subset S^5$ wrapped by the D7-brane, and gauge components in the non-compact directions of AdS_5. As one moves to the compact case, i.e. global AdS space [18], the states from this supermultiplet get reorganised (split) so that the lightest state in the compact space is the scalar which originates from the component of the gauge field in the direction of the internal $S^3 \subset S^5$. The vector components in the direction of the dual sphere as well as the transverse scalars both have larger masses. We now want to see how the fluctuations from the vector sector are shifted upon introducing a chemical potential.

The Gauge Theory Vector Fluctuations

Let us start with the vector components in the direction of the sphere $\bar{S}^3$ of the dual gauge theory. These fluctuations are dual to the vector excitations in the gauge

theory. Similarly to what we did for scalars, we start by writing the fluctuations as

$$A = A_0^{(3)}(u)\tau^3 dt + R a_i^{(1)}(t, u, \bar{\Omega}_3)\tau^1 d\bar{\theta}^i + R a_i^{(2)}(t, u, \bar{\Omega}_3)\tau^2 d\bar{\theta}^i \,, \tag{5.3.35}$$

where $i = (1, 2, 3)$ are indices on the dual $\bar{S}^3$, and as for scalars we fluctuate in the gauge directions orthogonal to $A_0^{(3)}$. Since we know that the lowest lying vector is a singlet on S^3 we do not have to consider excitations which depend on the coordinates of the internal sphere.[3]

Next, we linearise the Yang-Mills action on the world-volume of the D7-probe,

$$S = -T_{D7}\pi^2 \frac{R^4}{2\lambda} \int d^8\xi \sqrt{-g} \Bigg[(\partial_u A_0^{(3)})^2 g^{tt} g^{uu}$$

$$+ R^2 \left(((D_t a_i)^{(a)})^2 g^{tt} g^{ii} + (\partial_u a_i^{(a)})^2 g^{uu} g^{ii} \right) + R^2 (f_{ij}^a)^2 g^{ii} g^{jj} \Bigg] \,, \tag{5.3.36}$$

where

$$(D_t a_i)^{(a)} = \partial_t a_i^{(a)} - \epsilon^{abc} A_0^{(b)} a_i^{(c)} \,, \qquad f_{ij}^a = (\partial_i a_j^{(a)} - \partial_j a_i^{(a)}) \,. \tag{5.3.37}$$

Here, g_{ij} is the metric on $\bar{S}^3$. The equations of motion for the fluctuations $a_i^{(a)}$ are given by

$$\sqrt{-g}\epsilon^{abc} A_0^{(c)} D_t a_i^{(b)} g^{tt} g^{ii} + \sqrt{-g}\partial_t \left(D_t a_i^{(a)} \right) g^{tt} g^{ii} + \partial_u \left(\sqrt{-g}\partial_u a_i^{(a)} g^{uu} g^{ii} \right)$$

$$+ \sum_j \left(\sqrt{-g} \left(\partial_j a_i^{(a)} - \partial_i a_j^{(a)} \right) g^{jj} g^{ii} \right) = 0, \tag{5.3.38}$$

In order to solve this equation let us Fourier transform in the time direction. In order to decouple the equations for the fluctuations $a_i^{(1)}$ and $a_i^{(2)}$ we introduce a new pair of variables

$$\bar{X}_i^{(\pm)}(u, \omega, \bar{\Omega}_3) = e^{-i\omega t} \left(a_i^{(1)}(u, \omega, \bar{\Omega}_3) \pm i a_i^{(2)}(u, \omega, \bar{\Omega}_3) \right) \,. \tag{5.3.39}$$

This finally yields the fluctuation equations

$$\partial_u \left(\sqrt{-g}g^{uu} g^{ii} \partial_u \bar{X}_i^{(\pm)} \right) + \sum_j \partial_j \left(\sqrt{-g}g^{jj} g^{ii} \left(\partial_j \bar{X}_i^{(\pm)} - \partial_i \bar{X}_j^{(\pm)} \right) \right)$$

$$- \sqrt{-g}g^{tt} g^{ii} \left(\omega \pm A_0^{(3)} \right)^2 \bar{X}_i^{(\pm)} = 0 \,, \tag{5.3.40}$$

---

[3]In the language of [18] we consider type II fluctuations, with type I fluctuations to be considered in the next subsection. Looking ahead, it turns out that type III fluctuations condense after type I fluctuations and we will not consider them in detail here.

which are equivalent to

$$D^u \left(\partial_u \bar{X}_i^{(\pm)} \right) + \nabla^j \left(\partial_j \bar{X}_i^{(\pm)} - \partial_i \bar{X}_j^{(\pm)} \right) - g^{tt} \left(\omega \pm A_0^{(3)} \right)^2 \bar{X}_i^{(\pm)} = 0. \qquad (5.3.41)$$

In order to solve these equations, we make a factorised ansatz for $\bar{X}_i$, as a product of radial and angular functions, and expand the angular part $\bar{X}_i^{\bar{\Omega}_3}(\bar{\Omega}_3)$ on $\bar{S}^3$ in terms of vector spherical harmonics, Π_i. In general, the fluctuations could also depend on a direction on internal sphere S^3. However, as mentioned before, we will focus only on singlets under the global $SO(4)$ symmetry group. Also, while there exists three type of vector spherical harmonics on $\bar{S}^3$, it has been argued in [18, 71], that for fluctuations of the vector field which are taking place in $\bar{S}^3 \subset AdS_5$, only $\Pi_i^{l,\pm}$ which transform in $\left(\left(\frac{l \mp 1}{2}, \frac{l \pm 1}{2} \right) \right), l \geq 1)$ irreducible representations of $SO(4)$ are relevant. Hence we expand the fluctuations as

$$\bar{X}_i^{(\pm)}(u, \omega, \bar{\Omega}_3) = \sum_{\bar{l}, s = \pm} \bar{\Phi}_{\omega, \bar{l}, s}^{(\pm)}(u) \Pi_i^{\bar{l}, s}, \qquad (5.3.42)$$

where the index $(\pm)$ refers to the two linear combinations of modes as defined in (5.3.39), and the $\pm$ index refers to the value of the index s labelling the vector spherical harmonics.

The spherical harmonics satisfy the identities

$$\nabla_i \nabla^i \Pi_j^{l,\pm} - R_j^k \Pi_k^{l,\pm} = -(l+1)^2 \Pi_j^{l,\pm},$$

$$\epsilon^{ijk} \nabla_j \Pi_k^{l,\pm} = \pm (l+1) \Pi_{l,\pm}^i, \qquad (5.3.43)$$

$$\nabla^i \Pi_i^{l,\pm} = 0,$$

Using these identities the equation for the vector fluctuations can be rewritten as

$$\bar{\Phi}_{\omega, \bar{l}, s}^{(\pm)\prime\prime}(u) + \frac{\partial_u \left(\sqrt{-g(u)} g^{uu}(u) P(u) \right)}{\left(\sqrt{-g(u)} g^{uu}(u) P(u) \right)} \bar{\Phi}_{\omega, \bar{l}, s}^{(\pm)\prime}(u)$$

$$- \frac{1}{g^{uu}(u)} \left[g^{tt}(u) \left(\omega \pm A_0^{(3)}(u) \right)^2 + (\bar{l}+1)^2 P(u) \right] \bar{\Phi}_{\omega, \bar{l}, s}^{(\pm)}(u) = 0, \quad (5.3.44)$$

where the $\pm$ sign in front of A_0 in the equation is correlated with the $(\pm)$ sign on the $\bar{\Phi}^{(\pm)}$ and $P(u)$ is the inverse of the u-dependent part of the the metric factor in front of $\mathrm{d}\bar{\Omega}_3^2$. We should note that this equation is independent of the quantum number

$s = \pm 1$, which will be different when we start looking at the vector fluctuations in the direction of the internal sphere. In the case of zero temperature the fluctuation equation becomes (see also [18])

$$\bar{\Phi}_{\omega,\bar{l}}^{(\pm)''}(u) + \frac{\partial_u \left(u^3 \left(1 + \frac{R^2}{4u^2} \right) \left(1 - \frac{R^2}{4u^2} \right) \right)}{u^3 \left(1 + \frac{R^2}{4u^2} \right) \left(1 - \frac{R^2}{4u^2} \right)} \bar{\Phi}_{\omega,\bar{l}}^{(\pm)'}(u)$$

$$+ \left[\frac{R^4}{u^4 \left(1 + \frac{R^2}{4u^2} \right)^2} (\omega \pm \mu)^2 - \frac{R^2}{u^4 \left(1 - \frac{R^2}{4u^2} \right)^2} (\bar{l} + 1)^2 \right] \bar{\Phi}_{\omega,\bar{l}}^{(\pm)}(u) = 0 . \quad (5.3.45)$$

This equation is very similar to (5.3.33), and can again be cast in Schrödinger form. We then find that the spectrum of vector fluctuations for the $\bar{l}$-th spherical harmonics is given by

$$(\omega \pm \mu)R = (3 + \bar{l} + 2n) \quad n = 0, 1, 2, 3.... \quad \bar{l} = 1, 2, 3.... , \quad (5.3.46)$$

Here n is again the main quantum number, and $\bar{l}$ is an $SO(4)$ quantum number corresponding to the sphere $\bar{S}^3 \subset AdS_5$. We see that the result is again the same as the one in [18] if we consider $SO(4)$ singlets (i.e. set $l = 0$), except that the chemical potential shifts the frequency $\omega \to \omega \pm \mu$.

From equation (5.3.46) we see that for a critical value of the chemical potential given by $\mu_{\text{crit}} = 4/R$, the lowest lying mode $\bar{l} = 1$ will become massless. Therefore, we expect that when the chemical potential is larger than this value, the system potentially becomes unstable.

The Charged Scalar Fluctuations

Let us now consider fluctuations of the vector field in the direction of the internal $S^3 \subset S^5$, which are dual to an $SO(4)$ charged scalar field in the gauge theory. Since the WZ term in the action is now non-zero, when considering fluctuations, we have to modify the action from (5.3.36) by adding the term

$$S_{WZ} = \frac{T_{D7} \pi^2 R^4}{\lambda} \int tr(C \wedge F \wedge F), \quad \mathrm{d}C = \frac{4}{R} \text{Vol}(AdS_5). \quad (5.3.47)$$

Similarly as before, we make an ansatz as in (5.3.35) except that the index i is now taking values in the internal S^3. In addition, we will also allow the fluctuations to

depend on both S^3 and $\bar{S}^3$ variables. In order to decouple the equations of motion we redefine variables as in (5.3.39) and make a factorised ansatz

$$X_i^{(\pm)}(u, \omega, \Omega_3, \bar{\Omega}_3) = e^{-i\omega t}\Phi^{(\pm)}(u)\bar{Y}^{\bar{l}}(\bar{\Omega}_3)\Pi_i^{l,s}(\Omega_3)\,, \tag{5.3.48}$$

where the index $(\pm)$ refers to the sign in the linear combination (5.3.39), $\bar{Y}^{\bar{l}}(\bar{\Omega}_3)$ is the scalar spherical harmonic of mode $\bar{l}$ on $\bar{S}^3$, i denotes the index in the direction of the internal S^3, and the index $s = \pm 1$. Also to shorten the notation we have suppressed indices on the functions $\Phi^{(\pm)}$, which should really also carry indices $(\omega, s, \bar{l}, l)$.

Following the same procedure as for scalars and the other gauge components we arrive at the equation for the fluctuations (see also [18])

$$\partial_u^2\Phi^{(\pm)} + \frac{\partial_u(u^5\left(1 + \frac{R^2}{4u^2}\right)\left(1 - \frac{R^2}{4u^2}\right)^3)}{u^5\left(1 + \frac{R^2}{4u^2}\right)\left(1 - \frac{R^2}{4u^2}\right)^3}\partial_u\Phi^{(\pm)} + \frac{R^2}{u^4\left(1 + \frac{R^2}{4u^2}\right)^2}(\omega \pm \mu)^2\Phi^{(\pm)}$$
$$- \left[(l+1)^2 + \bar{l}(\bar{l}+2)\frac{R^2}{u^2\left(1 - \frac{R^2}{4u^2}\right)^2} + 4s(l+1)\right]\frac{1}{u^2}\Phi^{(\pm)} = 0\,, \tag{5.3.49}$$

where the sign in the $(\omega \pm \mu)$ is the same as for $\Phi^{(\pm)}$. We should note that this equation explicitly depends on the quantum number s, which is labelling the vector harmonics on S^3. This is in contrast to the previous case for the equation for vector fluctuations on $\bar{S}^3$.

Putting equation (5.3.49) in Schrödinger form, like we did for the other fluctuations, we obtain for the spectrum

$$(\omega \pm \mu)R = 3 + 2s + l + 2n + \bar{l} \qquad \text{where}$$

$$\bar{l} = 0, 1, 2, \dots \quad l = 1, 2, 3, \dots \quad n = 0, 1, 2, \dots \quad s = \pm 1\,. \tag{5.3.50}$$

This is the same as (4.31) of [18] except for the shift $\omega \to \omega + \mu$. Let us also note that the lowest lying excitation carries quantum numbers $(\bar{l} = 0, l = 1, s = -1, n = 0)$, and this mode will reach zero frequency when $\mu > \mu_{\text{crit}} = 2/R$.[4]

---

[4]The fact that this excitation has the lowest mass at $\mu = 0$ was also observed in [18], but no attempt was made to study its condensation under the influence of a chemical potential.

5.4 Perturbative Analysis of the Homogeneous Vacuum at $T \neq 0$

In the previous section we have observed that the homogeneous isotropic ground state at non-zero chemical potential and zero temperature was unstable under both scalar and vector fluctuations. We would now like to see how is this modified once the temperature is turned on, paying particular attention to the order in which the instabilities set in as a function of temperature.

We should emphasise that in contrast to the zero temperature case, where all fluctuations have real frequency ω (corresponding to stable mesonic scalar and vector particles), at finite temperature (above the Hawking-Page transition), even in the absence of chemical potential all fluctuation frequencies have a non-vanishing imaginary part. When the chemical potential is zero the imaginary part of these frequencies are negative, corresponding to the fact that these excitations are decaying in time, i.e. that they describe quasi-stable particles. However, as the chemical potential is turned on, if there is indeed an instability present, we expect that the negative imaginary part of the frequencies will become positive, i.e. that a decaying excitation would become an exponentially growing mode, which signals an instability. In what follows, we will therefore focus on studying the imaginary part of the quasi-normal modes of the system.

We start our analysis by looking at the scalar fluctuations, and repeat the procedure similar to that at zero temperature. Again, we use the metric on the S^5 as in (5.3.25), keeping only the transverse scalar $\Psi(t, u)$ nonzero (see equation (5.3.27)) and making it depend only on time and the radial direction u. As argued before, such excitation is consistent with the full equations of motion, and should correspond to the lowest energy mode, an S-wave on $\bar{S}^3$. The induced metric on the D7-brane world-volume is then

$$
\mathrm{d}s^2 = -\frac{2\rho_H^2 F(u)}{u R^2 W(u)} \mathrm{d}t^2 + 2\frac{\rho_H^2}{u} W(u) \mathrm{d}\bar{\Omega}_3^2 + \frac{R^2}{4u^2 F(u)} \mathrm{d}u^2
$$
$$
+ R^2 \left(1 - \frac{\Psi(t, u)^2}{R^2}\right) \mathrm{d}\Omega_3^2 + \left(\frac{\partial\Psi(t, u)}{\partial t} \mathrm{d}t + \frac{\partial\Psi(t, u)}{\partial u} \mathrm{d}u\right)^2, \quad (5.4.51)
$$

where

$$F(u) = 1 - u^2 , \quad W(u) = 1 - \frac{uR^2}{4\rho_H^2} . \tag{5.4.52}$$

As before, we Fourier transform the scalar $\Psi(t, u)$ and make the ansatz that it is pointing in the direction orthogonal to the $A_0^{(3)}\tau^3$ in colour space,

$$\Psi(t, u) = \int \frac{\mathrm{d}\omega}{2\pi} e^{-i\omega t} (\Psi_\omega^{(1)}(u)\tau^1 + \Psi_\omega^{(2)}(u)\tau^2) . \tag{5.4.53}$$

We then again change variables as

$$\Psi_\omega^{(\pm)}(u) = \Psi_\omega^{(1)}(u) \pm i\Psi_\omega^{(2)}(u) , \tag{5.4.54}$$

so that the equations for the $\Psi^{(\pm)}$ fluctuations decouple and are given by[5]

$$\frac{\partial_u \left(\frac{W(u)F(u)}{u} \partial_u \Psi_\omega^{(\pm)}(u) \right)}{\frac{W(u)F(u)}{u}} + \frac{R^4 W(u)}{8u\rho_H^2 F(u)^2} \left(\omega \pm A_0^{(3)}(u) \right)^2 \Psi_\omega^{(\pm)}(u)$$

$$+ \frac{3}{4u^2 F(u)} \Psi_\omega^{(\pm)}(u) = 0 . \tag{5.4.55}$$

We solve the fluctuation equation by imposing that the modes satisfy an incoming boundary condition at horizon,

$$\Psi_\omega^{(\pm)}(u) \Big|_{u \approx 1} = (1 - u)^{-i\omega/(4\pi T)} (1 + \mathcal{O}(1 - u)) . \tag{5.4.56}$$

The equations for the vector fluctuations are derived in a similar way. Let us first consider the vector fluctuations which are dual to vectors. We take them to be singlets under the global $SO(4)$ ($l = 0$), and orthogonal to the isospin chemical potential in the gauge group as we did at zero temperature, see (5.3.35). Following steps similar to those at zero temperature, instead of $a_i^{(1)}, a_i^{(2)}$, we introduce a new pair of variables $X_i^{(\pm)}$, as in (5.3.39) and Fourier expand it in spherical harmonics as in (5.3.42). Hence, we arrive at the equations of motion for these fluctuations

$$\partial_u^2 \bar\Phi_\omega^{(\pm)s,\bar{l}} + \frac{\partial_u F(u) \partial_u \bar\Phi_\omega^{(\pm)s,\bar{l}}}{F(u)} - (\bar{l} + 1)^2 \frac{R^2}{8\rho_H^2 W(u)F(u)u} \bar\Phi_\omega^{(\pm)s,\bar{l}}$$

$$+ \frac{R^4 W(u)}{8u\rho_H^2 F(u)^2} (\omega \pm A_0^{(3)})^2 \bar\Phi_\omega^{(\pm)s,\bar{l}} = 0 . \tag{5.4.57}$$

---

[5]Note that at $T = 0$, the equations only depend on $\omega - \mu$, and hence the critical chemical potential coincides with the frequency of the lightest mode. At $T > 0$ the $A_0^{(3)}$ component is no longer a constant, and obtaining the critical chemical potential is more complicated (physical states are no longer straight lines in the ω, μ plane).

As for scalars, we impose incoming boundary conditions at the black hole horizon

$$\bar{\Phi}_{\omega}^{(\pm)s,\bar{l}}\Big|_{u\approx1} = (1-u)^{-i\omega/(4\pi T)}(1 + \mathcal{O}(1-u)).\tag{5.4.58}$$

Finally, we turn to the vector fluctuations dual to the charged scalars. Following similar steps as we did at zero temperature we arrive at the equations governing these fluctuations (see equation (5.3.49))

$$\frac{\partial_u\left(\frac{W(u)F(u)}{u}\partial_u\Phi^{(\pm)}\right)}{\frac{W(u)F(u)}{u}} - (l+1)^2\frac{1}{4u^2F(u)}\Phi^{(\pm)} - \bar{l}(\bar{l}+2)\frac{R^2}{8\rho_H^2 W(u)F(u)u}\Phi^{(\pm)}$$

$$- \frac{s(l+1)}{u^2F(u)}\Phi^{(\pm)} + \frac{R^4W(u)}{8u\rho_H^2 F(u)^2}(\omega \pm A_0^{(3)})^2\Phi^{(\pm)} = 0.\tag{5.4.59}$$

where we have again suppressed the indices $(\omega, \bar{l}, l, s)$ on the functions Φ and we impose incoming boundary conditions at the horizon of the black hole

$$\Phi^{(\pm)}\Big|_{u\approx1} = (1-u)^{-i\omega/(4\pi T)}(1 + \mathcal{O}(1-u)).\tag{5.4.60}$$

In order to solve the fluctuation equations (5.4.55), (5.4.57) and (5.4.59), we use a shooting technique (see appendix A.1 and A.2 for more detail), in which we start from the horizon and look for modes that decay at infinity i.e. we look for the modes that describe normalisable excitations. These boundary conditions will be satisfied only for a discrete set of frequencies. We plot the imaginary parts of those frequencies for the scalar and two vectors, for fixed temperature and various values of the chemical potential μ, in figure 5.1.

We see that as the value of the chemical potential is increased, the imaginary parts of the frequencies, which were initially all negative, become less and less negative and approach zero. When the chemical potential exceeds a critical value, the imaginary parts become positive one by one, signalling the presence of unstable modes in the system. Similarly, the real parts of the frequencies are decreasing to zero as the chemical potential grows, signalling again the onset of an instability. For a particular value of the temperature presented on the left plot in the figure 5.1, we see that the vector dual to the gauge theory charged scalar remains the lightest in the spectrum and condenses first, followed by the transverse scalar and finally the vector.
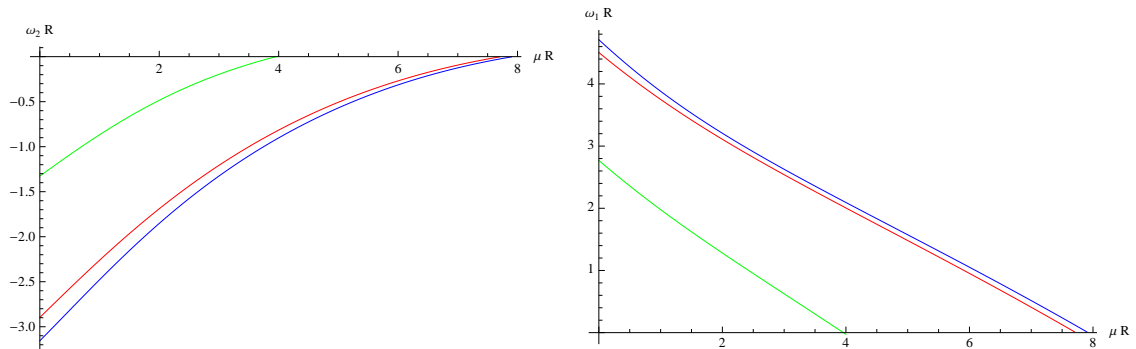
Figure 5.1: Plots of the imaginary (left) and real (right) parts of the frequencies for the lowest lying uncharged scalar fluctuation (red), the vector fluctuation (blue) and the charged scalar fluctuation (green), at fixed temperature $\pi T R = 2$, as a function of the chemical potential.

In general, one would expect that particles condense roughly when the chemical potential become of the order of their mass. It is thus of interest to look at the behaviour of the masses[6] as a function of temperature. Figure 5.2 shows the result of this analysis. We here observe another interesting phenomenon, namely that there is a crossover point at some critical value of the temperature, above which the lightest vector becomes lighter than the transverse scalar. This suggests that above the crossover temperature, the lightest vector would condense before the lightest transverse scalar, if it had not been for the $SO(4)$ charged scalar that condenses even earlier. One can indeed see that the corresponding imaginary parts cross as well, approximately at this point, see figure 5.3.

For large TR, the results read

$$\text{charged scalar}: \quad \mu_{\text{crit}} R \approx 2.00 \pi T R - \frac{2.00 \times 0.05}{4\pi T R} + \cdots,$$

$$\text{vector}: \quad \mu_{\text{crit}} R \approx 4.00 \pi T R - \frac{4.00 \times 0.05}{4\pi T R} + \cdots, \qquad (5.4.61)$$

$$\text{uncharged scalar}: \quad \mu_{\text{crit}} R \approx 4.16 \pi T R - \frac{4.16 \times 1.00}{4\pi T R} + \cdots.$$

The leading order terms should agree with those obtained in the Poincaré patch,

---

[6]We use pole masses here for convenience as they are easy to obtain from the quasi-normal mode analysis, and the intuition we want to verify is anyhow qualitative.
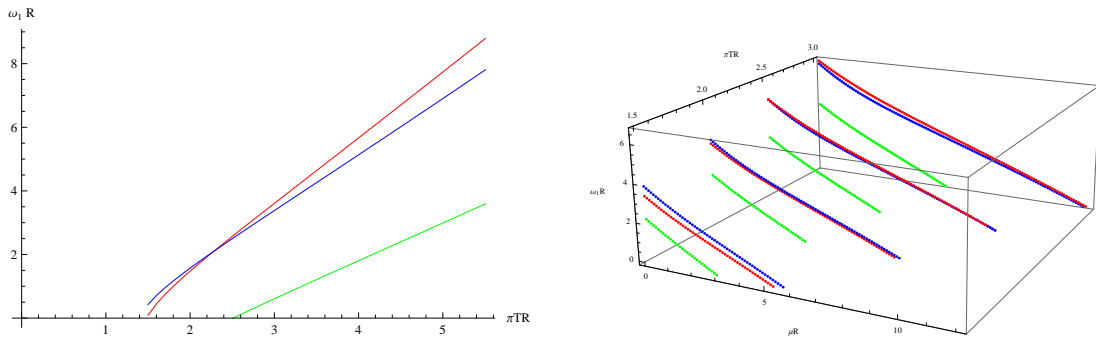
Figure 5.2: Left is a plot of the real parts of the frequencies for the various modes (colours as in figure 5.1) as functions of the temperature at fixed value $\mu R = 5$ of the chemical potential. The plot on the right shows the real parts of the frequencies as functions of both temperature and chemical potential.

though to our knowledge only the one for the vector has been computed in the literature [68, 70, 73]. The result for the critical chemical potential of [68, 70] (when extrapolated to zero bare quark mass) seems to be somewhat larger than ours, which may be due to the fact that we have used a Yang-Mills truncation rather than the full DBI action.

5.5 The New Ground States at Zero and Finite Temperature

In the previous two sections we have seen that for large enough chemical potential the homogeneous ground state on $\bar{S}^3 \subset AdS_5$ becomes unstable under both scalar and various components of vector fluctuations. This is happening both at zero and non-zero temperature. In particular we observe that, at zero temperature, vector fluctuations in the direction of the internal $S^3 \subset S^5$ are the first to became unstable. As the temperature is increased, these vector components remain the first to become unstable. On the other hand, the ordering in which the other components of the vector fluctuations and the scalar fluctuations become unstable is dependent on the temperature, as there is a 'crossover' temperature above which all vector components first become unstable.
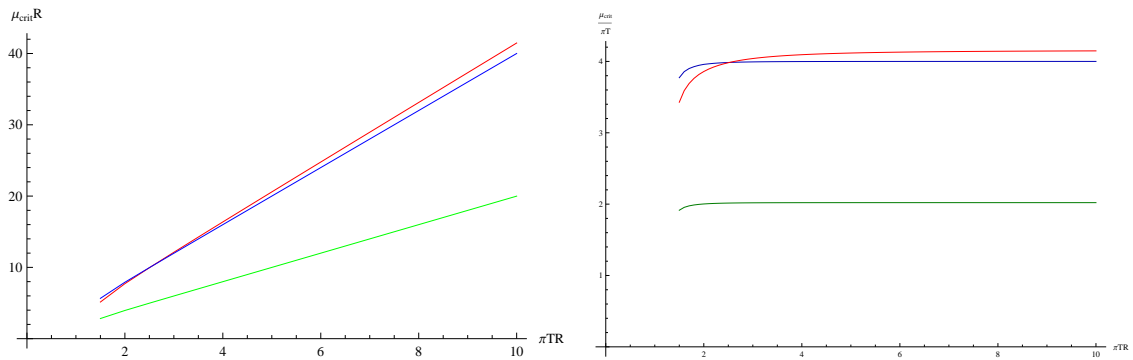
Figure 5.3: Critical chemical potential as function of temperature, in two different dimensionless combinations. The figure on the right shows more clearly what happens in the $TR \to \infty$ limit, which can be interpreted as the large radius limit at fixed temperature.

Our previous analysis was done in perturbation theory, i.e. at the linearised level. So we would now like to see if the instabilities which we have found are present in the full non-linear theory, and to explore the new ground state in which the system settles for large enough values of the chemical potential.

5.5.1   The New Ground State at Zero Temperature

In section 5.3.2 we have observed that as the chemical potential is turned on, when its value reaches $\mu \geq 2/R$, the lowest lying mode of the vector component in the internal S^3, becomes massless, signalling the onset of possible instability in the system. We have also seen that for even larger values of the chemical potential, the scalar becomes massless at $\mu \geq 3/R$ and the other components of the vector develop an instability for $\mu \geq 4/R$.

To see whether the appearance of these massless modes indeed signals a real instability, we will now turn to the full non-linear theory and try to explicitly construct the new ground state to which the system would evolve as a consequence of the instability. As the perturbative analysis suggests that vector components in the internal S^3 direction are first to condense, we will start the analysis of the new ground state by turning on only those components. We will later, for comparison, also analyse possible ground states due to condensation of the other fluctuations,

and verify that those always have higher energy than the scalar condensate.

When writing down an ansatz for the scalar condensate ground state, we will use the fact that in perturbation theory, the first unstable mode is an $\bar{l} = 0, l = 1, n = 0, s = -1$ wave (where $\bar{l}$ labels modes in the $\bar{S}^3$ and l labels modes in the $S^3 \subset S^5$). As far as the A_0 component is concerned, at linearised level one cannot see the back-reaction of the scalar on the background value of this field, so in principle one cannot say if in the new ground state the A_0 component will start to depend on the angular coordinates or not.

As a simplest attempt we take A_0 to remain homogeneous, i.e. independent of the $\bar{S}^3$ angular coordinates. With this ansatz, potential problems in the equations of motion could originate from expression of the form "$A_\alpha A_\beta g_{S^3}^{\alpha\beta}$", which are now turned on due to the non-vanishing vector field in the direction of the internal sphere S^3. Since these terms will typically produce spherical harmonics of higher l-number we would need to balance them in the equations of motion. However, we expect that the ground state would originate from condensation of only the lowest harmonic, so that higher l-harmonics are not needed. It is possible to reconcile these two observations if the "$A_\alpha A_\beta g_{S^3}^{\alpha\beta}$" expression is independent of the angular coordinates. This can indeed be achieved for a particular linear combination of spherical harmonics given by

$$\Pi_\alpha = \frac{ik_0}{K}\Pi_\alpha^{1,0,0,-1} + \frac{(k_1 + ik_2)}{K}\Pi_\alpha^{1,0,-1,-1} + \frac{(k_1 - ik_2)}{K}\Pi_\alpha^{1,0,1,-1}$$

$$\text{where} \qquad K \equiv \sqrt{k_0^2 + 2(k_1^2 + k_2^2)}, \quad (5.5.62)$$

and k_0, k_1, k_2 are three arbitrary real numbers which are not simultaneously vanishing, and (l, m_1, m_2, s) are the quantum numbers of the spherical harmonics. We should note here that value of these quantum numbers will be taken to be the same as those of the lowest lying excitation we have previously found in the perturbative

analysis. Explicitly, the spherical harmonics are given by

$$\Pi^{1,0,0,-1} = \frac{i}{2}\mathrm{d}\alpha + \frac{i}{2}\cos\beta\mathrm{d}\gamma$$

$$\Pi^{1,0,1,-1} = -\frac{1}{2\sqrt{2}}e^{-i\alpha}\mathrm{d}\beta - \frac{i}{2\sqrt{2}}\sin\beta e^{-i\alpha}\mathrm{d}\gamma \qquad (5.5.63)$$

$$\Pi^{1,0,-1,-1} = -\frac{1}{2\sqrt{2}}e^{i\alpha}\mathrm{d}\beta + \frac{i}{2\sqrt{2}}\sin\beta e^{i\alpha}\mathrm{d}\gamma\,,$$

where α, β, γ are Euler coordinates on $S^3 \subset S^5$,

$$\mathrm{d}s_{S^3}^2 = \frac{1}{4}(\mathrm{d}\alpha^2 + \mathrm{d}\beta^2 + \mathrm{d}\gamma^2 + 2\cos\beta\mathrm{d}\alpha\mathrm{d}\gamma)\,. \qquad (5.5.64)$$

It is also useful to keep in mind that

$$(\Pi_i^{l,m_1,m_2,s})^* = -(-1)^{m_1-m_2}\Pi_i^{l,-m_1,-m_2,s}\,. \qquad (5.5.65)$$

Our ansatz for the new ground state is

$$A_0 = A_0^{(3)}(u)\tau^3\,, \qquad A_\alpha = R\eta(u)\Pi_\alpha(\Omega_3)\tau^1 \qquad (5.5.66)$$

Plugging this into equations of motion, and using identities (5.3.43) we get an equation for $A_0(u)$

$$\frac{\partial_u\left((\partial_u A_0^{(3)})u^3\left(1 - \frac{R^2}{4u^2}\right)^3 / \left(1 + \frac{R^2}{4u^2}\right)\right)}{u^3\left(1 - \frac{R^2}{4u^2}\right)^3 / \left(1 + \frac{R^2}{4u^2}\right)} - \frac{R^2}{u^2}(\eta(u))^2 A_0^{(3)}(u) = 0\,, \qquad (5.5.67)$$

and an equation for the function $\eta(u)$

$$\frac{\partial_u\left(\partial_u\eta(u)u^5\left(1 + \frac{R^2}{4u^2}\right)\left(1 - \frac{R^2}{4u^2}\right)^3\right)}{u^5\left(1 + \frac{R^2}{4u^2}\right)\left(1 - \frac{R^2}{4u^2}\right)^3} + \frac{R^4}{u^4\left(1 + \frac{R^2}{4u^2}\right)^2}(A_0^{(3)}(u))^2\eta(u) + \frac{4}{u^2}\eta(u) = 0\,. \qquad (5.5.68)$$

Note that these are independent of the parameter K, which only appears in the angular part of the equations of motion, which is automatically satisfied for our ansatz.

Equations (5.5.67), and (5.5.68) are written in the non-compact coordinate u for which the AdS centre is at $u = R/2$ and the boundary is at $u = \infty$. However, for numerical considerations it is more convenient to perform a coordinate change to
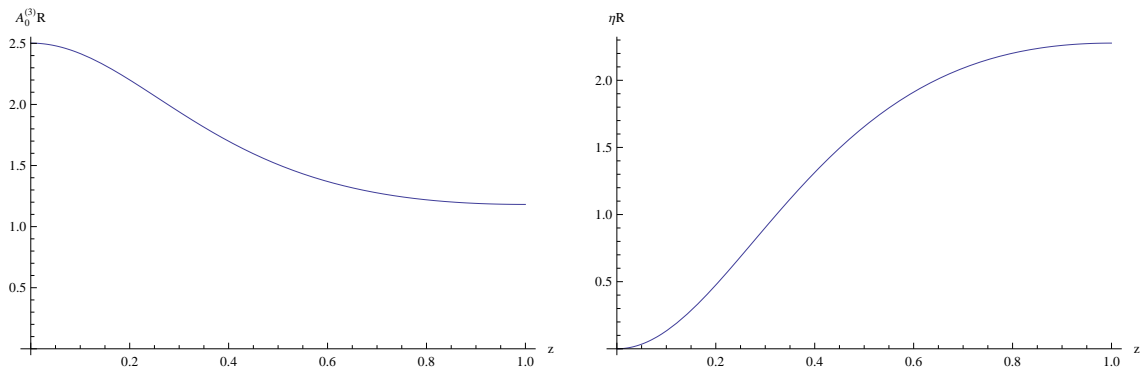
Figure 5.4: Profile of the fields A_0 (left) and η (right) of the charged scalar condensate, evaluated at $\mu R = 2.5$. The boundary is at $z = 0$ and the AdS centre is at $z = 1$.

compact coordinates $z = R/2u$, so that the AdS origin is at $z = 1$, and the boundary at $z = 0$. The equations of motion then are given by

$$\partial_z^2 A_0^{(3)}(z) + \frac{1 + 8z^2 + 3z^4}{z^5 - z} \partial_z A_0^{(3)}(z) - \frac{R^2}{z^2} \eta(z)^2 A_0^{(3)}(z) = 0 \,,$$

$$\partial_z^2 \eta(z) + \frac{3 + 4z^2 + 5z^4}{z^5 - z} \partial_z \eta(z) + \left(\frac{4}{z^2} + \frac{4R^2}{(1 + z^2)^2} A_0^{(3)}(z)^2 \right) \eta(z) = 0 \,. \tag{5.5.69}$$

We are interested in the solutions of these equations that are regular everywhere, and in particular at the origin of AdS space. This removes half of the solutions, as can be seen by looking at the $z \to 1$ limit of the above equations. Namely, assuming that A_0 and η are regular at the AdS origin, it is easy to see that the above equations reduce to the conditions that the first derivatives of A_0 and η are vanishing at the origin. Hence, the general regular solution will be parametrised by two parameters a, b. We then solve the equations of motion by shooting from the AdS origin, and look for the solutions at the boundary such that η is normalisable, while A_0 is not. This normalisability condition further reduces the number of parameters by one. Hence in the expansion near infinity

$$A_0^{(3)} = \mu - \rho z^2 + \cdots \,, \quad A_\alpha^{(1)} = R \rho_\eta \Pi_\alpha z^2 + \cdots \,. \tag{5.5.70}$$

both the densities ρ and ρ_η are functions of the chemical potential μ.

We plot the radial profile of the functions $A_0(z)$ and $\eta(z)$ for one particular solution in figure 5.4. As required, we see that the solution is regular everywhere, and
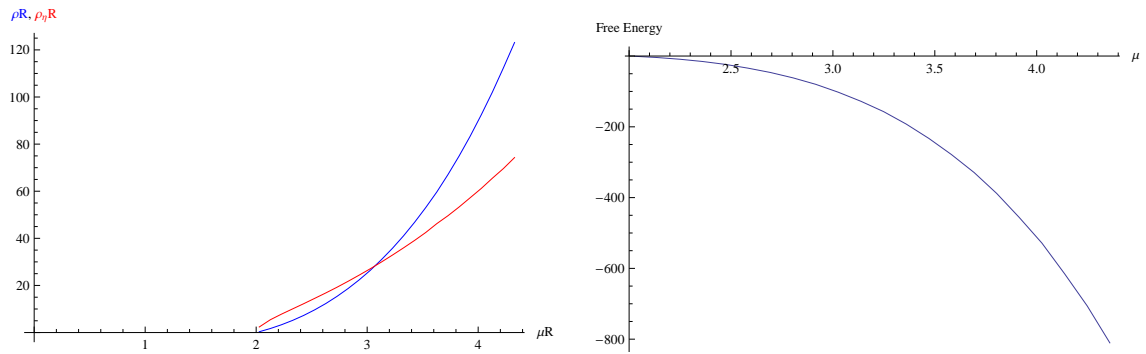
Figure 5.5: The plot on the left shows the isospin density ρR (blue) and scalar density $\rho_\eta R$ (red) of the charged scalar condensate as functions of the isospin chemical potential. The plot on the right shows the scaled free energy as function of chemical potential.

approaches the origin of AdS with vanishing derivative, so that no cusp is present. We also study various solutions for different values of chemical potential, see figure 5.5. The shooting procedure shows that there is a critical value of the chemical potential $\mu_{\mathrm{crit}} \sim 2/R$ below which there is no nontrivial solution present. Above $\mu = \mu_{\mathrm{crit}}$ a nontrivial condensate of scalar particles forms, and in the neighbourhood of μ_{crit}, this condensate is to a good approximation given by

$$\rho_\eta = \begin{cases} 0 & \text{for } \mu < \mu_{\mathrm{crit}} \\ \sqrt{\mu - \mu_{\mathrm{crit}}} & \text{for } \mu > \mu_{\mathrm{crit}} \,. \end{cases} \tag{5.5.71}$$

We have also evaluated the free energy for various values of the chemical potential (see figure 5.5), and observed that it is less than the (vanishing) free energy of the trivial configuration, which is in agreement with the statement that this is the ground state.

In summary, our analysis shows that for large enough value of the chemical potential, this system undergoes a second order phase transition in which the homogeneous isotropic solution is replaced with a non-isotropic one. The order parameter in this transition is the density ρ_η, and the critical exponent is the same as in the Landau-Ginsburg theory with positive quartic potential.

In order to complete the picture, and to show that (as expected from the perturbative analysis) the charged scalar condensate is always the one with the lowest
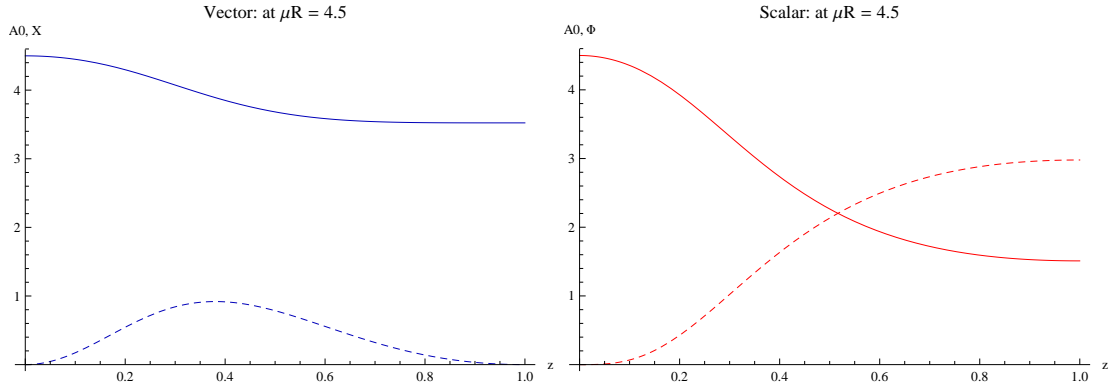
Figure 5.6: Left: a plot of the functions $A_0(z)$ (solid curve) and $\psi(z)$ (dashed curve) for the vector solution. Right: plots of the functions $A_0(z)$ (solid) and Φ (dashed) for the scalar configuration, both evaluated at a fixed value of chemical potential $\mu R = 4.5$.

energy, we will now construct condensates of the transverse scalar and the vector, and show that their energies are always higher than the one of the charged scalar. When constructing the transverse scalar ground state we recall that perturbative analysis suggested that the s-wave is the first excitation of the scalar which becomes massless. Hence we make a homogeneous (i.e. only u-dependent) ansatz as follows

$$A = A_0^{(3)}(u)\tau^3\,\mathrm{d}t\,, \quad \Phi = \Phi^{(1)}(u)\tau^1\,, \tag{5.5.72}$$

where the vector A_0 is present to account for the non-vanishing chemical potential, while all other vector components are zero. The equations of motion for the fields (A_0, Φ) are given by

$$\partial_z^2 A_0^{(3)}(z) + \frac{1 + 8z^2 + 3z^4}{z^5 - z}\partial_z A_0^{(3)}(z) - \frac{R^2}{z^2}\Phi(z)^2 A_0^{(3)}(z) = 0\,,$$
$$\partial_z^2 \Phi(z) + \frac{3 + 4z^2 + 5z^4}{z^5 - z}\partial_z \Phi(z) + \left(\frac{3}{z^2} + \frac{4R^2}{(1+z^2)^2}A_0^{(3)}(z)^2\right)\Phi(z) = 0\,. \tag{5.5.73}$$

Similarly, when constructing the ground state originating from vector condensation, we start with an ansatz which is similar to that of the vector component dual to a charged scalar, i.e. we write

$$A_0 = A_0^{(3)}(u)\tau^3\,, \qquad A_{\bar\alpha} = \psi(u)\Pi_{\bar\alpha}(\bar\Omega_3)\tau^1\,, \tag{5.5.74}$$
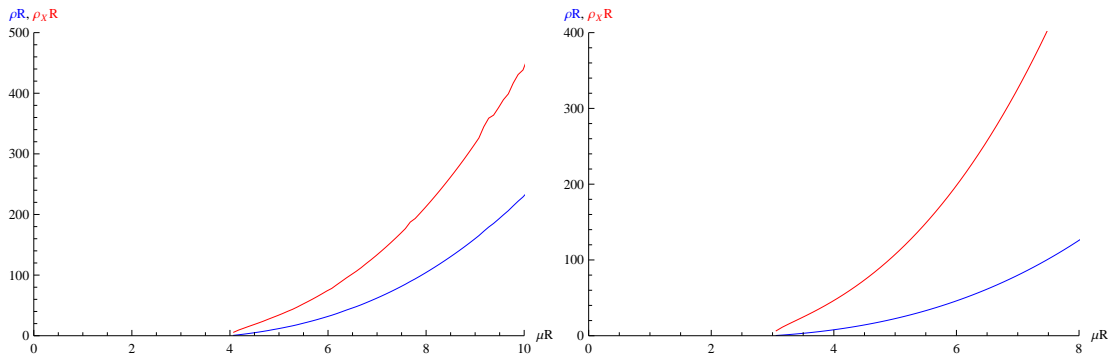
Figure 5.7: Plots of the densities ρ (blue) and ρ_η (red), as a function of the chemical potential μ, at zero temperature, for the vector condensate (left) and scalar condensate (right).

where $\Pi_{\bar{\alpha}}$ is as in (5.5.66), except that the index $\bar{\alpha} = 1, 2, 3$ now refers to the $\bar{S}^3 \subset AdS_5$. The equations of motion then become

$$\partial_z^2 A_0^{(3)}(z) + \frac{1 + 8z^2 + 3z^4}{z^5 - z}\partial_z A_0^{(3)}(z) - \frac{4}{(1-z^2)^2}\psi(z)^2 A_0^{(3)}(z) = 0\,,$$

$$\partial_z^2 \psi(z) + \frac{1 + 3z^4}{z^5 - z}\partial_z \psi(z) + \left(\frac{4R^2}{(1+z^2)^2}A_0^{(3)}(z)^2 - \frac{16}{(1-z^2)^2}\right)\psi(z) = 0\,. \tag{5.5.75}$$

We should emphasise here that this equation is derived from an ansatz which uses spherical harmonics with $\bar{l} = 1, s = -1$, similar to the ansatz we used when we constructed the state for the vector dual to a charged scalar. However, we have also seen in the perturbative analysis that vector fluctuations in the direction of $\bar{S}^3 \subset AdS_5$ are insensitive to the quantum number s, unlike the fluctuation in direction of $S^3 \subset S^5$. Therefore, it should also be possible to construct an alternative state with spherical harmonics with $\bar{l} = 1, s = 1$. This is indeed this the case, and the free energy of this state is the same as for the state with $\bar{l} = 1, s = -1$.

Equations (5.5.73) and (5.5.75) are solved in the same fashion as equation (5.5.69), that is by the shooting method as described in appendix A and imposing that the solution is regular everywhere and in particular at the origin of AdS_5. The solutions for the radial functions (A_0, Φ) for the scalar configuration and (A_0, ψ) for the vector are plotted in figure 5.6. We also plot the densities for both configurations (defined analogous to (5.5.70)) as functions of the chemical potential, see figure 5.7.

In order to compare various configurations we plot the free energies for all three
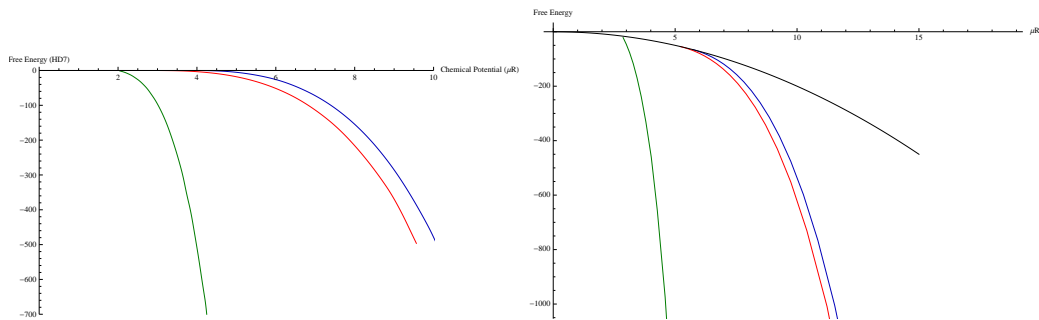
Figure 5.8: Scaled free energy of the zero-temperature (left) and the finite-temperature (right) condensates as a function of the dimensionless chemical potential. The vector is plotted in blue, the scalar in red, the charged scalar green. The black curves denote the old ground state.

states, see figure 5.8. As expected from the perturbative analysis, we see that the state which originates from a condensation of the vector components which are dual to a charged scalar has the lowest free energy. We also see that as the chemical potential is increased, the difference between the free energies of the other two states and the true ground state becomes larger. It is, however, likely that new instabilities will kick in at some point. Investigating that in detail would require at the least a perturbative analysis around this new ground state, which we will not attempt here.

5.5.2   The New Ground State at Finite Temperature

So far we have seen that at zero temperature, the ground state originates from the condensation of vector components which are dual to a charged scalar, exactly as perturbation theory suggested. We now want to see what is happening with this new ground state as the temperature is turned on. We start by making the same ansatz as at zero temperature, see (5.5.66). The equations of motion in the coordinates (5.2.12) are given by

$$\partial_v^2 A_0^{(3)}(v) - \frac{\Lambda - 1}{4(\Lambda - v)(1 - v)^2 v} R^2 \eta(v)^2 A_0^{(3)}(v) = 0 \,, \qquad (5.5.76)$$

together with

$$\partial_v^2 \eta(v) + \left(\frac{1}{1-v} + \frac{1}{v} - \frac{1}{\Lambda - v} \right) \partial_v \eta(v)$$

$$+ \frac{\Lambda - 1}{(\Lambda - v)(1-v)^2 v} \left(1 + \frac{(2-\Lambda)(1-v)R^2}{4(\Lambda - v)v} A_0^{(3)}(v)^2 \right) \eta(v) = 0 \,. \quad (5.5.77)$$

We are interested in finding regular solutions to these equations. It is easy to see that the solutions which are regular are parametrised by two free parameters. A general, perturbative expansion of the solution near the black hole horizon which is regular is given by

$$A_0^{(3)}(v) = av + \frac{ab^2(\Lambda - 1)}{8\Lambda R^2} v^2 + \mathcal{O}(v^3) \,,$$

$$\eta(v) = b - \frac{(\Lambda - 1)b}{\Lambda} v - \frac{12b(\Lambda - 1) + (2-\Lambda)(\Lambda - 1)a^2 R}{16\Lambda^2} v^2 + \mathcal{O}(v^3) \,,$$

$$(5.5.78)$$

i.e. a regular solution is parametrised by two real numbers a, b. We also see that the general regular solution for A_0 vanishes at the horizon, as required by global regularity. We solve this system of equations again using a shooting method with two free parameters. As at zero temperature, we require in addition that the solution for η is normalisable at infinity, or explicitly

$$A_0^{(3)}(v) = \mu - \rho(1-v) + \mathcal{O}((1-v)^2) \,, \quad \eta(v) = \rho_\eta(1-v) + \mathcal{O}((1-v)^2) \,. \quad (5.5.79)$$

This is possible only for a particular pair of parameters a, b, or in other words both densities ρ, ρ_η are functions of the chemical potential. An example of the radial profiles for a regular solution is plotted in figure 5.9. We also plot both densities as a function of chemical potential (see right plot on figure 5.9). We observe that, just as at zero temperature, the densities increase as the chemical potential is increased.

As for zero temperature, we should make sure that possible alternative states which appear due to condensation of other unstable particles have a larger free energy (as suggested by perturbation theory). We start with the scalar ground state. We make the same ansatz for the ground state, as we did at the zero temperature,
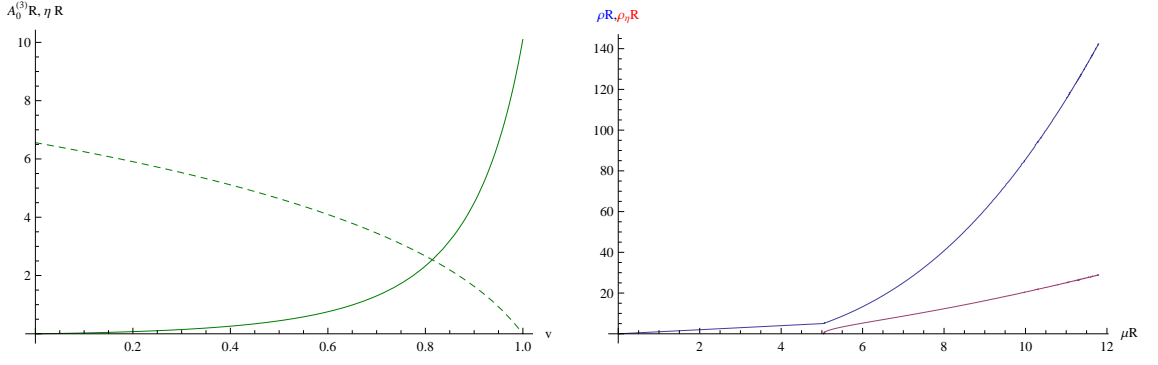
Figure 5.9: Left are plots of profile of the fields A_0 (solid) and η (dashed) for the charged scalar, evaluated at $\pi T R = 2.5$ and $\mu R = 10.1$. The boundary is at $v = 1$ and horizon at $v = 0$. Right plot is for densities ρ (blue) and ρ_η (red), as function of chemical potential μ, at fixed temperature $\pi T R = 2.5$.

see (5.5.72). The equations of motion in the coordinates (5.2.12) are given by

$$\partial_v^2 A_0^{(3)}(v) - \frac{\Lambda - 1}{4(\Lambda - v)(1 - v)^2 v} \Phi(v)^2 R^2 A_0^{(3)}(v) = 0 \,,$$

$$\partial_v^2 \Phi(v) + \left(\frac{1}{1 - v} + \frac{1}{v} - \frac{1}{\Lambda - v} \right) \partial_v \Phi(v) \tag{5.5.80}$$

$$+ \frac{\Lambda - 1}{(\Lambda - v)(1 - v)^2 v} \left(1 + \frac{(2 - \Lambda)(1 - v)R^2}{4(\Lambda - v)v} A_0^{(3)}(v)^2 \right) \Phi(v) = 0 \,.$$

Similarly, the ground state originating from the vectors is derived starting with the ansatz (5.5.74). The equations of motion are given by

$$\partial_v^2 A_0^{(3)}(v) - \frac{2 - \Lambda}{4(\Lambda - v)(1 - v)v} \psi(v)^2 A_0^{(3)}(v) = 0 \,,$$

$$\partial_v^2 \psi(v) + \left(\frac{1}{v} - \frac{1}{\Lambda - v} \right) \partial_v \psi(v) \tag{5.5.81}$$

$$- \frac{2 - \Lambda}{(\Lambda - v)(1 - v)v} \left(1 - \frac{(\Lambda - 1)R^2}{4(\Lambda - v)v} A_0^{(3)}(v)^2 \right) \psi(v) = 0 \,.$$

As before we consider only regular solutions to the equations (5.5.80) and (5.5.81) and require that the solutions are normalisable. Sample solutions for rather arbitrary values of the temperature and chemical potential are plotted in figure 5.10. We have also evaluated the densities for these solutions, and find a qualitatively similar dependence on the chemical potential as before. We have also verified that indeed
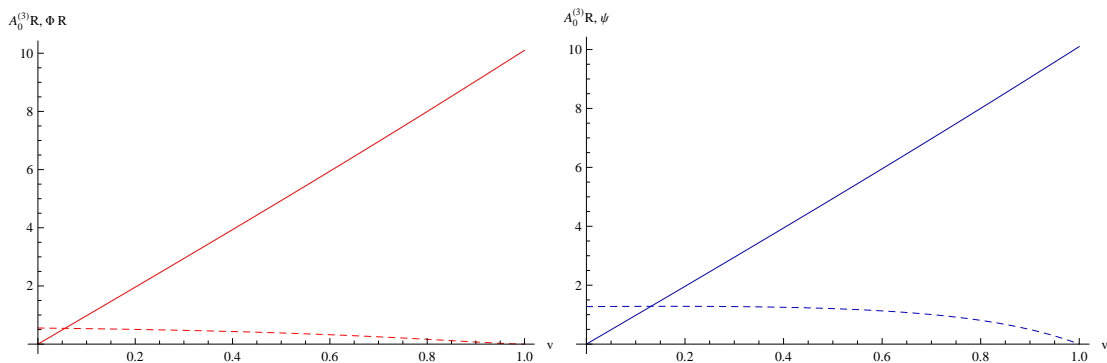
Figure 5.10: Plots of solutions $(A_0(z), \Phi(z))$, and $(A_0(z), \psi(z))$ for the scalar and vector condensates respectively, at fixed temperature $\pi T R = 2.5$ and chemical potential $\mu R = 4.5$ (the curve for A_0 is rather straight only because the plot is made for a chemical potential only slightly above the critical value).

the charge scalar always has a lower free energy than the condensate of the other particles, as predicted by perturbation theory.

Finally, we present in figure 5.11 the dependence of the charged scalar condensate densities on the temperature, for fixed chemical potential. This shows how increasing the temperature 'melts' the condensate.

5.6   Conclusion and Discussion

We have investigated some of the instabilities of the $\mathcal{N} = 2$ SYM theory on a three-sphere with the massless quark and the isospin chemical potential. At sufficiently high values of the chemical potential, in the gauge theory we found the instabilities of the vector, uncharged scalar and $SO(4)$ charged scalar. The mode that is unstable with the least value of the chemical potential is the $SO(4)$ charged scalar. This mode is thus the first mode to condense. By constructing the new ground state that uses the $SO(4)$ charged scalar as the additional basis, we found the free energy of the system with this new ground state is lower than the one with the old or the other ground states. This confirms the charged scalar new ground state is the true new ground state for this range of the chemical potential.

As the bases of the new ground state has the component of the $SO(4)$ charge
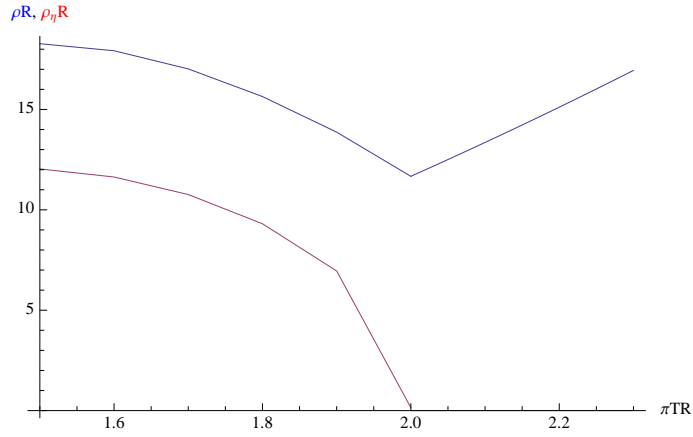
Figure 5.11: Dependence of the charged scalar ground state densities on TR at fixed chemical potential $\mu R = 4.005$.

scalar which is anisotropic in the three-sphere, the system with the new ground state has the global $SO(4)$ R-symmetry broken. As this story happens in the internal sphere, it still survives in the infinite volume limit where the Poincaré patch of $AdS_5 \times S^5$ spacetime is used in the gravity side.

The system also exhibits the cross-over behaviour in the fluctuation spectra of the scalar and the vector mesons as a function of the dimensionless temperature. It does not have any effects on the charged scalar condensation. However, it would yield an important influence when we consider the system with the higher chemical potential.

Chapter 6

Effects of a Magnetic Kalb-Ramond Field to the Meson Spectra and the New Ground States

In this chapter we will follow our work in progress [3]. We investigate the meson spectra and new ground states in $\mathcal{N} = 2$ SYM at zero temperature at strong coupling in compact space S^3 with a magnetic Kalb-Ramond field (magnetic B-field). For particular values of an external magnetic field, there is a range of quark masses called mass gap in which we still cannot find an appropriate solution. The analysis also shows the instability of the ground states when the external magnetic field increases to certain values.

6.1   Motivation

The magnetic effect to the strongly coupled system has been studied in many works such as [74–79]. One of the interesting influences is the catalysis of the chiral symmetry breaking that gives the fermion condensate [80–85]. This effect has been shown to be universal and should be accessed by every proper model [6]. Another interesting effect from the external magnetic field is the diminishing of the meson

new ground state in [86]. In our work, we will study the magnetic effect by using the holographic model. The setup is exactly the same as in the last chapter, except there is the B-field added in and we are also considering the massive quark. We will work in the gravity side and then map the quantity to the gauge theory by the boundary expansion to see if the diminishing of the new ground states and/or any other interesting effects arise.

6.2 Magnetic B-field and Holographic Quarks

6.2.1 DBI Action and Its EOMs with B-field Turned on

Here, the DBI action with non-zero B-field will be considered. We will show the equations of motion from the DBI action. The gauge symmetry at equations of motion level will be demonstrated. We find that the gauge field equations of motion are non-trivial even if gauge field is zero. Due to this constraint, we have to consider B-field depending on the radial coordinate[1] of the D7-brane.

Let us recall the DBI action

$$S = -T_{D7} \int d^8\sigma \sqrt{- \det(e_{ab} + 2\pi\alpha' F_{ab})}, \qquad (6.2.1)$$

where $e_{ab} = E_{\mu\nu}\partial_a x^\mu \partial_b x^\nu$ with $E_{\mu\nu} = G_{\mu\nu} + B_{\mu\nu}$. We obtain the equations of motion for the embedding function and for gauge field:

$$\partial_b \left(\sqrt{-\mathcal{E}}\mathcal{E}^{ba} E_{\nu\lambda} \frac{\partial x^\nu}{\partial \sigma^a} \right) + \partial_a \left(\sqrt{-\mathcal{E}}\mathcal{E}^{ba} E_{\lambda\nu} \frac{\partial x^\nu}{\partial \sigma^b} \right) - \sqrt{-\mathcal{E}}\mathcal{E}^{ba} \partial_\lambda E_{\mu\nu} \frac{\partial x^\mu}{\partial \sigma^a} \frac{\partial x^\nu}{\partial \sigma^b} = 0,$$
$$(6.2.2)$$

$$\partial_a(\sqrt{-\mathcal{E}}(\mathcal{E}^{ab} - \mathcal{E}^{ba})) = 0, \qquad (6.2.3)$$

where $\mathcal{E}^{ab}$ and $\mathcal{E}$ are inverse and determinant of $\mathcal{E}_{ab} = e_{ab} + 2\pi\alpha' F_{ab}$, respectively. Note that even though the gauge field vanishes, the equation (6.2.3) is still non-trivial[2]. In fact, the equations (6.2.2) and (6.2.3) are invariant under the gauge and

---

[1]This contrasts to [6], where the B-field ansatz is built from S^3 tetrads and does not depend on the radial coordinate.

[2]It seems that [6] missed the equation (6.2.3) which their B-field ansatz $B = (const) \sin\bar\theta d\bar\theta d\bar\phi$ contradicts.

tensor gauge transformations in (2.2.22) and (2.2.23). We consider the background metric in general form

$$
\begin{aligned}
ds^2 =& G_{tt}(r)dt^2 + G_{33}(r)(d\bar{\theta}^2 + \sin^2\bar{\theta}d\bar{\phi}^2 + \cos^2\bar{\theta}d\bar{\psi}^2) + G_{rr}(r)dr^2 \\
& + R^2\frac{d\chi^2}{1-\chi^2} + R^2\chi^2 d\kappa^2 + R^2(1-\chi^2)(d\theta^2 + \sin^2\theta d\phi^2 + \cos^2\theta d\psi^2),
\end{aligned}
\tag{6.2.4}
$$

and use the embedding

$$
\{t, r, \bar{\theta}, \bar{\phi}, \bar{\psi}, \theta, \phi, \psi, \chi, \kappa\} \rightarrow \{t, r, \bar{\theta}, \bar{\phi}, \bar{\psi}, \theta, \phi, \psi\}
\tag{6.2.5}
$$

with the embedding functions

$$
\{t, r, \bar{\theta}, \bar{\phi}, \bar{\psi}, \theta, \phi, \psi\} = \{t, r, \bar{\theta}, \bar{\phi}, \bar{\psi}, \theta, \phi, \psi\}, \quad \chi = \chi(r), \quad \kappa = 0.
\tag{6.2.6}
$$

Now we turn on a pure gauge B-field, $B = d\Lambda$, with

$$
\begin{aligned}
\Lambda &= H(r)\Pi_{\bar{\imath}}(\bar{\theta}, \bar{\phi}, \bar{\psi})dx^{\bar{\imath}}, \\
&= \frac{1}{2}H(r)R^2\left(\sin^2\bar{\theta}d\bar{\phi} + \cos^2\bar{\theta}d\bar{\psi}\right),
\end{aligned}
\tag{6.2.7}
$$

where $\Pi_{\bar{\imath}}(\bar{\theta}, \bar{\phi}, \bar{\psi})$ is the $\bar{S}^3$ vector spherical harmonic (VSH) of the mode $\{\bar{l}, \bar{m}_1, \bar{m}_2, \bar{s}\} = \{1, 0, 0, -1\}$[3]. It can be shown that

$$
B = \frac{1}{2}H'(r)R^2(\sin^2\bar{\theta}drd\bar{\phi} + \cos^2\bar{\theta}drd\bar{\psi}) + H(r)R^2\sin\bar{\theta}\cos\bar{\theta}(d\bar{\theta}d\bar{\phi} - d\bar{\theta}d\bar{\psi}).
\tag{6.2.8}
$$

We can see that this B-field at the boundary $r \rightarrow \infty$ is actually a field strength tensor that describes a constant magnetic field on $\bar{S}^3$ by

$$
\begin{aligned}
*B(r \rightarrow \infty) &= H(r \rightarrow \infty)R^2\sin\bar{\theta}\cos\bar{\theta}(*d\bar{\theta}d\bar{\phi} - *d\bar{\theta}d\bar{\psi}) \\
&= H(r \rightarrow \infty)R^2\left(\sin^2\bar{\theta}d\bar{\phi} + \cos^2\bar{\theta}d\bar{\psi}\right) \equiv H_{\bar{\imath}}dx^{\bar{\imath}}
\end{aligned}
\tag{6.2.9}
$$

with the magnitude of the magnetic field

$$
\| * B(r \rightarrow \infty)\| = \sqrt{H_{\bar{\imath}}H^{\bar{\imath}}} = H(r \rightarrow \infty)R^2 = const.
\tag{6.2.10}
$$

Note that for $H(r)$ to be asymtotically finite at $r \rightarrow \infty$, $H'(r \rightarrow \infty)$ has to vanish. We will later use $H_{ext} \equiv H(r \rightarrow \infty)$. With the embedding and B-field ansatz, two

---

[3]A more general ansatz with $\Lambda = H(r)\Pi(\bar{\theta}, \bar{\phi}, \bar{\psi})$, where $\Pi(\bar{\theta}, \bar{\phi}, \bar{\psi})$ is a linear combination of either VSH mode $\bar{l} = 1, \bar{s} = 1$ or mode $\bar{l} = 1, \bar{s} = -1$, also works.

non-trivial equations of motion can be obtained from (6.2.2) and (6.2.3). Equivalently, these two equations can also be obtained by first putting the ansatz into the action, and then vary the action with respect to $H(r), \chi(r)$. For reference, the substituted action is

$$
S = -T_{D7} \frac{R^3}{2} \int d^8\sigma \sin(\theta) \cos(\theta) \sin(\bar{\theta}) \cos(\bar{\theta}) \sqrt{-G_{tt}(r) \left(G_{33}(r)^2 + H(r)^2 R^4\right)}
$$
$$
\times \sqrt{\left((1 - \chi(r)^2)\left(4 G_{33}(r) G_{rr}(r) + H'(r)^2 R^4\right) + 4 G_{33}(r) R^2 \chi'(r)^2\right)} \left(1 - \chi(r)^2\right).
$$

$$(6.2.11)$$

Here are some remarks to consider:

- The embedding ansatz (6.2.5) and (6.2.6) do not work successfully when we treat $H(r) = const$.

- The B-field (6.2.8) is inspired by vector spherical harmonics. Had we used the B-field ansatz from local tetrads (e.g. $B \propto e^{(1)} \wedge e^{(2)}$, where $e^{(1)}$ and $e^{(1)}$ are two different one-form local tetrads), the equation (6.2.3) would not have been satisfied.

6.2.2 B-Field in Global Coordinates at Zero Temperature

For convenient, we will work in Fefferman-Graham coordinates [49] i.e. we will represent the radial coordinate r in (3.3.2) with $z = R/(r + \sqrt{r^2 + R^2})$. At zero temperature, the $AdS_5 \times S^5$ metric is

$$
ds^2 = -\frac{(1+z^2)^2}{4z^2} dt^2 + \frac{R^2}{4z^2}\left(1 - z^2\right)^2 \left(d\bar{\theta}^2 + \sin^2\bar{\theta} d\bar{\phi}^2 + \cos^2\bar{\theta} d\bar{\psi}^2\right)
$$
$$
+ \frac{R^2}{z^2} dz^2 + R^2 \frac{d\chi^2}{1 - \chi^2} + R^2\chi^2 d\kappa^2 + R^2(1 - \chi^2)(d\theta^2 + \sin^2\theta d\phi^2 + \cos^2\theta d\psi^2),
$$

$$(6.2.12)$$

where the AdS centre and boundary are at $z = 1$ and $z = 0$, respectively. The substituted action is then

$$
S = -T_{D7} \frac{R^7}{2} \int d^8\sigma \sin(\theta) \cos(\theta) \sin(\bar{\theta}) \cos(\bar{\theta}) \left(1 - \chi(z)^2\right)
$$
$$
\times \sqrt{\frac{(z^2 + 1)^2 \left(H(z)^2 + \frac{(1-z^2)^4}{16z^4}\right)\left((1 - \chi(z)^2)\left(H'(z)^2 + \frac{(1-z^2)^2}{z^4}\right) + \frac{(1-z^2)^2\chi'(z)^2}{z^2}\right)}{4z^2}}.
$$

$$(6.2.13)$$

To solve the equations of motion, we use shooting method (see appendix A for more detail) by shooting from IR to boundary. Different types of embeddings are distinguished by different initial conditions. There are two types of the D7-brane embedding called ball and Minkowski embeddings [18,48,50]. The ball and Minkowski embeddings correspond to the brane completely wrapping shrinking $\bar{S}^3 \subset AdS_5$ and $S^3 \subset S^5$, respectively [18,48,50]. For ball embeddings, we have the initial condition

$$\chi(z) = \chi_{ball} - \frac{3}{8}\chi_{ball}\left(H_{c2}^2 + 1\right)(1-z)^2 + \mathcal{O}\left((1-z)^3\right), \qquad (6.2.14)$$

$$H(z) = H_{c2}(1-z)^2 + H_{c2}(1-z)^3 + \mathcal{O}\left((1-z)^4\right), \qquad (6.2.15)$$

where at the AdS centre ($z = 1$) the brane can start at any angle from 0 to $\pi/2$ to cover all possible solutions (see figure 6.1 for an illustration). For Minkowski embeddings, the initial condition is

$$\chi(z) = 1 + \chi_{M1}(z_{Mink} - z) + \chi_{M2}(z_{Mink} - z)^2 + \mathcal{O}\left((z_{Mink} - z)^3\right), \qquad (6.2.16)$$

$$H(u) = H_M + H_{M1}(z_{Mink} - z) + H_{M2}(z_{Mink} - z)^2 + \mathcal{O}\left((z_{Mink} - z)^3\right), \quad (6.2.17)$$

where $\chi_{M1}, \chi_{M2}, H_{M1}, H_{M2}$ are long expressions consisting of z_{Mink} and H_M, and at $z = z_{Mink}$ the brane has to start at the vertical axis $\chi(z_{Mink}) = 1$ (see figure 6.1) to ensure that it totally wraps the shrinking $S^3 \subset S^5$. By counting parameters, we find each case has two free parameters remaining due to regularity requirement. Note in particular that $H(z) \to 0$ as $z \to 1$ to avoid B-field singularity at the centre. This regularity requirement will have an important impact on the phase transitions between confined and deconfined phases. The expansion of the fields χ and H near boundary is

$$\chi(z) = \frac{2m}{R}z + \frac{8c_1}{R^3}z^3 + \frac{4m}{R}z^3\log(2z) + \mathcal{O}(z^4), \qquad (6.2.18)$$

$$H(z) = H_{ext} + \frac{4M_{tz}}{R^2}z^2 + 8H_{ext}z^2\log(2z) + \mathcal{O}(z^3). \qquad (6.2.19)$$

Due to the presence of the log terms, we need to renormalise c_1 and M_{tz}. In the renormalisation process, having the B-field turned on causes an additional divergence term in the on-shell action. Using only the counterterms in (3.4.13) and (3.4.19) is no longer enough to cancel the divergence. Similar to [6], to completely cancel the divergence we have an additional counterterm

$$L_H = \frac{R^3}{2\pi}\log(\epsilon)H(\epsilon)^2. \qquad (6.2.20)$$

To find the renormalised values, we do the same thing as in section 3.4. The renormalised values of c_1 and M_{tz} are given by

$$c = c_1 - \frac{mR^2}{2} \log \frac{m}{R}, \quad M = M_{tz} + H_{ext}R^2, \tag{6.2.21}$$

respectively. Here m, c, H_{ext} and M will be identified with the quark mass, quark condensate, external magnetic field and magnetisation respectively.

We show some solutions by plotting the brane shapes in the figure 6.1. We show the plots at various fixed H_{ext}. We see as H_{ext} increases, more and more branes of ball embeddings vanishes. The disappearance is due to the fact that for a given initial condition of ball embeddings, there is a maximum value of H_{ext}.
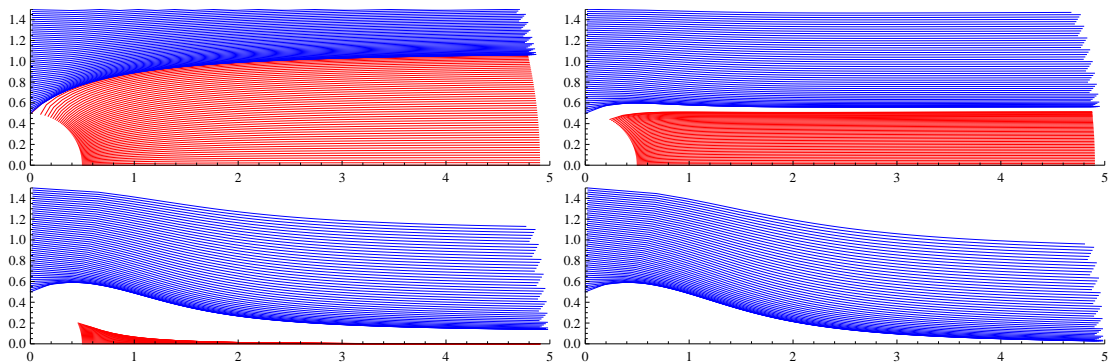
Figure 6.1: Plot of brane shapes for D7 embedding. From Left to Right and Top to Bottom shows the plot at fixed external magnetic field $H_{ext} = 0, 2, 4, 5$, respectively. Red is for ball embeddings where D7 reaches AdS centre. Blue is for Minkowski embeddings where D7 does not reach AdS centre. The horizontal and vertical axes are $R\sqrt{1-\chi^2}/(2z), R\chi/(2z)$. There is the development of mass gap as external magnetic field is increased roughly to $H_{ext} = 4$. The gap closes again around $H_{ext} = 5$ where the lowest Minkowski embedding has zero quark mass.

In figure 6.2, We plot all possible values of m and H_{ext} in ball embeddings and some for Minkowski. We see that there is a quark mass gap developed in our case while in [6], there is no mass gap. Therefore, the two cases are qualitatively different.

The mass gap is plotted in figure 6.3.
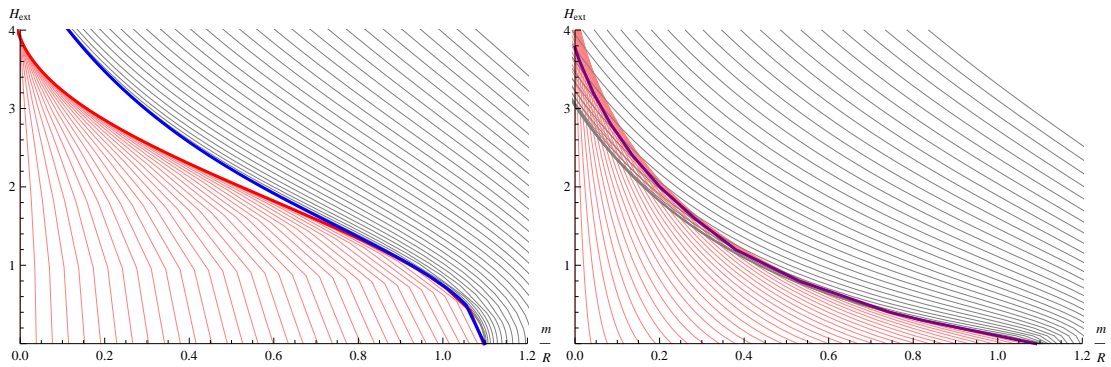
Figure 6.2: Plot of possible values of H_{ext} and m. Different lines represent different initial condition of $\chi(z)$, while different points along each line represent different initial condition of $H(z)$. Light Red represents ball embeddings while Grey represents Minkowski embeddings. Left is for the system discussed here. We draw critical curve for ball (Thick Red) and for Minkowski (Thick Blue). We define the white region between Thick Red and Thick Blue for $m/R > 0$ as the mass gap. Right is for the system discussed in [6], where they determine the exact boundary between the two configurations by the thick purple curve obtained from the comparison of free energy.

6.2.3 The Mass Gap

The presence of mass gap at finite external magnetic field is an interesting result. We would like to study this effect carefully.

B-field Perturbation

To see the development of the mass gap, it would be interesting to see the behaviour of the equations in the linear order of the B-field first. If there is no mass gap at the linear order, we will conclude mathematically that the mass gap comes from the nonlinearity of the B-field in the equation. In this case, we will continue adding higher order terms to the equations to see the mass gap development. For example,
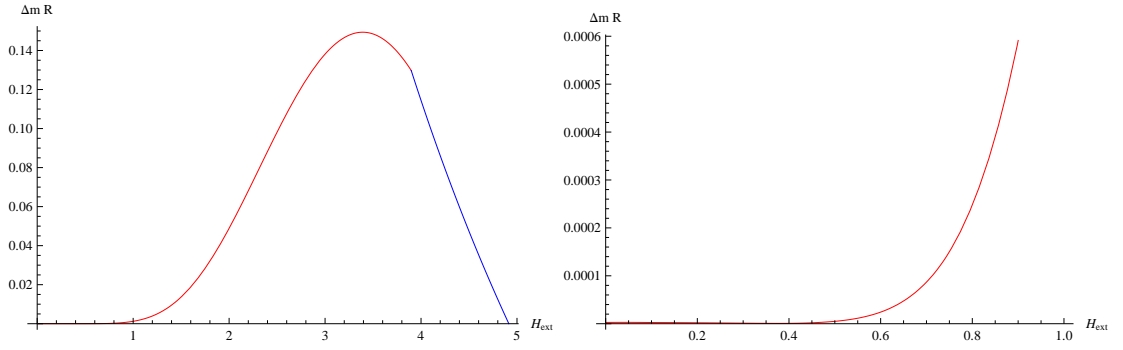
Figure 6.3: Mass gap between confined and deconfined phase for various H_{ext}. Red indicates the region that ball embeddings are possible. Blue indicates the region that all but equatorial embedding ($\chi(z) = 0$) vanishes. Left shows all the relevant plot range while Right shows the zoomed in region near plot origin. To get even closer result near plot origin, we need to collect more associated data.

the equations of motion in the first order are

$$
\begin{aligned}
\left(\left(z^2 - z^6\right) \chi(z)^2 + \left(z^4 - 1\right) z^2\right) \chi''(z) + \left(3 - 3z^4\right) \chi(z)^3 + 3\left(z^4 - 1\right) \chi(z) \\
+ 4z^2 \left(z^4 - 1\right) \chi(z)\chi'(z)^2 + \left(z\left(5z^4 + 4z^2 + 3\right) - z\left(5z^4 + 4z^2 + 3\right) \chi(z)^2\right) \chi'(z) \\
+ 4\left(z^7 + z^5 + z^3\right) \chi'(z)^3 = 0, \quad (6.2.22)
\end{aligned}
$$

$$
H''(z) + \frac{\left(3z^4 - \frac{4\left(z^6 + z^4 + z^2\right)\chi'(z)^2}{\chi(z)^2 - 1} + 1\right)}{z\left(z^4 - 1\right)} H'(z) + \frac{16\left(z^2\chi'(z)^2 - \chi(z)^2 + 1\right)}{\left(z^2 - 1\right)^2 \left(\chi(z)^2 - 1\right)} H(z) = 0. \tag{6.2.23}
$$

Then we solve the equations by shooting method. We illustrate the solutions in the figure 6.4. From the plot of first order, there is no mass gap found. This is obvious since in the first order, the equations of motion of brane shape does not contain the field $H(z)$, so for any values of mass we can set H_{ext} to an arbitrary value yielding no mass gap. However, for the higher orders, there appears to have the mass gap. The result for the third, the fifth and the seventh orders are also shown in figure 6.4.

We emphasise that the first order does not contain the mass gap feature of the full equation. We show this by considering the equatorial embedding where at the
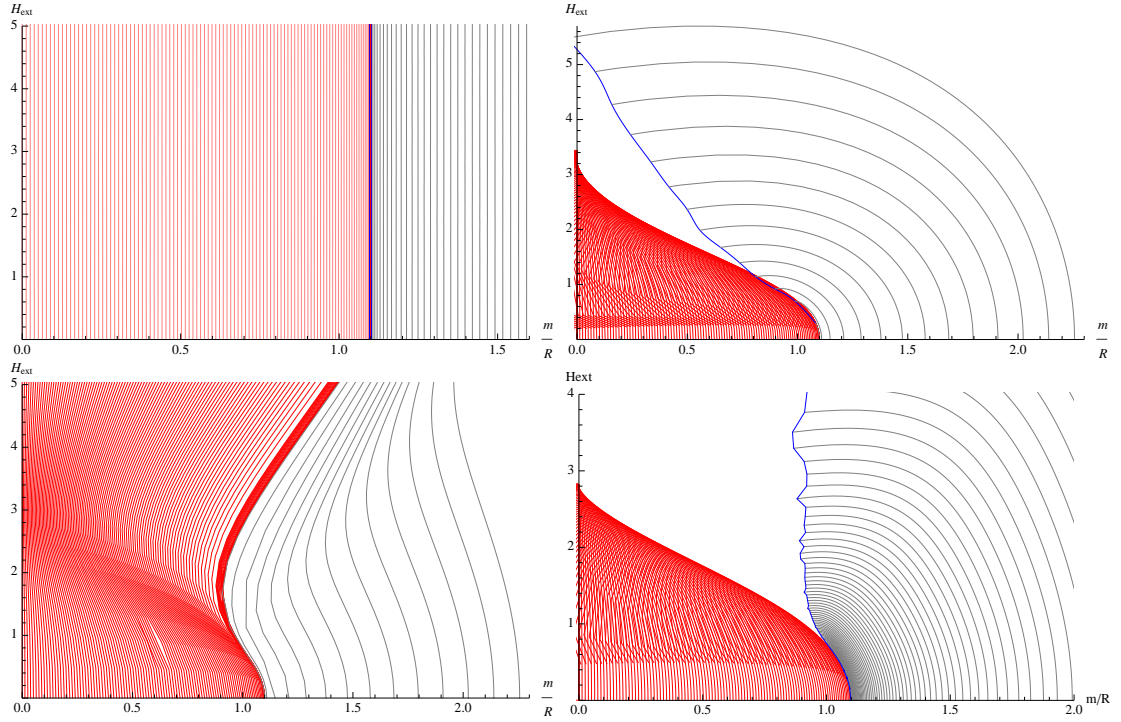
Figure 6.4: Plots of possible values of H_{ext} and m/R. Different lines represent different initial conditions of $\chi(u)$, whereas different points along each line represent different $H(u)$ initial conditions. Red lines represent ball embeddings and grey lines represent Minkowski embeddings. The blue lines represent envelopes of Minkowski embeddings beyond which there is a numerical issue preventing us to find the solution. Top Left, Top Right, Bottom Left and Bottom Right are the results from the first, third, fifth and seventh order perturbation, respectively. We should not trust the result from at and beyond the fifth order since the plot has a weird behaviour that is not a sign to converge to the solution of the full equation (i.e. the left plot in figure 6.2).

first order the EOM for H(z) now reads

$$H''(z) + \frac{\left(3z^4 + 1\right) H'(z)}{z \left(z^4 - 1\right)} - \frac{16H(z)}{\left(z^2 - 1\right)^2} = 0, \tag{6.2.24}$$

which has the analytic solution that is

$$H(z) = \frac{c_1 z^2}{\left(z^2 - 1\right)^2} + \frac{c_2 \left(-z^4 - 8z^2 \log(z) + 8z^2 \log \left(z^2 + 1\right) - 1\right)}{2 \left(z^2 - 1\right)^2}. \tag{6.2.25}$$

Requiring that the solution vanishes at AdS centre gives

$$c_1 = -c_2(\log(16) - 1). \tag{6.2.26}$$

Requiring that the solution tends to H_{ext} at the boundary gives

$$c_2 = -2H_{ext}. \tag{6.2.27}$$

Finally, we have

$$H(z) = \frac{H_{ext} \left(z^4 + 8z^2 \log \left(\frac{z}{z^2 + 1}\right) + z^2(\log(256) - 2) + 1\right)}{\left(z^2 - 1\right)^2}. \tag{6.2.28}$$

The function $H(z)$ of this form is well-behaved everywhere from the centre to the boundary. Furthermore, since H_{ext} is an overall factor, the solution valid for all H_{ext}.

We see that at the linear level, the solution is valid for every value of H_{ext}. Therefore, the linear level does not capture the mass gap feature of the full equation.

Let us now consider equatorial embedding with $H(z)$ up to third order. The EOM is given by

$$H''(z) - \frac{16z^4 H(z) H'(z)^2}{\left(z^2 - 1\right)^4} + \frac{\left(3z^4 + 2z^2 + 3\right) z^3 H'(z)^3}{\left(z^2 - 1\right)^3 \left(z^2 + 1\right)}$$
$$+ \left(-\frac{32 \left(z^5 + z^3\right) H(z)^2}{\left(z^2 - 1\right)^5} - \frac{3z^4 + 1}{z - z^5}\right) H'(z) - \frac{16H(z)}{\left(z^2 - 1\right)^2} + \frac{256z^4 H(z)^3}{\left(z^2 - 1\right)^6} = 0. \tag{6.2.29}$$

We cannot obtain an analytic solution. Let us try to argue the limitations of H_{ext} as follows. We start from adding a function to the analytic result of the previous order:

$$H(z) = H_0 \left(1 + 8\frac{z^2}{\left(z^2 - 1\right)^2} \log \left(\frac{2z}{z^2 + 1}\right)\right) + \frac{1}{4}c(z - 1)^2 - \frac{1}{4}c(z - 1)^3$$
$$+ \frac{1}{384}(z - 1)^4 \left(-c^3 - 6c^2 H_0 - 12cH_0^2 + 56c - 8H_0^3\right) + \mathcal{O}((z - 1)^5). \tag{6.2.30}$$

We obtain $c = H_{c2} - 2H_0$. We take

$$H(0) = \frac{1}{384}\left(-H_{c2}^3 + 248H_{c2} - 112H_0\right) + \mathcal{O}((0-1)^5) = H_{ext}, \tag{6.2.31}$$

$$H'(0) = \frac{1}{96}\left(H_{c2}^3 - 176H_{c2} + 352H_0\right) + \mathcal{O}((0-1)^4) = 0, \tag{6.2.32}$$

where in the last equalities of the two above equations, we used the expansion at boundary

$$H(z) = H_{ext} + z^2\left(4M_{tz}R^2 + 8H_{ext}\log(2z)\right) + \mathcal{O}(z^3). \tag{6.2.33}$$

Let us formally ignore $\mathcal{O}((0-1)^4), \mathcal{O}((0-1)^5)$ (abbreviated $\mathcal{O}_4, \mathcal{O}_5$ respectively) by assuming they do not depend on H_{ext}, H_{c2}, H_0. We then eliminate H_0 and obtain

$$H_{ext} = \frac{-5H_{c2}^3 + 1408H_{c2} + 224\mathcal{O}_4 + 2816\mathcal{O}_5}{2816}. \tag{6.2.34}$$

Using the fact that $H_{ext} = 0$ when $H_{c2} = 0$, we finally obtain

$$H_{ext} = \frac{H_{c2}}{2} - \frac{5}{2816}H_{c2}^3. \tag{6.2.35}$$

The result is plotted in blue in figure 6.5. We see that there is a maximal value of H_{ext}. We believe that our discussion is valid up to $H_{c2} \sim 10$ as the comparison with numeric suggests (red plot in figure 6.5).

We see that there is indeed the maximal value of H_{ext} for which the equatorial embedding is allowed. However, we are still unable to capture the mass gap feature of the full equation where the maximal value of H_{ext} is approximately 5.58. This value is approached for asymptotically large H_{c2}, the value that is beyond the domain of validity of the third order perturbation.

Our semi-analytical treatment here is not fully justified. There is no reason to take $\mathcal{O}_4, \mathcal{O}_5$ to be independent of H_{ext}, H_{c2}, H_0. Therefore, the matching with numerical result up to $H_{c2} \approx 10$ can as well be from pure coincidence. Nevertheless, the form of the RHS of the equation (6.2.35) is as expected. Since we expand the equation up to third order in $H(z)$, we should obtain H_{ext} as a third order polynomial of H_{c2}. To obtain the more precise relationship between H_{ext} and H_{c2}, we will have to study higher order perturbations. For general embedding, the mass gaps of the third and the seventh orders may be arisen from a numerical issue. We cannot have solutions for H_{c2} and H_M higher than some values. We first assume this is the true
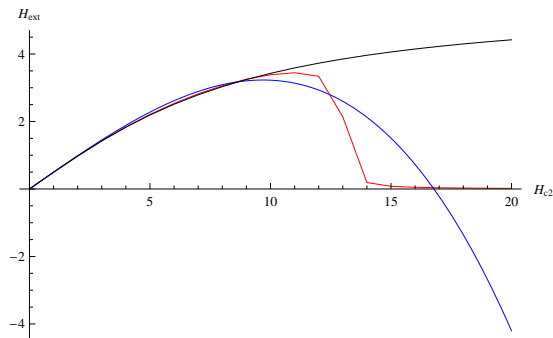
Figure 6.5: The plot of H_{ext} versus H_{c2} for equatorial embedding with perturbative order 3 in B-field. Red is the result from purely numerical, Blue is the result from semi-analytical. We also compare with the Black plot obtained from the full equation in H_{ext}.

feature. The nature of the mass gap here is then different from the one in non-perturbative case which has solutions for all values of H_{c2} and H_M. We cannot yet proved the assumption. So far, even though we have adjusted the WorkingPrecision and have increased the number of terms in the series expansions of initial condition, we still cannot go beyond such H_{c2} and H_M values.

One thing we have from the perturbative analysis is that no matter how high the order of the expansion of $H(u)$ and its derivatives is, we always have the constraint $H(u) = 0$ at the centre. This naturally comes from the EOMs without imposing it by hand.

Metric Perturbation

Another way to see the development of the mass gap is to do the metric expansion around the flat geometry. We first expand the metric near AdS centre. We then pretend that this expansion works throughout the spacetime. This prescription is coordinate dependent, so we will work in both u- and z-coordinates. However, we expect the qualitative result to be the same.

For u-coordinates, we start by obtaining the u-coordinates from (6.2.4). Focusing

on the AdS part, the full metric is

$$ds^2 = -\frac{u^2}{R^2}\left(1 + \frac{R^2}{4u^2}\right)^2 dt^2 + u^2\left(1 - \frac{R^2}{4u^2}\right)^2 (d\bar\theta^2 + \sin^2\bar\theta d\bar\phi^2 + \cos^2\bar\theta d\bar\psi^2) + \frac{R^2}{u^2} du^2.$$

(6.2.36)

Near AdS centre, we make an expansion

$$\delta u = u - \frac{R}{2}.$$

(6.2.37)

We now expand the metric to nth order in u and use the metric as if this approximation extends to the boundary. As a reference, the zeroth order is given by

$$ds^2 = -dt^2 + 4\left(u - \frac{R}{2}\right)^2 (d\bar\theta^2 + \sin^2\bar\theta d\bar\phi^2 + \cos^2\bar\theta d\bar\psi^2) + 4du^2.$$

(6.2.38)

Let us concentrate on the zeroth order for a moment. The EOM is given by

$$H''(u) + R\frac{(2u/R - 1)H'(u)^3}{4\left(H(u)^2 + (1 - 2u/R)^4\right)} - \frac{H(u)H'(u)^2}{H(u)^2 + (1 - 2u/R)^4}$$
$$+ \frac{\left(2(1 - 2u/R)^4 - 2H(u)^2\right)H'(u)}{(2u - R)H(u)^2 + R(2u/R - 1)^5} - \frac{16(1 - 2u/R)^2 H(u)}{R^2(H(u)^2 + (1 - 2u/R)^4)} = 0.$$

(6.2.39)

An analytic result can be obtained from Mathematica

$$H_\mp(c_1, c_2)(u) =$$

$$\frac{-4i\sqrt{c_1 - 1}(\frac{u}{R} - 1)\frac{u}{R} \mp \frac{(1-i)\sqrt{-i(c_1+1)\left(\sqrt{c_1^2-1}-c_1\right)\left(c_1(c_2-1)+c_2+16(\frac{u}{R}-1)\frac{u}{R}(2(\frac{u}{R}-1)u+1)+1\right)}}{-c_1+\sqrt{c_1^2-1}-1}}{\sqrt{c_1 + 1}}$$
$$- i\frac{\sqrt{c_1 - 1}}{\sqrt{c_1 + 1}}.$$

(6.2.40)

Requiring $H_\mp(c_1, c_2)(R/2) = 0$ gives $c_2 = 1$ and hence

$$H_\mp(c_1, 1)(u) =$$

$$-\frac{i\sqrt{c_1 + 1}\left(c_1 - \sqrt{c_1^2 - 1} + 1\right)(1 - 2\frac{u}{R})^2}{-\sqrt{c_1 + 1}(c_1 - 1) + c_1\sqrt{c_1 - 1} + \sqrt{c_1 - 1} \mp 2\sqrt{(c_1 + 1)\left(-c_1 + \sqrt{c_1^2 - 1}\right)}}.$$

(6.2.41)

Choosing appropriate c_1, we have the solution

$$H(u) = \frac{H_{c2}}{R^2}\left(u - \frac{R}{2}\right)^2.$$

(6.2.42)

The limit $u \to \infty$ then implies $H_{ext} \to \infty$. Note that we do not need to see what the domain of validity (based on its dependence on c_1) of H_{c2} is. This is because whatever the valid value of H_{c2} is, we always have $H_{ext} \to \infty$.

Thus, we conclude that the limit $u \to \infty$ for non-trivial solution of $H(u)$ is infinity. This is not a feature we encountered in the full case.

We then plot, for massless embedding, the solution $H(u)$ of perturbed EOM subject to regularity requirement. For some reason, the odd order perturbations fail to give the result. So we only report even order results.

The result $H(u \to \infty)$, diverges. For higher order, the divergence behaviour keeps getting better as order increases. However, up to 300th order, the result still does not converge to the result for full metric. Therefore, the perturbation in u-coordinates is not useful. Figure 6.6 compare the results between full metric and perturbation at 300th order.

The failure of u-coordinates is understandable because radius of convergence of the series expansions is $\sim R$ but we extend our calculation up to boundary which has large value of u. Let us use another coordinates which the distance between centre and boundary does not exceed the radius of convergence.
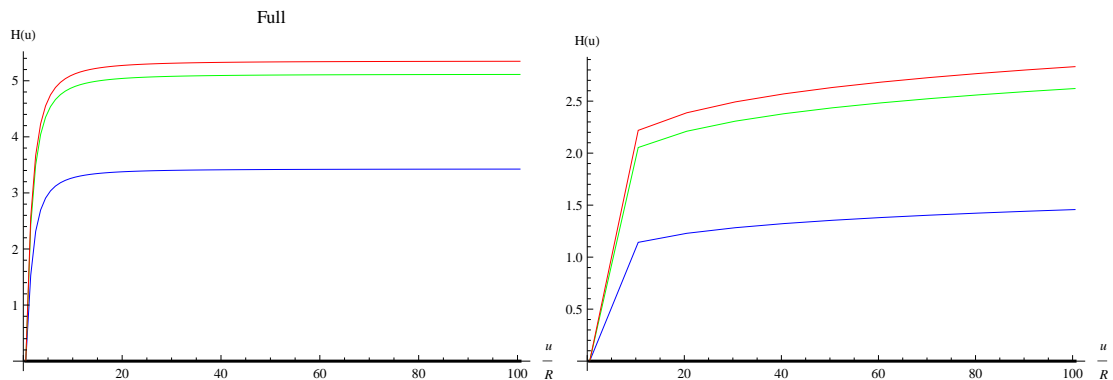
Figure 6.6: The plot of $H(u)$ for various values of H_{c2}. Black, Blue, Green, Red stand for $H_{c2} = 0, 10, 50, 100$, respectively. Left is the result from the full metric. Right is the result from the perturbed metric at the 300th order.

For z-coordinates we use the metric (in AdS_5 part)

$$ds^2 = -\frac{(1+z^2)^2}{4z^2}dt^2 + \frac{R^2(1-z^2)^2}{4z^2}\left(d\bar{\theta}^2 + \sin^2\bar{\theta}d\bar{\phi}^2 + \cos^2\bar{\theta}d\bar{\psi}^2\right) + \frac{R^2}{z^2}dz^2. \quad (6.2.43)$$

As in u-coordinates, we expand near the AdS centre in

$$\delta z = 1 - z. \tag{6.2.44}$$

As a reference, the zeroth order expansion of the metric is given by

$$ds^2 = -dt^2 + R^2(1-z)^2 \left(d\bar{\theta}^2 + \sin^2 \bar{\theta} d\bar{\phi}^2 + \cos^2 \bar{\theta} d\bar{\psi}^2\right) + R^2 dz^2. \tag{6.2.45}$$

Let us concentrate on the zeroth order for a moment. The EOM is given by

$$H''(z) + \frac{(z-1)H'(z)^3}{2\left(H(z)^2 + (z-1)^4\right)} - \frac{H(z)H'(z)^2}{H(z)^2 + (z-1)^4} - \frac{\left(H(z)^2 - (z-1)^4\right)H'(z)}{(z-1)\left(H(z)^2 + (z-1)^4\right)}$$
$$- \frac{4(z-1)^2 H(z)}{H(z)^2 + (z-1)^4} = 0. \tag{6.2.46}$$

An analytic result can be obtained from Mathematica

$$H_\pm(c_1, c_2)(z) = -\frac{\left(\sqrt{1-c_1^2} \pm \sqrt{1-c_1 c_2}\right)(z-1)^2}{c_1}. \tag{6.2.47}$$

Recall that the centre is at $z = 1$ while the boundary is at $z = 0$. Requiring $H_\pm(c_1, c_2)(0) = H_{ext}$ gives

$$H(z) = H_{ext}(z-1)^2. \tag{6.2.48}$$

Let us consider the domain of validity for H_{ext} from

$$H_{ext} = -\frac{\left(\sqrt{1-c_1^2} \pm \sqrt{1-c_1 c_2}\right)}{c_1}. \tag{6.2.49}$$

We consider a special case on positive solution with $c_2 = c_1$. Then

$$H_{ext} = -2\frac{\sqrt{1-c_1^2}}{c_1}. \tag{6.2.50}$$

Redefine $c_1 = \cos y$, then

$$H_{ext} = -2\tan y. \tag{6.2.51}$$

Since $\tan y$ can take any real values, we conclude that H_{ext} can take any real values.

Therefore, the solution is valid for all H_{ext}. As in u-coordinate, this feature is not realised in the full case.

At each order, we solve for $H(z)$. Unfortunately, the analytic result can only be obtained at the zeroth level. The function $H(z)$ at second order differed a lot from

its first order counterpart. See bottom plots of figure 6.7. So unfortunately, we cannot get analytically perturbative result (i.e. it is not possible to write $H_{2nd}(z) = H_{1st}(z) + \dot{H}(z)$ as $\dot{H}(z)$ is this case is very large).

We show the results in figure 6.7, 6.8. From figure 6.7 the curves for $H_{c2} = 50, 100$ are close together despite their value being very differed. This indicates that the result is reaching the fixed point. There is a maximal value of H_{ext} that we can get even at the second order perturbation. This is indeed the case as the figure 6.8 shows the saturation of H_{ext} even at the second order.
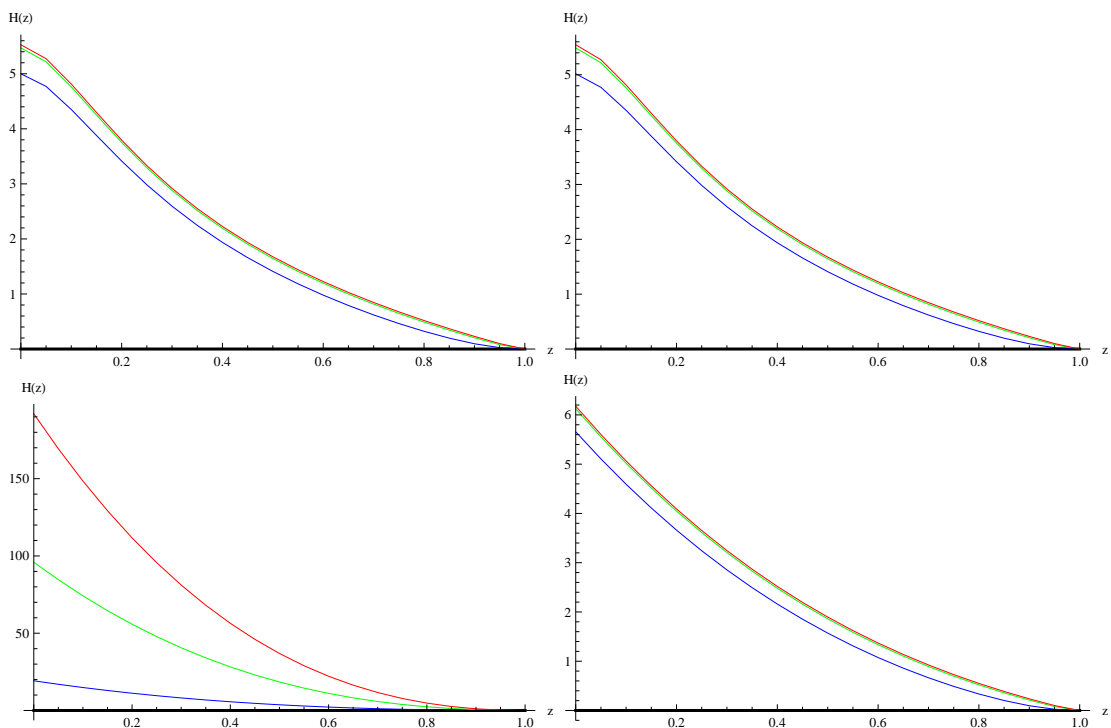
Figure 6.7: The plot of $H(z)$ for various values of H_{c2}. Black, Blue, Green, Red stand for $H_{c2} = 0, 10, 50, 100$, respectively. Top Left is the result from the full metric. Top Right is the result from the perturbed metric at the 200th order. Bottom Left is for 1st order. Bottom Right is for 2nd order.

6.2.4   Saturation of External B-field

The saturation of the B-field is the crucial part for the existence of the mass gap. In this subsection, we present the plot H_{c2} versus H_{ext} to show that no matter how
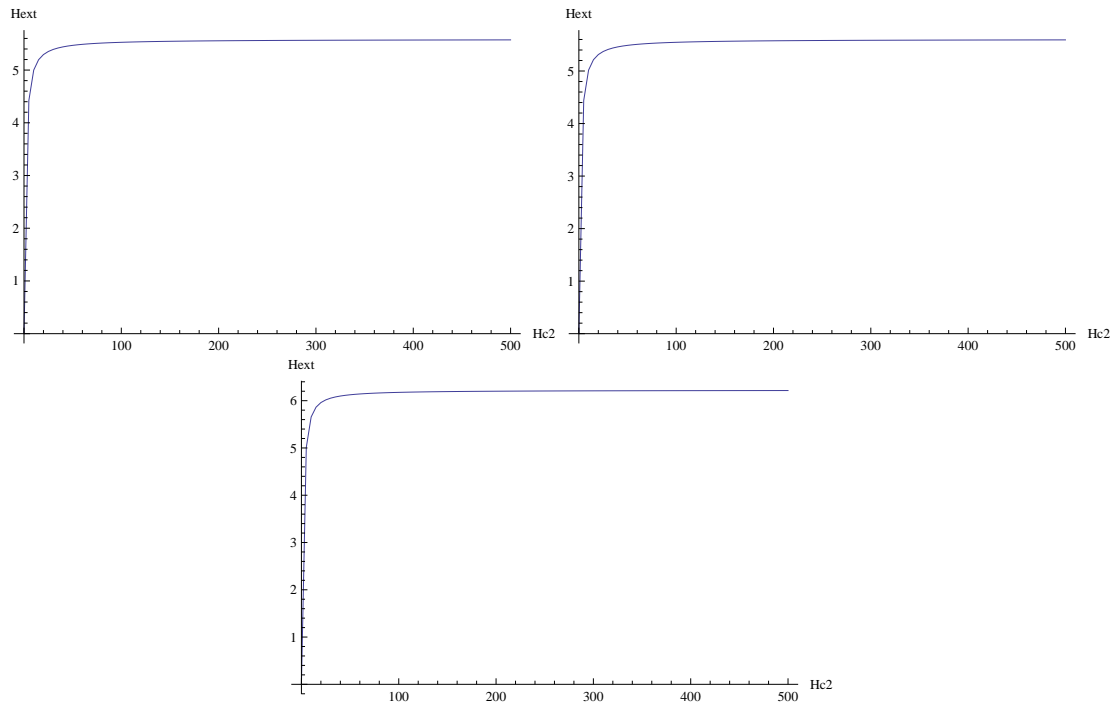
Figure 6.8: The plot of H_{ext} versus H_{c2}. Top Left is the result from the full metric. Top Right is the result from the perturbed metric at the 200th order. Bottom is for 2nd order.

high H_{c2} is, the value of H_{ext} cannot exceed a certain value[4].

We first present the results obtained from setting $u_{ball}/R = 5001/10000$, $u_{inf}/R = 10000$, where u_{ball} and u_{inf} are numerical values for AdS centre and AdS boundary, respectively. With this setting, the left of the figure 6.9 suggests that if we make H_{c2} high enough, then we can have high enough H_{ext}.

It turns out that the above feature is due to the numerical not being precise enough. In order to make it more precise, we set $u_{ball}/R = 500001/1000000$. The result is shown in the right of the figure 6.9. Numerically, we see that H_{ext} asymp-

---

[4]For ball embeddings except equatorial one, we call this value the critical magnetic field $H_{ext,crit}$, and of course this value depends on m/R (see the left plot of figure 6.2 for an illustration). If we say $H_{ext,crit}$ without any information of m/R, we mean $H_{ext,crit}$ when $m/R \to 0$ i.e. the value 3.98. For the equatorial embedding, however, the embedding can survive for $H_{ext} > H_{ext,crit}$ until H_{ext} reaches 5.58. To avoid confusion, we will refer to this value as the saturated magnetic field $H_{ext,sat}$.

totically reaching $H_{ext,sat}$ while M_{tz}/R^2 asymptotically reaching 0.38.
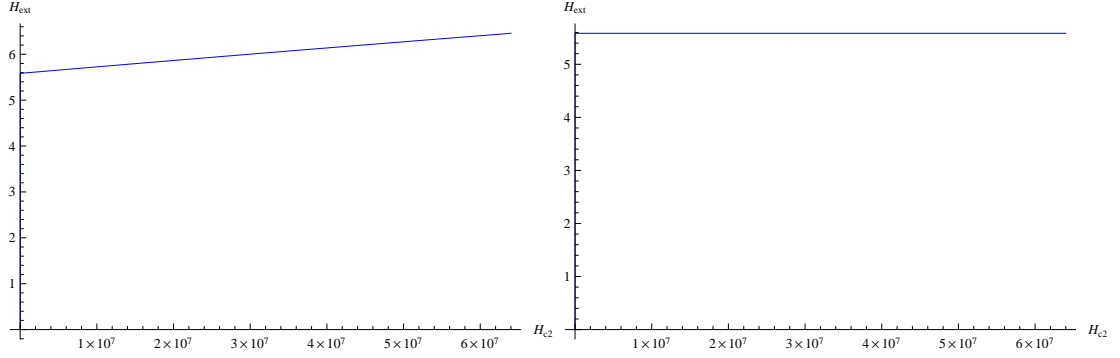
Figure 6.9: The plot of H_{ext} versus H_{c2}. Left uses the setting $u_{ball}/R = 5001/10000$. Right uses the setting $u_{ball}/R = 500001/1000000$.

6.2.5   Full B-field EOM Analysis

We want to see if there is some analytic aspect to show the gap feature. We now analyse the full EOM of $H(z)$ with the equatorial embedding $\chi(z) = 0$. Using the full EOM to determine the coefficients, we expand the field $H(z)$ near centre $(z = 1)$ and boundary $(z = 0)$ as

$$
H(z)\Big|_{z \to 1} = H_0 \left(1 + \frac{8z^2 \log\left(\frac{2z}{z^2+1}\right)}{(1-z^2)^2} \right) + \frac{c}{4}(1-z)^2 + \frac{c}{4}(1-z)^3
$$
$$
+ \frac{-c^3 - 6c^2 H_0 + c\left(56 - 12H_0^2\right) - 8H_0^3}{384}(1-z)^4 + \cdots + (\cdots)(1-z)^8,
$$

$$(6.2.52)$$

$$
H(z)\Big|_{z \to 0} = H_0 \left(1 + \frac{8z^2 \log\left(\frac{2z}{z^2+1}\right)}{(1-z^2)^2} \right) + a + bz^2 + 8az^2 \log(z) - 2(4a-b)z^4 + \cdots + (\cdots)z^6 \log(z),
$$

$$(6.2.53)$$

where H_0, c, a and b are related to H_{c2}, H_{ext} and M_{tz}. The first term of the expansions is the analytic solution of the linear perturbation. The orders of the two expansions can be arbitrary and are not directly related to each other, but the higher the orders the more accurate the result. Previously, we know that these expansions have radius of convergence not less than 1. So, using $z = 1/2$ as the meeting point, the two expansions of $H(z)$ are approximately equated. The first and second derivatives of

them are approximately equated at that point as well. After substituting and eliminating the unwanted parameters, we then have a polynomial equation containing only H_{ext} and H_{c2} as

$$25H_{c2}^7 \left(1311465 - 49672H_{ext}^2\right) + 28H_{c2}^5 \left(19611320H_{ext}^2 - 504255471\right)$$

$$+96H_{c2}^3 \left(11139559023 - 475946168H_{ext}^2\right) + 37748736H_{c2} \left(237464H_{ext}^2 - 4951755\right)$$

$$-75497472H_{ext} \left(3520H_{ext}^4 + 277624H_{ext}^2 - 4951755\right) = 0,$$

$$(6.2.54)$$

of which the degrees in H_{c2} and H_{ext} depend on the orders of the expansions of $H(z)$ near centre and boundary respectively. The contour plot of this equation is shown in figure 6.10.
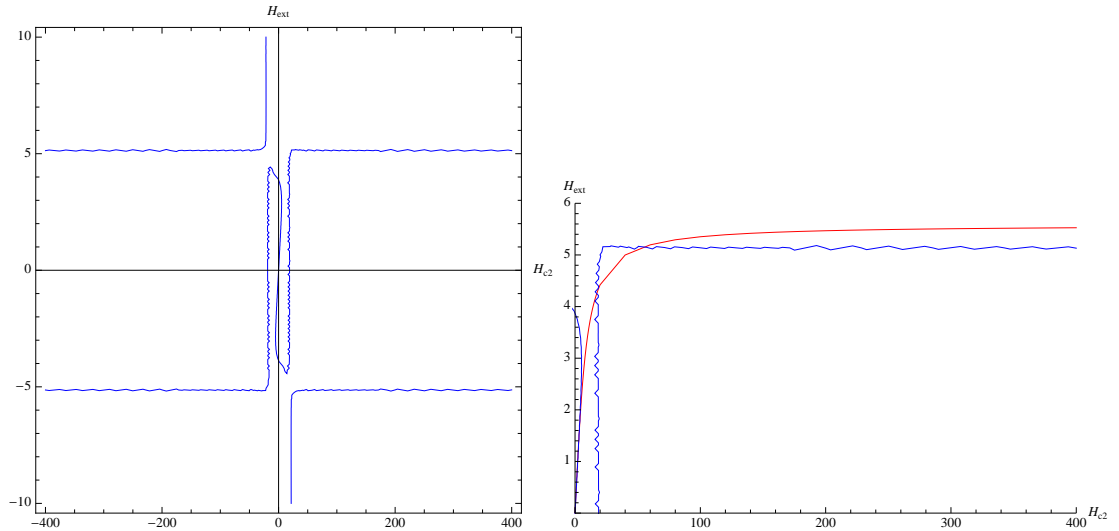
Figure 6.10: Left is the contour plot of the solution to (6.2.54). Right is a plot from the left with the result from the full numerical solution plotted in red.

From the plot, there are more than one solutions disconnected. We expect they are independent. For some physical reasons, the point $(H_{c2}, H_{ext}) = (0, 0)$ has to be included in the solution. We then choose the middle one in the plot as the physical solution. Despite the weird behaviour near $(0, 0)$, the solution shows the gap feature that there is a limit value for H_{ext} when H_{c2} goes to high values. This also qualitatively agrees with the result from numeric shown in the right side of figure 6.10. So, this is a non-numerical aspect that shows the gap feature.

Although our analysis is done perturbatively, this does not necessarily mean that only small value of H_{c2} can be trusted. In fact our analysis includes the following non-linear considerations

- We do not expand the part

$$H_0 \left(1 + \frac{8z^2 \log \left(\frac{2z}{z^2+1} \right)}{\left(1 - z^2 \right)^2} \right) \tag{6.2.55}$$

  as we expect non-linear behaviour is already present in the linear EOM (6.2.24). Had we expand such term, the asymptotic value of H_{ext} would not have been close to the actual numeric value.

- We make boundary expansion up to the term that gives non-linear relationship between H_{ext} and H_{c2}. Expanding fewer term does not capture the non-linearity and hence the result would only be valid for small value of H_{c2}. On the other hand, we expect that expanding more terms would lead to complications and that no further insights can be gained.

It turns out that our analysis capture the behaviour at small H_{c2} as well as at large H_{c2}. For the mid-values of H_{c2}, more analysis would be required. However, we expect that the graph of H_{ext} versus H_{c2} would be monotonically increasing. Therefore, there is a maximal value of H_{ext}. Indeed, we can extract the maximal value by considering the limit $H_{c2} \to \infty$ of equation (6.2.54) where the equation reduces to

$$25 H_{c2}^7 \left(1311465 - 49672 H_{ext}^2 \right) = 0 \tag{6.2.56}$$

and hence $H_{ext,max} = 5.14$ (NB the numerical result gives $H_{ext,max} \equiv H_{ext,sat} = 5.58$.). The equatorial embedding cannot exists for $H_{ext} > H_{ext,sat}$ and hence the disappearance.

6.2.6 Compare Free Energy of B-field Embedding

We compare free energy between our B-field ansatz and [6]'s. The free energy is computed by using the renormalisation as we have mentioned in chapter 3. Additionally, we have to include cut-off from B-field as well. As a check, the scaled free

energy of massless, zero B-field configuration is $F = 3/32$ in agreement with [48]. We proceed to compute the free energy between our and [6]'s configurations. The plots of free energy are shown in figure 6.11.
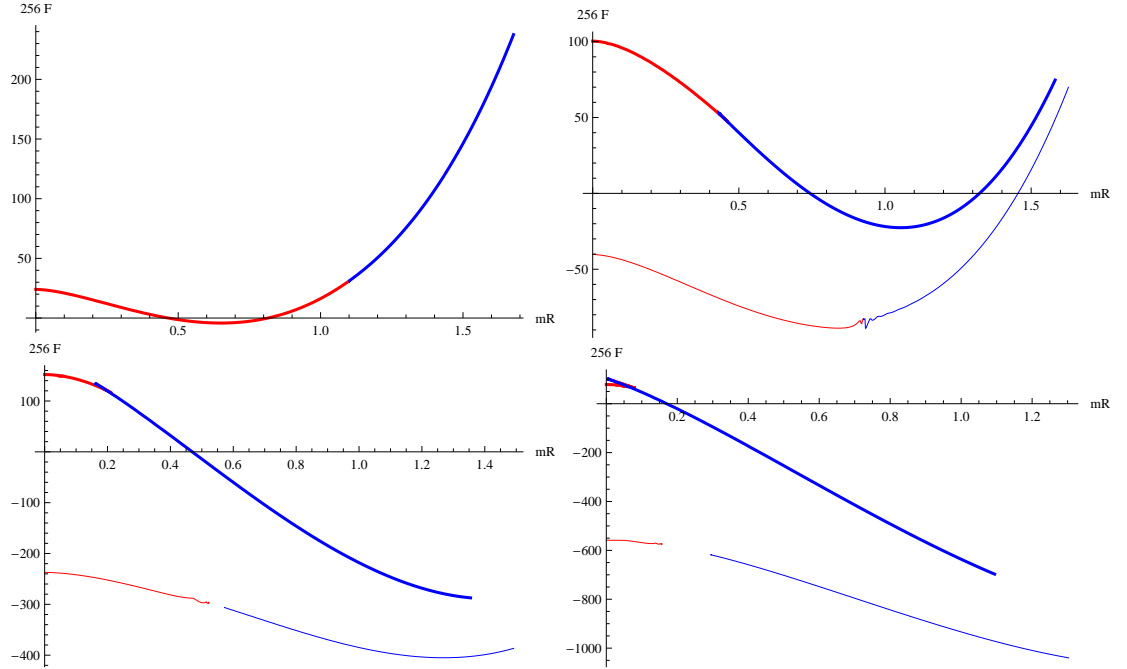
Figure 6.11: Comparison of free energy between Filev's and our system versus different quark mass. From Left to Right and Top to Bottom shows the free energy at fixed external magnetic field $H_{ext} = 0, 1, 2, 3$, respectively. Red is for ball embeddings, while Blue is for Minkowski embeddings. Thick curves are for Filev's while Thin curves are for our results. The free energy of Filev's is indeed higher. The discontinuity in our curve is due to mass gap from requiring regularity of B-field at AdS centre (discussed in previous file).

6.3 Magnetic B-field and Meson Spectra

We will analyse the effects of the magnetic B-field to the meson spectra. We make fluctuations around the background fields of section 6.2.2. For this, in addition to

DBI action, we need WZ action:

$$S_{WZ} = \frac{1}{2}T_{D7}(2\pi\alpha')^2 \int P[C_4] \wedge F \wedge F + \frac{1}{2}T_{D7} \int P[C_4] \wedge P[B] \wedge P[B]$$
$$+ 2\pi\alpha' T_{D7} \int P[C_4] \wedge P[B] \wedge F, \quad (6.3.57)$$

where C_4 is a 4-form gauge field with self-dual field strength F_5 given by

$$F_5 = \frac{4}{R}\left(\text{Vol}(AdS_5) + \text{Vol}(S^5)\right). \quad (6.3.58)$$

The equations of motion from DBI+WZ action are given by

$$\partial_a(\sqrt{-\mathcal{E}}(\mathcal{E}^{ab} - \mathcal{E}^{ba})) = -\frac{1}{5!}F_{a_1a_2a_3a_4a_5}\mathcal{F}_{a_6a_7}\tilde{\epsilon}^{a_1\cdots a_7 b} \quad (6.3.59)$$

$$-\frac{1}{4\cdot 4!}\tilde{\epsilon}^{a_1\cdots a_8}F_{\rho a_1 a_2 a_3 a_4}\mathcal{F}_{a_5 a_6}\mathcal{F}_{a_7 a_8} = \partial_b\left(\sqrt{-\mathcal{E}}(\mathcal{E}^{ba} + \mathcal{E}^{ab})\right)G_{\nu\rho}\partial_a x^\nu$$
$$+ 2\sqrt{-\mathcal{E}}\mathcal{E}^{ba}\left(G_{\nu\rho}\partial_b\partial_a x^\nu + \frac{1}{2}\left(\partial_\mu G_{\rho\nu} - \partial_\rho G_{\mu\nu} + \partial_\nu G_{\mu\lambda}\right)\partial_a x^\mu \partial_b x^\nu\right),$$
$$(6.3.60)$$

where $\mathcal{F} = P[B] + 2\pi\alpha'F$. The Greek indices are spacetime indices while Roman indices are worldvolume indices. For the spacetime fields having worldvolume indices, it is understood that the fields are pulled back to the worldvolume.

6.3.1 Charged Scalar Fluctuation

Around the background fields, we make $SO(4)$ charged scalar fluctuation. We consider an ansatz with embedding as before:

$$\chi = \chi(u), \quad \kappa = 0. \quad (6.3.61)$$

Remember that our spacetime background also includes

$$B = \frac{1}{2}H'(u)R^2(\sin^2\bar\theta dud\bar\phi + \cos^2\bar\theta dud\bar\psi) + H(u)R^2\sin\bar\theta\cos\bar\theta(d\bar\theta d\bar\phi - d\bar\theta d\bar\psi). \quad (6.3.62)$$

Additionally, we turn on charged scalar fluctuation:

$$A = A(t,u)(\sin^2\theta d\phi + \cos^2\theta d\psi). \quad (6.3.63)$$

We substitute the ansatz into the EOM (6.3.59)-(6.3.60) and expand in order of α'/R^2. The zeroth order is the background EOM while the first order consistently

gives EOM of charged scalar fluctuation. We can impose further ansatz on the charged scalar fluctuation: $A(t,u) = \exp(-i\omega t)A_c(u)$.

The next step is to find the spectrum ω. We solve the EOM of fluctuation fields with conditions from the background EOM. The shooting method is used in order to obtain the values of ω that match with the boundary expansion. The results are shown in figure 6.12 and 6.13. From our results, there are no modes that become unstable. We would like to see now if other fluctuation modes give any instability.
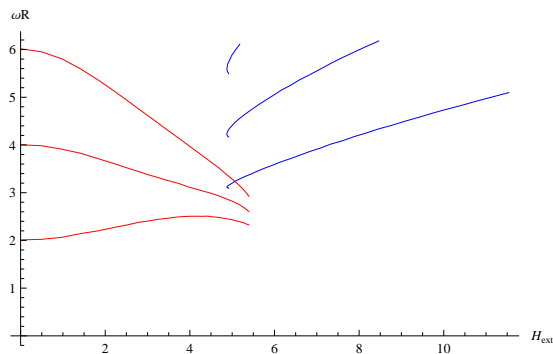
Figure 6.12: The first three normal modes of charged scalar fluctuation for fixed $mR = 0$ but vary external magnetic field. Red shows the plot for ball embedding while Blue shows the plot for Minkowski embedding.

6.3.2 Vector Fluctuation

For vector fluctuation, it is expected to couple to scalar fluctuation. So we also restrict ourselves to equatorial embedding where there is no couple with scalar fluctuation.

Recall that the embedding is given by

$$\chi = 0, \quad \kappa = 0. \tag{6.3.64}$$

Our spacetime background also includes the B-field in (6.3.62). The vector fluctuation ansatz is

$$A = A(t,u)(\sin^2 \bar{\theta} d\bar{\phi} + \cos^2 \bar{\theta} d\bar{\psi}). \tag{6.3.65}$$

Like what we did in the last subsection, we substitute the ansatz into the EOM (6.3.59)-(6.3.60) and expand in order of α'/R^2. The first order is the EOM of vector
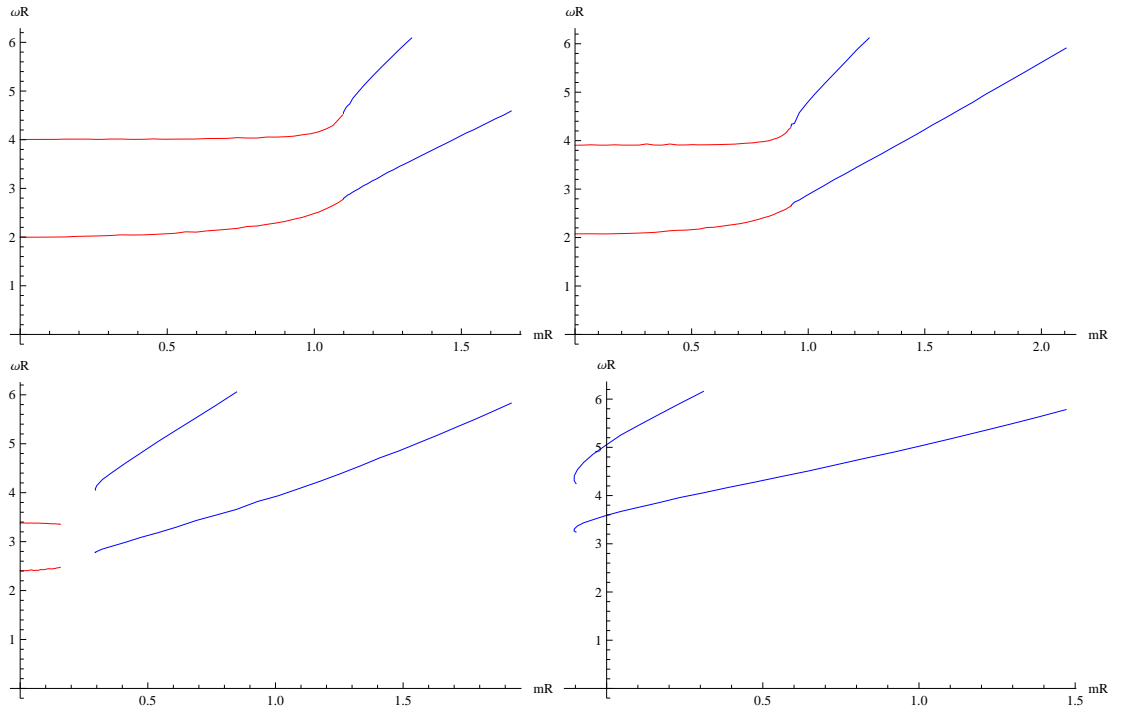
Figure 6.13: The first two normal modes of charged scalar fluctuation for fixed external magnetic field but vary quark mass. From left to right and top to bottom: $H_{ext} = 0, 1, 3, 6$, respectively. Red shows the plot for ball embedding while Blue shows the plot for Minkowski embedding.

fluctuation. We present the result of the normal modes of vector fluctuation in figure 6.14. In the same figure, we also present the result for charged scalar fluctuation. For $H_{ext} = 0$, there are some degeneracies of normal modes between modes of charged scalar and vector fluctuations. But for $H_{ext} > 0$, these degeneracies are destroyed.

6.3.3   Scalar Fluctuation

We now consider scalar fluctuation. It is expected that scalar fluctuation couples to vector fluctuation, so the computation is more involved.

However, it is much more simplified if we restrict ourselves to equatorial embedding. In this case, the scalar fluctuation does not couple to vector.
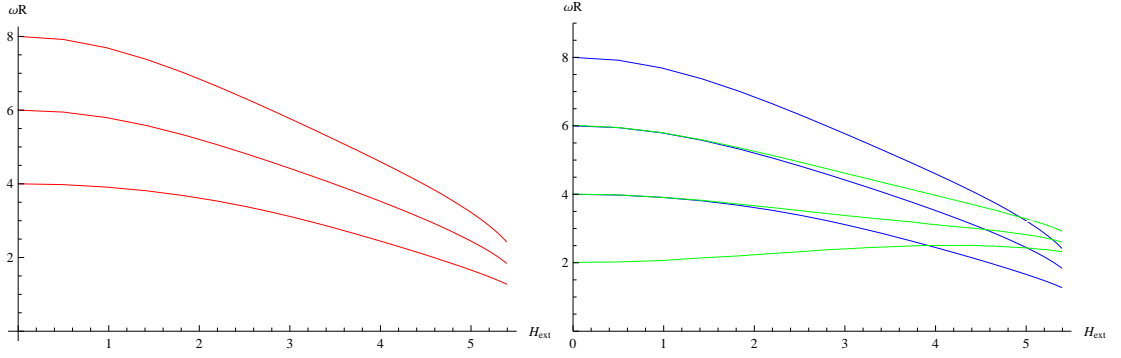
Figure 6.14: Left shows the first three normal modes of vector fluctuation for equatorial embedding $mR = 0$ but vary external magnetic field. Right shows the left figure and figure 6.12 (only data from the ball embedding) plotted together. It is interesting to see that external magnetic field destroys degeneracy of normal modes.

We use the configuration

$$\chi = 0, \quad \kappa = 0,$$
$$B = \frac{1}{2}H'(u)R^2(\sin^2\bar{\theta}dud\bar{\phi} + \cos^2\bar{\theta}dud\bar{\psi}) + H(u)R^2\sin\bar{\theta}\cos\bar{\theta}(d\bar{\theta}d\bar{\phi} - d\bar{\theta}d\bar{\psi}),$$
$$A = 0,$$

$$(6.3.66)$$

and for the fluctuation

$$x^\mu \to x^\mu + (2\pi\alpha')\Psi^\mu, \tag{6.3.67}$$

where x^μ are the spacetime coordinates normal to the D7-brane and Ψ^μ are the fluctuation fields. For the D7-brane in ten-dimensional spacetime, there are two directions perpendicular to it; let's say x^8 and x^9. Fortunately, for the equatorial embedding it turns out that the EOMs for the fluctuation fields Ψ^8 and Ψ^9 are symmetric, and we believe that setting one of the fluctuation fields to zero will give the lowest energy configuration. Therefore, we choose

$$\Psi^8 = \Psi, \quad \Psi^9 = 0. \tag{6.3.68}$$

The EOM of the fluctuation field is

$$\partial_u^2\Psi(u) + \frac{\partial_u\left(\sqrt{-e}\left(e^{-1}\right)^{uu}\right)}{\sqrt{-e}\left(e^{-1}\right)^{uu}}\partial_u\Psi(u) + \frac{1}{\left(e^{-1}\right)^{uu}}\left(\frac{3}{R^2} - \left(e^{-1}\right)^{tt}\omega^2\right)\Psi(u) = 0. \tag{6.3.69}$$

We then solve this EOM along with the EOM of $H(u)$ at equatorial embedding. The result of fluctuation analysis is shown in figure 6.15. From the plot, we see the
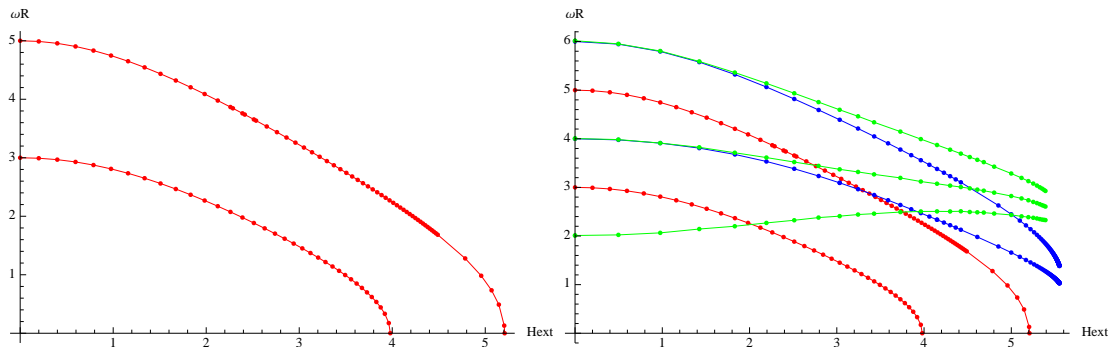
Figure 6.15: Left shows the first two normal modes of scalar fluctuation for equatorial embedding $mR = 0$ but vary external magnetic field. Right shows the left figure and figure 6.14 (right) plotted together. The data is obtained by a pole tracking method described in appendix A.3. It is interesting to see that the magnetic field makes the scalar fluctuation unstable.

scalar fluctuation becomes unstable when increasing the magnetic field to the value, $H_{ext} = 3.98$. This value exactly matches with the value $H_{ext,crit}$, where nearly all ball embeddings (except the equatorial one) disappear. Based on the informations so far we can conclude that if the model has the following features, then mass gap appears:

1. Scalar fluctuation at equatorial embedding is unstable for high enough magnetic field $H_{ext,crit}$. Although we still do not understand why scalar fluctuation is unstable for high enough magnetic field, studying fluctuation is easier and more intuitive than finding out why brane embeddings disappear.

2. The value of $H_{ext,m}$ where the lowest Minkowski embedding starts to be massless is greater than $H_{ext,crit}$. Unfortunately, since the start of this project we still have no way to understand this feature better.

It might give some insights to investigate if feature 1 also appears in other model especially in D3/D7 at finite temperature.

6.3.4 Fluctuation at Finite Temperature

As stated above, we would like to see if one of the features for mass gap also appears in other models. The closest model to investigate is D3/D7 at finite temperature. We find that the scalar fluctuation at finite temperature is also unstable when H_{ext} increased to a value. This value depends on temperature. The plots of poles of the scalar fluctuation at the temperature $\pi TR = 1.5$ are shown in figure 6.16. The relation between the critical H_{ext} where the scalar fluctuation is unstable and the temperature is plotted in figure 6.17. At $\pi TR = 1.5$, we find that the critical H_{ext} for the scalar fluctuation also corresponded to the value of H_{ext} that the black hole embeddings are completely disappeared. This confirms our discussion at the end of the above subsection. Generally, we expect that this feature remains true for any temperatures.

Just for completeness, we have analysed the vector and charged scalar fluctuations at finite temperature as well. As far as we can reach, when increasing H_{ext} from zero to some very high values, they do not show any instabilities. This result seemingly disagrees with D3/D7 Poincare analysis for vector fluctuation of [87]. However, we are not interested in investigating this further as it is beyond the scope of the project.

6.4 New Ground States at $\lambda \to \infty$

We will find the effects of the magnetic B-field to the meson new ground states. We start from the D7-brane action

$$
\begin{aligned}
S = &- T_{D7} \int d^8\sigma Str \sqrt{-\det(e_{ab} + 2\pi\alpha' F_{ab})} \\
&+ \frac{1}{2} T_{D7} \int tr(P[C_4] \wedge (B + 2\pi\alpha' F) \wedge (B + 2\pi\alpha' F)),
\end{aligned}
\tag{6.4.70}
$$

where the background fields are kept Abelian, but we promote gauge fields to non-Abelian. We then consider the action in $\lambda \to \infty$ limit:

$$
\begin{aligned}
S \approx &- T_{D7} \int d^8\sigma \sqrt{-e} Str \left(1 + \frac{1}{2} tr K + \frac{1}{4}((TrK)^2 - Tr(K^2)) - \frac{1}{8}(TrK)^2 \right) \\
&+ \frac{1}{2} T_{D7} \int tr(P[C_4] \wedge (B + 2\pi\alpha' F) \wedge (B + 2\pi\alpha' F)),
\end{aligned}
\tag{6.4.71}
$$

where $K_\nu^\mu = 2\pi\alpha'(e^{-1})^{\mu\alpha}F_{\alpha\nu}$, and Tr and tr are the traces over worldvolume and colour indices respectively. Note that

$$tr(TrK) = tr(\tau^a)K_\sigma^{\sigma(a)} = 0, \tag{6.4.72}$$

and

$$Str(TrK)^2 = Str(\tau^a\tau^b)K_{\sigma_1}^{\sigma_1(a)}K_{\sigma_2}^{\sigma_2(b)} = \frac{1}{2}K_{\sigma_1}^{\sigma_1(a)}K_{\sigma_2}^{\sigma_2(a)}. \tag{6.4.73}$$

The EOM of this term will contain $K_{\sigma_1}^{\sigma_1(a)}$ which is zero for our ansatz. However, for generality we will keep the term $Str(TrK)^2$ at the action level. We are finally left with the action of the form

$$S = S_{background} + S_1, \tag{6.4.74}$$

where

$$\begin{aligned}
\frac{S_1}{T_{D7}} &= \frac{(2\pi\alpha')^2}{4}\int d^8\sigma\sqrt{-e}\, tr\left((e^{-1})^{\sigma_1\sigma_2}F_{\sigma_2\sigma_3}(e^{-1})^{\sigma_3\sigma_4}F_{\sigma_4\sigma_1} - \frac{1}{2}(e^{-1})^{\sigma_1\sigma_2}F_{\sigma_1\sigma_2}(e^{-1})^{\sigma_3\sigma_4}F_{\sigma_3\sigma_4}\right) \\
&- \frac{(2\pi\alpha')^2}{2}\int d^8\sigma\sqrt{-e}\, tr\left((e^{-1})^{tt}D_t\Psi D_t\Psi + (e^{-1})^{uu}\partial_u\Psi\partial_u\Psi + 2(e^{-1})^{(ut)}D_t\Psi\partial_u\Psi - \frac{3\Psi^2}{R^2}\right) \\
&+ \frac{(2\pi\alpha')^2}{2}\int tr\left(P[C_4]\wedge F\wedge F\right),
\end{aligned} \tag{6.4.75}$$

where the second term is present for the uncharged scalar only. The EOM (not including the uncharged scalar) is given by

$$\begin{aligned}
D_{\sigma_4}\left(\sqrt{-e}\left((e^{-1})^{[\sigma_1|\sigma_2}F_{\sigma_2\sigma_3}(e^{-1})^{\sigma_3|\sigma_4]} + \frac{1}{2}(e^{-1})^{\sigma_2\sigma_3}F_{\sigma_2\sigma_3}(e^{-1})^{[\sigma_1\sigma_4]}\right)\right) & \\
- \frac{2}{R}\sqrt{-G_{tt}(u)G_{uu}(u)G_{33}^3(u)G(\bar{\Omega}_3)}\tilde{\epsilon}^{ijk}F_{ij}\delta_k^{\sigma_1} = 0, &
\end{aligned} \tag{6.4.76}$$

where i,j,k are indices on $S^3 \subset S^5$. Note that the sign on the second term should actually be positive. However, the sign change is because we are going to write charged scalar ansatz in polar spherical coordinates which has opposite orientation to Euler coordinates.

6.4.1 Charged Scalar Ground State

For numerical computation, it is more convenient to use z-coordinates. The ansatz for the charged scalar is

$$A = A_0^{(3)}(z)\tau^3 dt + \eta(z)(\sin^2\theta d\phi + \cos^2\theta d\psi)\tau^1. \tag{6.4.77}$$

We first consider the equatorial embedding $\chi(z) = 0$. For a given solution $H(z)$ of background EOM, we solve gauge field EOM. The boundary expansions are given by

$$A_0^{(3)}(z) = \mu - \rho z^2 + \cdots , \qquad (6.4.78)$$

$$\eta(z) = R\rho_\eta z^2 + \cdots . \qquad (6.4.79)$$

The numerical results are shown in figure 6.18 and 6.19.

The magnetic field (let us call it $\bar{F}$) of [86] and our B-field B are related by

$$\frac{1}{\lambda}\bar{F} \sim B. \qquad (6.4.80)$$

The $\lambda \to \infty$ limit makes the action of $\bar{F}$ reduced to YM but retains DBI action for B. Also, this limit means that in order to obtain a finite B, we need large $\bar{F}$. Our figure 6.18 and the left plot of figure 11 of [86] are describing qualitatively equivalent things. The behaviour of μ_{crit} for small H_{ext} qualitatively matches with the monotonically increasing behaviour for any $\bar{F}$. However, the behaviour for sufficiently large H_{ext} (≈ 4) cannot be compared with [86] as this is a large $\bar{F}$ limit that the analysis of [86] cannot cover.

Figure 6.19 tells us that at fixed chemical potential, the densities generally decrease as external magnetic field is increased suggesting the magnetic effect to diminish the new ground state as found in e.g. [86]. For small enough chemical potential, there is a critical value of H_{ext} beyond which the densities vanish completely or nearly completely. For sufficiently high chemical potential, however, there are no such critical external magnetic field.

Having understood the role of external magnetic field on the new ground state, it is useful to go back to discuss figure 6.18. For a given chemical potential in the range $2 < \mu R \lesssim 2.31$, there exists a critical value of external magnetic field beyond which the new ground state is completely destroyed. For a given μ in the range $2.31 < \mu R \lesssim 2.50$, there is a critical value $H_{crit,1}$ that destroys the new ground state. However, there is a value $H_{crit,2} > H_{crit,1}$ beyond which the new ground state is restored. For example, when $\mu R = 2.4$, the critical values are $H_{crit,1} = 2.97, H_{crit,2} = 5.13$. Finally, when $\mu R \gtrsim 2.50$, the ground states are not destroyed by external magnetic field.

6.4.2 Vector Ground State

Starting with the same procedure with charged scalar new ground state, we have the vector ground state ansatz

$$A = A_0^{(3)}(z)\tau^3 dt + \psi(z)(\sin^2 \bar{\theta} d\bar{\phi} + \cos^2 \bar{\theta} d\bar{\psi})\tau^1. \qquad (6.4.81)$$

Again, we consider the equatorial embedding $\chi(z) = 0$. For a given solution $H(z)$ of background EOM, we solve gauge field EOM. The boundary expansions are given by

$$A_0^{(3)}(z) = \mu - \rho z^2 + \cdots, \qquad (6.4.82)$$

$$\psi(z) = R\rho_\psi z^2 + \cdots. \qquad (6.4.83)$$

The numerical results are shown in figure 6.20 and 6.21.

Figure 6.21 tells us that at fixed chemical potential, the densities increase as external magnetic field is increased. For small enough chemical potential, there is a critical value of H_{ext} beyond which new ground state is created. The feature where magnetic field enhances the new ground state is not expected from e.g. [86].

6.4.3 Scalar Ground State

Starting with the similar procedure with charged scalar and vector new ground state, we make an ansatz for equatorial embedding $\chi(z) = 0$:

$$A = A_0^{(3)}(z)\tau^3 dt, \qquad (6.4.84)$$

$$\chi = (2\pi\alpha')^2 \Phi(z)\tau^1. \qquad (6.4.85)$$

We do the same as the previous subsections. The boundary expansions are given by

$$A_0^{(3)}(z) = \mu - \rho z^2 + \cdots, \qquad (6.4.86)$$

$$\Phi(z) = \rho_\Phi z^3 + \cdots. \qquad (6.4.87)$$

It takes too long to extract the numerical result for new ground state. It is approximately at least 10 times longer than vector case. So we might extract only some sample points. This remains a work in progress.

Nevertheless, based on the fact that at zero temperature the fluctuation frequency and the new ground state's chemical potential appear at the same place in EOM, we can, as always, predict the phase diagram based on fluctuation analysis. There is an issue that we cannot understand what happens at the region corresponding to mass gap. This diagram is in figure 6.22. For $H_{ext} > 3.98$ the region marked ??? for small chemical potential is the most problematic. We have no idea what the ground state look like. In fact, had we known this, we would have been able to 'cover' the mass gap. To elaborate on this point, let us consider chemical potential around $\mu R = 2$. Increasing external magnetic field will make new ground state appears and it should be enhancing as we further increase external magnetic field. But then suddenly, when $H_{ext} = 3.98$, there is no solution corresponding to new ground state: it does not simply disappear thermodynamically. Let us now consider high enough chemical potential, e.g. $\mu R = 4$. Formally, there would always be new ground state. However at $H_{ext} = 3.98$, we expect the discontinuity in densities since the new ground state for $H_{ext} < 3.98$ is based on the 'first branch' while the one for $H_{ext} > 3.98$ is based on the 'second branch'.

6.5 Discussion

We find that the magnetic Kalb-Ramond field affects the D3/D7 system in compact size in many interesting ways. One of them is the mass gap feature that does not exist in the non-compact case[5]. This arises because of the regularity requirement of the field at the AdS centre. In the non-compact case boundary conditions are not imposed at the AdS centre but rather at the Poincaré horizon, and hence there is no need for the field to be regular there. The mass gap feature emphasises the difference between the ball and Minkowski embeddings in the gravity side, and there is no smooth transition between them. We expect a phase transition to exists also in the field theory. Work is in progress to analyse the brane embeddings by shooting from infinity rather than from the origin, which may shed light on the reason for

---

[5]The results for the non-compact case can be found in [78, 79], in which there is no mass gap found.

the existence of the mass gap.

Another interesting effect is the instability of the scalar meson. We expect that this is related to the mass gap feature because of the fact that the critical magnetic field coincides for both phenomena. The instability will lead to a new ground state. We expect that this new ground state will be such that it covers the mass gap, but a construction of it will be left for future work.
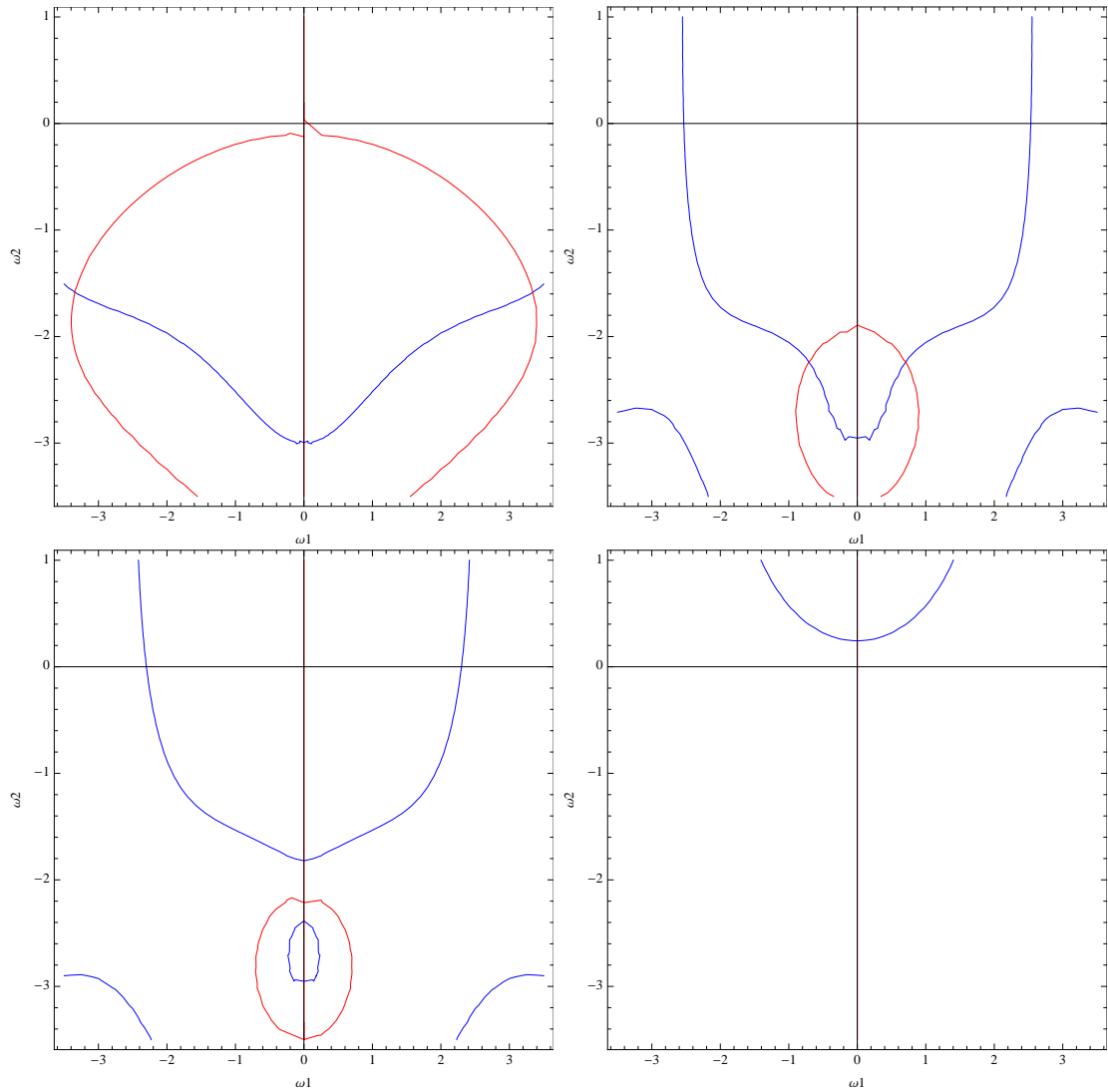
Figure 6.16: The plots of poles of the scalar fluctuation at $\pi TR = 1.5$: from left to right and top to bottom, $H_{ext} = 0, 6.33, 7.29, 18.17$. The blue/red curves indicate the real/imaginary parts of the fluctuation field at the boundary vanish.
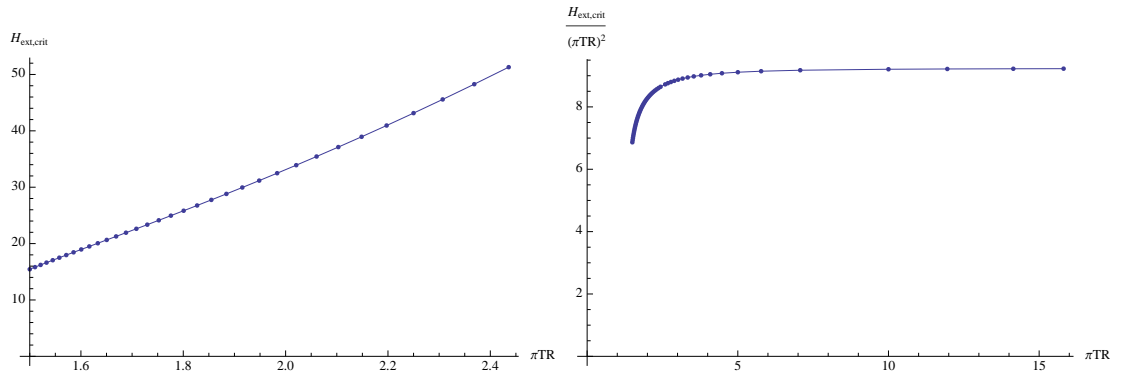
Figure 6.17: The left plot is the relation between the critical magnetic field $H_{ext,crit}$ and the temperature πTR from the scalar fluctuation. The right plot has the same data as the left one with some additional points, and the vertical axis is scaled by $(\pi TR)^2$. The right plot shows the asymptotic value at high πTR which is the Poincaré limit $(H_{ext,crit}/(\pi TR)^2 = 9.24)$.
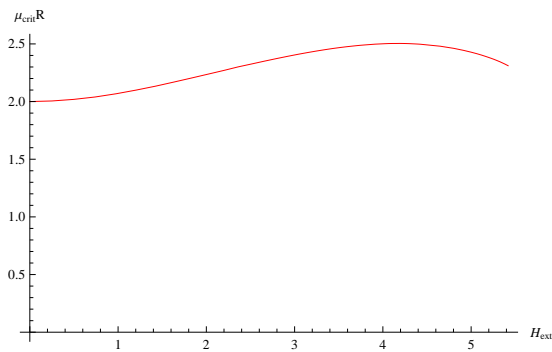
Figure 6.18: The numerical results for charged scalar new ground state in $\lambda \to \infty$ limit and equatorial embedding. Critical chemical potential for each applied external magnetic field is shown.
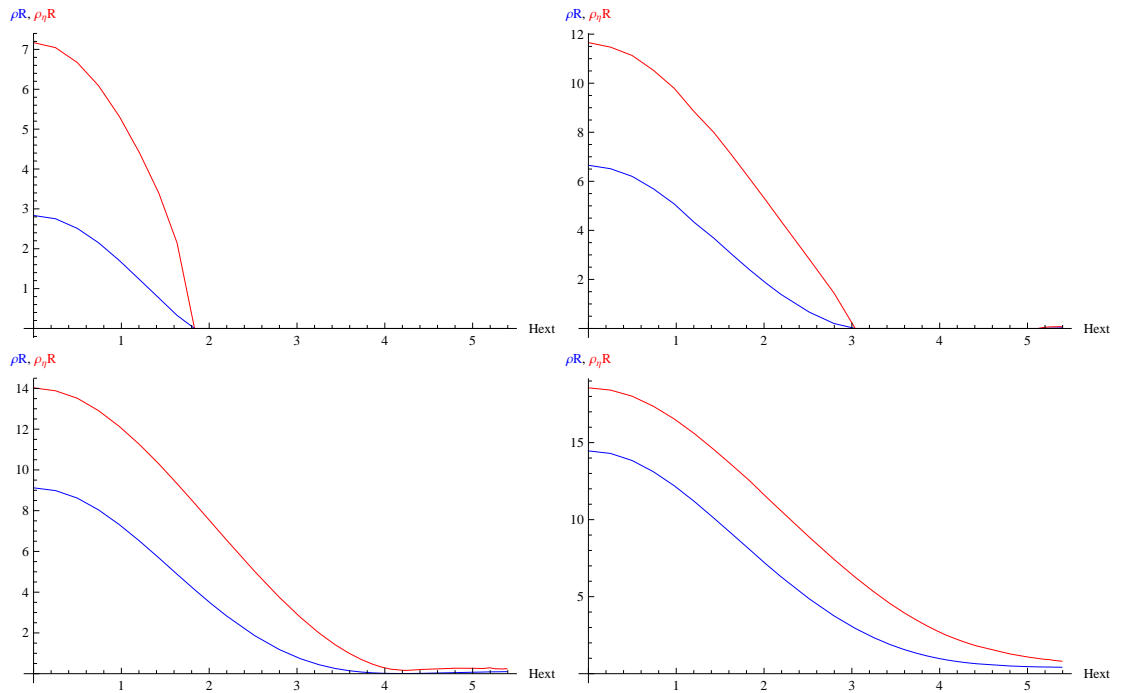
Figure 6.19: The numerical results for charged scalar new ground state in $\lambda \to \infty$ limit and equatorial embedding. The densities at a given value of isospin chemical potential are shown. From Left to Right and Top to Bottom: $\mu R = 2.2, 2.4, 2.507, 2.7$.
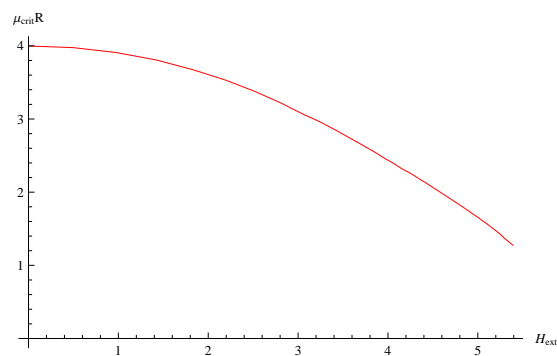
Figure 6.20: The numerical results for vector new ground state in $\lambda \to \infty$ limit and equatorial embedding. Critical chemical potential for each applied external magnetic field is shown.
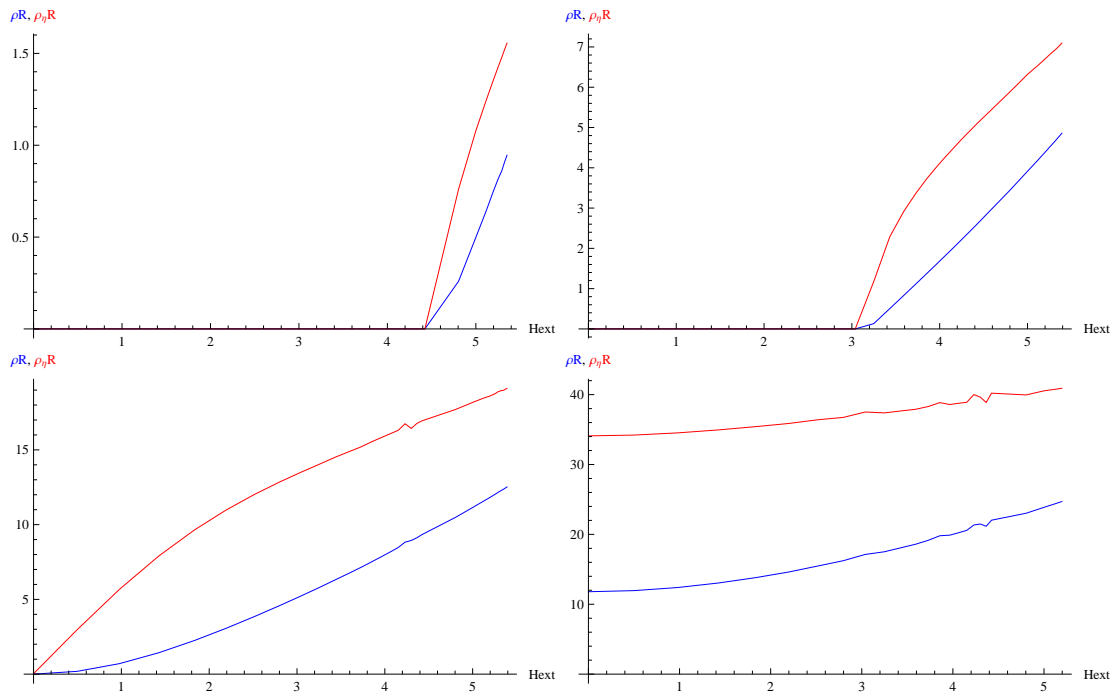
Figure 6.21: The numerical results for vector new ground state in $\lambda \to \infty$ limit and equatorial embedding. The densities at a given value of isospin chemical potential are shown. From Left to Right and Top to Bottom: $\mu R = 2, 3, 4, 5$.
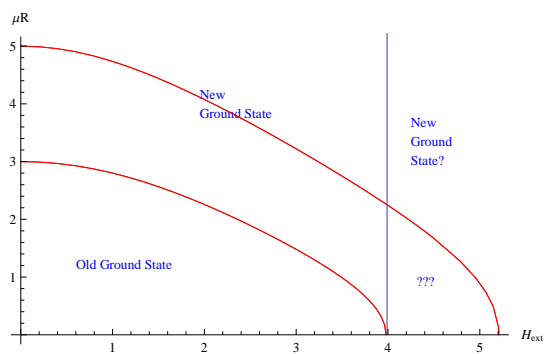
Figure 6.22: The expected phase diagram for scalar new ground state in $\lambda \to \infty$ limit and equatorial embedding. Due to the mass gap behaviour, it is not certain about the new ground state for $H_{ext} > 3.98$.

Chapter 7

Conclusions

We have studied the holography in the context of the AdS/CFT correspondence. We have chosen to study the duality between the type IIB supergravity in AdS spacetime and $\mathcal{N} = 4$ and $\mathcal{N} = 2$ SYM, and we investigate the system in compact size. We have seen finite-size effects from the results in chapter 4, 5 and 6. Let us summarise what we have done in and the results from those chapters, which contain our own works.

In chapter 4, we study the drag force exerted on a quark moving through the QGP. The gauge theory is $\mathcal{N} = 4$ SYM, and we study it from its dual gravity theory. In compact size, the finite-size effect we found is the reduction of the magnitude of the drag force. This is quite unusual when compared to the Newtonian fluid, where the compact-size effect increases the magnitude of the drag force.

In chapter 5, we investigate the meson spectra and new ground states of the $\mathcal{N} = 2$ SYM theory from the gravity side with the isospin chemical potential. One of the results we found is that when the chemical potential increases the first excitation is an $SO(4)$ charged scalar meson. This is not a finite-size effect as it survives in the non-compact case. The fact that the first excitation is the charged scalar meson contrasts other related models such as [66,73] where the first excitation is the vector. Moreover, the interesting finite-size effect we found is that the meson spectra of the vector and scalar mesons cross over each other as functions of temperature and system size. This suggests some complexity in the model. For example, at high enough chemical potential, there would be a transition between vector and scalar

meson ground states by just adjusting the temperature and/or the system size.

In chapter 6, we study the influence of a magnetic Kalb-Ramond field to the $\mathcal{N} = 2$ SYM theory holographically. We found a region, which we called 'mass gap', at which there are still no appropriate configurations that give the values of external magnetic field and quark mass. This is not the feature in the non-compact case. Another interesting result is the instability of the scalar meson due to the external magnetic field. Sharing the same critical magnetic field, the mass gap and the scalar instability are somehow related. If we had known how to build the new ground state for the scalar meson, we would be able to fill in the mass gap, so what does the new ground state look like? We leave this as an open question and our future plan.

Some of those compact-size effects should be realised in the more real world model if we have one. In reality, we cannot have the system with infinite size. There must be a size associated with it. For the model this means we have an additional scale. More phase transitions are then expected to occur. It is interesting to investigate the finite-size effect in other models where the system has been treated as infinite size.

Appendix A

Computational Techniques

A.1   The Shooting Method

In our works, we encounter many ordinary differential equations (ODE) that cannot be solved analytically. We need to solve them by using numerical methods. There are various types of the numerical methods suitable for particular problems. The differential equations we worked with have the solution known at the initial point, and we want to find the solution at the boundary. Therefore, the most well-fit numerical method we need to use is the shooting method.

Let us quickly illustrate how the shooting method is used to solve the second order ODE. The shooting method indeed changes the boundary value problem to the initial value one. In our problem, the second order ODE is in the form

$$y''(x) = f(y'(x), y(x); x). \tag{A.1.1}$$

Let the starting point be at x_0, so the initial values are $y(x_0) = y_0$ and $y'(x_0) = y'_0$. To find the solution at the boundary x_b, we suppose the solution has the boundary values $y(x_0) = y_0$ and $y(x_b) = y_b$. We can define the function [88]

$$F(y'_0) = y(x_b; y'_0) - y_b, \tag{A.1.2}$$

where $y(x_b; y'_0)$ is the solution at x_b obtained from the initial values. If the boundary value problem has a solution, the function F has a root [88]. There are many methods to find the root. In our case, we will find the root by using the function

NDSolve in Mathematica, which will automatically select the most suitable method for us.

A.2 Using NDSolve to Solve ODEs around Regular Singular Points

In this section, we will demonstrate how to numerically solve a second-order ODE where the initial condition is at the regular singular point. We are not able to directly use NDSolve to solve the ODE from the regular singular point as Mathematica will fail to compute the infinite expression $1/0$. We have to find the expansion of the solution near the singular point first, and then we can use NDSolve. Let us show the steps by considering the second-order ODE in the form of

$$y''(x) + p(x)y'(x) + q(x)y(x) = 0, \tag{A.2.3}$$

where the initial condition at the singular point $x = 0$ is $\{y(0) = a, \ y'(0) = b\}$. The functions $p(x)$ and $q(x)$ are singular at $x = 0$, and the quantities

$$\lim_{x \to 0} x\, p(x) \qquad \text{and} \qquad \lim_{x \to 0} x^2 q(x) \tag{A.2.4}$$

are finite to ensure $x = 0$ is a regular singular point. The expansion of $y(x)$ can be found by using the Frobenius power series

$$y(x) = x^r \sum_{k=0}^{n} c_k x^k, \tag{A.2.5}$$

where c_k's are the coefficients. Since Mathematica cannot handle this with infinite number of coefficients as in the 'proper' Frobenius method, n cannot be infinite and is the number of coefficients we want to find[1]. Then we substitute the expansion to the ODE and make the series expansion of the ODE. Next, we use Mathematica

---

[1]It would be better to consider the form of the expansion as $y(x) = x^r \sum_{k=0}^{n} c_k x^k + err(x)$, where $err(x)$ is an error term. In this case, we can specify an error from the numerical computation. However, as far as we are concerned, Mathematica has large enough digit precision; we can go very near the singular point as long as the rounding effect does not become dominant, and the error estimate would be as small as 10^{-6}, for example, which somehow can be neglected.

to identify the coefficients c_k's and then find the expansion of the solution near the singular point. An example of the Mathematica code to do this job is written in the figure A.1.

Now we are able to use NDSolve; the code is in the figure A.2. Note from the figure that the initial condition changes from the functions at the singular point $\{y(0) = a, y'(0) = b\}$ to their expansions near the singularity $\{y(x_0), y'(x_0)\}$, where $\lim_{x_0 \to 0} y(x_0) = a$, $\lim_{x_0 \to 0} y'(x_0) = b$ and x_0 is a little different from 0.

A.3 Pole Tracking

In the fluctuation analysis, we need to locate the first pole as it represents the physical mode. Basically, the pole will move if we change a related parameter. The pole is located at the point where the Green's function diverges. Since the numerical computing for each value of the parameters may take a long time, tracking the pole by directly applying ContourPlot to the Green's function would be a tedious job. We make it a lot better by, for the parameter k,

1. Replacing the Green's function by a corresponding function that is quicker to compute and gives the zero value at the pole; in our case the function is just the solution from the ODE evaluated at the boundary.

2. Estimating the position of the pole at the starting value of k by ContourPlot

3. Using FindRoot to precisely obtain the pole position

4. Slightly changing the value k

5. Using the previous result as a guess of the new position of the pole for the new k

6. Repeating the step 3 through 5 until having all the needed data

An example of the code to work from the step 3 to 5 is written in the figure A.3.

A.4 Curve Selecting Algorithm

For the work in chapter 5 and 6, while we were trying to find the new ground state we encountered a ridiculous routine that we had to choose the physical curve from the plot such as the one in figure A.4. In that plot, we have to pick the most left curve that gives the physical and stable solution. Unfortunately, when extracting the curves from the plot, Mathematica does not number them naturally in ascending or descending order from left to right, for example[2]. To choose the most left curve, we then have to guess the number of that curve. The worst case is that the number of times we guess is the number of the curves in the plot. Doing this for all values of the associated parameters such as temperature may unreasonably waste a large amount of time. However, there are still ways to have the computer doing this for us. It is obvious that the curves on the left are going to touch the horizontal axis at the less horizontal values than the curves on the right. For the data of each curve, Mathematica represents it as a set of order points i.e. $\{\{x_1, y_1\}, \{x_2, y_2\}, \ldots\}$. Our algorithm to pick the most left curve are:

1. Searching for the order points that have the minimum values of the vertical axis for each curve

2. Comparing those order points between the curves and choosing one with the lowest horizontal value

3. At this horizontal value, estimating the vertical value for every curve and just ignoring the curves that do not cross this horizontal value

4. Obtaining the curve we want by the fact that the curve will have the lowest estimated vertical value from the last step[3]

---

[2]A slightly change in the plot may yield the labels of the curves completely shuffled. Also, for the same plots but with slightly different ranges Mathematica may give totally different sets of the labels.

[3]The curves are indeed arranged from left to right by the estimated vertical values from the step 3. This is valid for only the curves that pass through or touch the horizontal value in this step. For the others, we can reapply the steps 2 and 3 to them if we want to arrange all of them.

An example of the Mathematica code doing this algorithm is shown in the figure A.5.

A.5 S^3 Spherical Harmonic Expansions

Our works focus on what happen in the holographic field theory in compact space. The compact space is S^3. The field on S^3 naturally has the mode expansion in the S^3 spherical harmonics. For example, a scalar field on S^3 has the mode expansion as

$$\Phi(\Omega_3) = \sum_{l,m_1,m_2} C_{l,m_1,m_2} Y_{l,m_1,m_2}(\Omega_3), \tag{A.5.6}$$

where Y_{l,m_1,m_2} is the S^3 scalar spherical harmonic, C_{l,m_1,m_2} is the coefficient and $\{l,m_1,m_2\}$ are quantum numbers of the spherical harmonic. For the vector field, the mode expansion is

$$\Phi^i(\Omega_3) = \sum_{l,m_1,m_2,s} C_{l,m_1,m_2,s} \Pi^i_{l,m_1,m_2,s}(\Omega_3), \tag{A.5.7}$$

where $\Pi^i_{l,m_1,m_2,s}$ is the S^3 vector spherical harmonic in the direction x^i and $\{l,m_1,m_2,s\}$ are its quantum numbers. This can also be done for general rank tensor fields; see [89] for more detail. In our works, we encounter the expression such as $Y_{l,m_1,m_2}Y_{l',m'_1,m'_2}$ which is a result of two fields coupled to each other. This expression needs to be expand in a sum of single spherical harmonics in order to factor out the angular dependence. The formulae can be found in [89]. To save time, we wrote Mathematica codes to do the expansions. Starting with the $SU(2)$ and S^3 Clebsch-Gordan coefficients, which play a role in the expansion, we write the code in the figure A.6 and A.7. The codes to generate the spherical harmonic expansions of the multiplication between the scalar spherical harmonics and the vector ones are in the figures A.8, A.9 and A.10. Additionally, after running the codes in the figures A.8, A.9 and A.10, it would be safe to restore the attributes to the operators.

```
p[x_] := 1 / x;
q[x_] := 3 x;
n = 30;
m = 7;
(*Thing above is an example of input*)
(*The code actually begins here*)
Module[{r}, eqny[x_] := y''[x] + p[x] y'[x] + q[x] y[x];
   indicialr = Solve[r (r - 1) + Limit[x p[x], x → 0] r + Limit[x^2 q[x], x → 0] == 0, r];
   (*If |r1-r2| is integer, deltar1r2int will be True; otherwise False*)
   deltar1r2int = IntegerQ[(r /. indicialr[[1]]) - (r /. indicialr[[2]])];
   (*y1 is the series of 1st soln with undetermined coefficients*)
   y1[x_] := x^If[deltar1r2int, Max[r /. indicialr], r /. indicialr[[1]]]
     Sum[c[i] x^i, {i, 0, n}];
   (*Find coefficients of y1*)
   coeffy1 = Solve[! Eliminate[
       ! (Series[x^ (-If[deltar1r2int, Max[r /. indicialr], r /. indicialr[[1]]])
              eqny[x] /. y → y1, {x, 0, m}] == 0), x], Table[c[i], {i, 0, n}]];
   (*1st series soln with coefficients determined*)
y1expn[x_] = If[Length[coeffy1[[1]]] > 0,
     x^If[deltar1r2int, Max[r /. indicialr], r /. indicialr[[1]]]
       Sum[c[i] x^i, {i, 0, Length[coeffy1[[1]]]}] /. coeffy1[[1]], 0];
   (*y2 is the series of 2nd soln with undetermined coefficients*)
   y2[x_] := If[deltar1r2int, If[Length[Union[indicialr]] == 1,
     y1expn[x] Log[x] + x^r Sum[d[i] x^i, {i, 0, n}] /. indicialr[[1]],
     d[0] y1expn[x] Log[x] + x^Min[r /. indicialr] (1 + Sum[d[i] x^i, {i, 1, n}])],
    x^r Sum[d[i] x^i, {i, 0, n}] /. indicialr[[2]]];
   (*Find coefficients of y2*)
   coeffy2 = Solve[! Eliminate[
       ! (Series[x^ (-If[deltar1r2int, Min[r /. indicialr], r /. indicialr[[2]]])
              eqny[x] /. y → y2, {x, 0, m}] == 0), x], Table[d[i], {i, 0, n}]];
   (*2nd series soln with coefficients determined*)
   y2expn[x_] = If[deltar1r2int, If[Length[Union[indicialr]] == 1,
       y1expn[x] Log[x] + x^r Sum[d[i] x^i, {i, 0, Length[coeffy2[[1]]]}] /.
        indicialr[[1]], d[0] y1expn[x] Log[x] + x^Min[r /. indicialr]
          (1 + Sum[d[i] x^i, {i, 1, Length[coeffy2[[1]]]}])], If[
       Length[coeffy2[[1]]] > 0, x^r Sum[d[i] x^i, {i, 0, Length[coeffy2[[1]]]}] /.
        indicialr[[2]], 0]] /. coeffy2[[1]];];
(*Linear combination of 1st and 2nd series solns*)
yexpn[C1_, C2_][x_] =
 C1 (y1expn[x] /. {c[_] → 1(*or any other convinient number*)}) +
   C2 (y2expn[x] /. {c[_] → 1, d[_] → 1(*or any other convinient numbers*)})
```

Figure A.1: Mathematica 8 code used to generate the expansions near $x = 0$ of the solution to the second-order linear ODE. Note that the inputs p[x] and q[x] are the functions in (A.2.3) and should be able to be expanded in the forms of x^{-1}(a power series) and x^{-2}(a power series) respectively. n is the same as one in (A.2.5). m is the number of terms in the expansion of the ODE, in which the function Series will generate, and has to correspond to n i.e. every term in the expansion of the ODE must not have any c_k's (c[i], d[i]) lost due to the fact that the expansion of $y(x)$ does not have enough terms. (This figure is associated with appendix A.2.)

```
x0 = 1 / 1000(*or any other value near zero*);
xfinal = 10(*specifying the final position*);
diffsoln[C1_, C2_] := NDSolve[{eqny[x] == 0, y[x0] == yexpn[C1, C2][x0],
      y'[x0] == yexpn[C1, C2]'[x0]}, y, {x, x0, xfinal}];
(*An example of the solution can be seen by*)
Plot[Evaluate[y[t] /. diffsoln[1, 2]], {t, x0, xfinal}]
```

Figure A.2: Mathematica 8 code showing the use of NDSolve to numerically solve the second-order linear ODE near a regular singular point ($x = 0$) where the initial conditions are derived from the expansion of the solution obtained from the code in the figure A.1. (This figure is connected with appendix A.2.)

```
kstart = 0; kstop = 10; dk = 1 / 10; (*Example of starting,
stopping and increment values*)
ktable = Table[i, {i, kstart, kstop, dk}](*Contains all k's*);
ωinitestmtd = 4 - 3 I (*for example*);
k = ktable[[1]](*Begin from starting value*);
(*Find the exact pole position at starting value of k*)
polepositions = {{k, ω /. Quiet[FindRoot[
        Xvec[vfinal] /. ndsolveXvec(*function to find the pole;
        the pole locates at the zero of this function evaluated at vfinal*),
        {ω, ωinitestmtd}], {NDSolve::ndinnt, ReplaceAll::reps}]]}};
(*Then move to the next k and find the pole, and repeat until done*)
Do[
 k = ktable[[nth]];
 polepositions =
  polepositions ~ Join ~ {{k, ω /. Quiet[FindRoot[Xvec[vfinal] /. ndsolveXvec, {ω,
         polepositions[[nth - 1, 2]]}]], {NDSolve::ndinnt, ReplaceAll::reps}]]}},
 {nth, 2, Length[ktable]}]
```

Figure A.3: Mathematica 8 code used to track a zero-value point of a numeric function, Xvec, evaluated at vfinal. In this case, k is the parameter with the starting value kstart, the stopping value kstop and the increment step dk. The zero-value point is on the complex plane ω. ωinitestmtd is the estimated zero-value point from ContourPlot, for example. The output variable is polepositions and will be in the form of $\{\{\text{kstart}, \omega_{\text{kstart}}\}, \{\text{kstart}+\text{dk}, \omega_{\text{kstart}+\text{dk}}\}, \{\text{kstart}+2\text{dk}, \omega_{\text{kstart}+2\text{dk}}\}, \ldots\}$, where ω_t is the pole position when k $= t$. (This figure is linked to appendix A.3.)
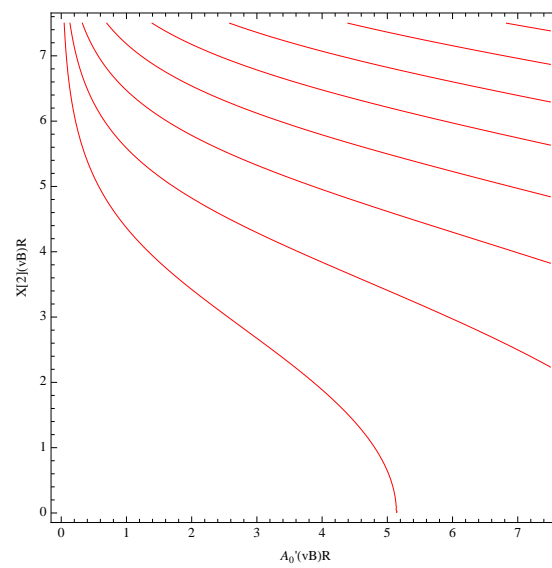
Figure A.4: The plot of the initial condition that yields the physical solution for the scalar new ground state at the temperature $\pi TR = 1.5$. (This figure is connected with appendix A.4.)

```
Needs["Combinatorica`"];(*to perform BinarySearch*)
(*Sort the data points of each curve by vertical axis values and then sort
 the curves by the horizontal values of their lowest(miny) points*)
minypointswithlabelssortedbyx = Sort[Join[Table[{i}, {i, Length[#]}], #, 2] &[
    Flatten[Map[Sort[#, #1[[2]] < #2[[2]] &] &, datapoints], {{2}, {1}, {3}}][[
    1]]], #1[[2]] < #2[[2]] &];
(*For each curve, this contains the data points sorted
 by the horizonal values*)
sorteddatapoints = Map[Sort[#, #1[[1]] < #2[[1]] &] &, datapoints];
(*For each curve, search for the position of the data points that the
 selected horizontal value (look at step 3 in the algorithm) would be
 in. If there exists the datapoint with the selected horizonal value,
the "return number" will be integer (the position of that data point);
otherwise, it will be half integer indicating the
 position between ones with the higher and lower values*)
pointpositionsofthex =
  Map[BinarySearch[#, minypointswithlabelssortedbyx[[1, 2]], #[[1]] &] &,
    sorteddatapoints];
estimatedy = {} (*This will be {{curve1,estimatedy1},
    {curve2,estimatedy2},...}*);
(*Begin to estimate the vertical values for each curve*)
Do[If[1 ≤ pointpositionsofthex[[nthcurve]] ≤
    Length[sorteddatapoints[[nthcurve]]], estimatedy = estimatedy~
     Join~{{nthcurve, If[IntegerQ[pointpositionsofthex[[nthcurve]]],
        (*If the "return number" is integer,
        we just return the vertical position of that data point*)
        sorteddatapoints[[nthcurve, pointpositionsofthex[[nthcurve]], 2]],
        (*If the "return number" is not integer,
        we have to interpolate the vertical value associate to the
         selected horizon value*)Interpolation[sorteddatapoints[[
           nthcurve, Max[Floor[pointpositionsofthex[[nthcurve]]], 1]
            ;; Min[Ceiling[pointpositionsofthex[[nthcurve]]],
             Length[sorteddatapoints[[nthcurve]]]]]], InterpolationOrder → 1][
         minypointswithlabelssortedbyx[[1, 2]]]]}}],
  {nthcurve, Length[sorteddatapoints]}];
(*Please refer to step 4 in the algorithm;
the numbers in the output indicate the list positions
 in which the data of the particular curves contains*)
lefttorightorder = Transpose[Sort[estimatedy, #1[[2]] < #2[[2]] &]][[1]]
```

Figure A.5: Mathematica 8 code used to select the most left curve in, for example, the plot of the figure A.4. The variable named datapoints contains the order points of the plots in the form of $\{\{\{x_{i_1,j_1}, y_{i_1,j_1}\}, \{x_{i_1,j_2}, y_{i_1,j_2}\}, \ldots\}, \{\{x_{i_2,j_1}, y_{i_2,j_1}\}, \{x_{i_2,j_2}, y_{i_2,j_2}\}, \ldots\}, \ldots\}$ where i's label the curves and j's label the order points for each curve. The output is a set in which the label of the most left curve is the first element, and the next element is the label of the nearby right curve and so on. Since the code is not written to arrange all the curves, the labels of some far right curves may disappear from the output. For more details, see the footnote 3 in the page 114. (This figure is associated with appendix A.4.)

```
CSU2[j_, j1_, m1_, j2_, m2_] :=
 If[Abs[j1 - j2] ≤ j ≤ j1 + j2 && - j1 ≤ m1 ≤ j1 && - j2 ≤ m2 ≤ j2 && Abs[m1 + m2] ≤ j &&
    Mod[j1 + m1, 1] == 0 && Mod[j2 + m2, 1] == 0,
  Module[{k = 0, sum = 0},
   While[(j - j2 + m1 + k) < 0 || (j - j1 - m2 + k) < 0, k++];
   While[(j1 + j2 - j - k) ≥ 0 && (j1 - m1 - k) ≥ 0 && (j2 + m2 - k) ≥ 0,
    sum += (-1) ^k / (k! * (j1 + j2 - j - k) ! * (j1 - m1 - k) ! *
        (j2 + m2 - k) ! * (j - j2 + m1 + k) ! * (j - j1 - m2 + k) !); k++];
   Sqrt[(2 j + 1) (j + j1 - j2) ! (j - j1 + j2) ! (j1 + j2 - j) ! / ((j1 + j2 + j + 1) !)] * Sqrt[
     (j + m1 + m2) ! (j - m1 - m2) ! (j1 - m1) ! (j1 + m1) ! (j2 - m2) ! (j2 + m2) !] * sum], 0]
```

Figure A.6: Mathematica 8 code used to compute the $SU(2)$ Clebsch-Gordan coefficients represented by $CSU2$. (This figure is connected with appendix A.5.)

```
CS3[j_, l_, m1_, m2_, lp_, m1p_, m2p_] :=
 If[Abs[l - lp] ≤ j ≤ l + lp && - l ≤ 2 m1 ≤ l && - l ≤ 2 m2 ≤ l && - lp ≤ 2 m1p ≤ lp &&
    - lp ≤ 2 m2p ≤ lp && 2 Abs[m1 + m1p] ≤ j && 2 Abs[m2 + m2p] ≤ j &&
    Mod[l / 2 + m1, 1] == 0 && Mod[l / 2 + m2, 1] == 0 && Mod[lp / 2 + m1p, 1] == 0 &&
    Mod[lp / 2 + m2p, 1] == 0 && Mod[j / 2 + m1 + m1p, 1] == 0 && Mod[j / 2 + m2 + m2p, 1] == 0,
  Sqrt[(l + 1) (lp + 1) / (j + 1)] CSU2[j / 2, l / 2, m1, lp / 2, m1p]
   CSU2[j / 2, l / 2, m2, lp / 2, m2p], 0]

DS3[j_, l_, m1_, m2_, s_, lp_, m1p_, m2p_, sp_] :=
 If[Abs[l - lp] + Abs[s - sp] ≤ j ≤ l + lp - Abs[s + sp] &&
    - l - s ≤ 2 m1 ≤ l + s && - l + s ≤ 2 m2 ≤ l - s && - lp - sp ≤ 2 m1p ≤ lp + sp &&
    - lp + sp ≤ 2 m2p ≤ lp - sp && 2 Abs[m1 + m1p] ≤ j && 2 Abs[m2 + m2p] ≤ j &&
    Mod[(l + s) / 2 + m1, 1] == 0 && Mod[(l - s) / 2 + m2, 1] == 0 &&
    Mod[(lp + sp) / 2 + m1p, 1] == 0 && Mod[(lp - sp) / 2 + m2p, 1] == 0 &&
    Mod[j / 2 + m1 + m1p, 1] == 0 && Mod[j / 2 + m2 + m2p, 1] == 0 && Abs[s] == Abs[sp] == 1,
  - Sqrt[l (l + 1) (l + 2) lp (lp + 1) (lp + 2) / (j + 1)] *
   SixJSymbol[{j / 2, l / 2, lp / 2}, {1 / 2, (lp + sp) / 2, (l + s) / 2}] *
   SixJSymbol[{j / 2, l / 2, lp / 2}, {1 / 2, (lp - sp) / 2, (l - s) / 2}] *
   CSU2[j / 2, (l + s) / 2, m1, (lp + sp) / 2, m1p]
   CSU2[j / 2, (l - s) / 2, m2, (lp - sp) / 2, m2p], 0]

GS3[j_, l_, m1_, m2_, s_, lp_, m1p_, m2p_] :=
 If[Abs[l - lp] + 1 ≤ j ≤ l + lp - 1 && - l - s ≤ 2 m1 ≤ l + s && - l + s ≤ 2 m2 ≤ l - s &&
    - lp ≤ 2 m1p ≤ lp && - lp ≤ 2 m2p ≤ lp && 2 Abs[m1 + m1p] ≤ j && 2 Abs[m2 + m2p] ≤ j &&
    Mod[(l + s) / 2 + m1, 1] == 0 && Mod[(l - s) / 2 + m2, 1] == 0 && Mod[lp / 2 + m1p, 1] == 0 &&
    Mod[lp / 2 + m2p, 1] == 0 && Mod[j / 2 + m1 + m1p, 1] == 0 && Mod[j / 2 + m2 + m2p, 1] == 0 &&
    Abs[s] == 1, - Sqrt[l (l + 1) (l + 2) (lp + 1) / (8 (j + 1))] *
   Sum[k (k + 1) (k + 2) SixJSymbol[{j / 2, l / 2, k / 2}, {1 / 2, lp / 2, (l + 1) / 2}] *
     SixJSymbol[{j / 2, l / 2, k / 2}, {1 / 2, lp / 2, (l - 1) / 2}], {k, {lp - 1, lp + 1}}] *
   CSU2[j / 2, (l + s) / 2, m1, lp / 2, m1p] CSU2[j / 2, (l - s) / 2, m2, lp / 2, m2p], 0]
```

Figure A.7: Mathematica 8 code used to compute the S^3 Clebsch-Gordan coefficients represented by $CS3$, $DS3$ and $GS3$. (This figure is associated with appendix A.5.)

```
ClearAttributes[Times, Protected];
Y[l_, m1_, m2_] * Y[lp_, m1p_, m2p_] :=
  Sum[CS3[j, l, m1, m2, lp, m1p, m2p] Y[j, m1 + m1p, m2 + m2p], {j, Abs[l - lp], l + lp}]

ClearAttributes[Power, Protected];
Y[l_, m1_, m2_]^n_ /; (n ≥ 2 || n ≤ -2) :=
  Module[{sum = 1}, For[i = 0, i < Floor[Abs[n]], i++, sum *= Y[l, m1, m2]]; If[n > 0,
    sum * Y[l, m1, m2]^(n - Floor[n]), (sum^-1) * Y[l, m1, m2]^(n - Ceiling[n])]]
```

Figure A.8: Mathematica 8 code used to compute the spherical harmonic expansions of $Y_{l,m_1,m_2}Y_{l',m_1',m_2'}$ and $(Y_{l,m_1,m_2})^n$, $n \in \mathbb{Z}$. (This figure is connected with appendix A.5.)

```
ClearAttributes[Times, Protected];
Πibar[l_, m1_, m2_, s_] * Πibar[lp_, m1p_, m2p_, sp_] :=
  Sum[DS3[j, l, m1, m2, s, lp, m1p, m2p, sp] * Y[j, m1 + m1p, m2 + m2p],
    {j, Abs[l - lp] + Abs[s - sp], l + lp - Abs[s + sp]}]

ClearAttributes[Power, Protected];
Πibar[l_, m1_, m2_, s_]^n_ /; (n == 2 || n == -2) :=
  Module[{sum = 1}, For[i = 0, i < Floor[Abs[n]], i++, sum *= Πibar[l, m1, m2, s]];
    If[n > 0, sum * Πibar[l, m1, m2, s]^(n - Floor[n]),
      (sum^-1) * Πibar[l, m1, m2]^(n - Ceiling[n])]]
```

Figure A.9: Mathematica 8 code used to compute the spherical harmonic expansions of $\Pi^{\bar{i}}_{l,m_1,m_2,s}\Pi^{\bar{j}}_{l',m_1',m_2',s'}$ and $(\Pi^{\bar{i}}_{l,m_1,m_2,s})^n$, $n \in \mathbb{Z}$, where $\Pi^{\bar{i}}_{l,m_1,m_2,s}$ is the S^3 vector spherical harmonic function in the direction $x^{\bar{i}}$. (This figure is linked to appendix A.5.)

```
ClearAttributes[Times, Protected];
Y[l_, m1_, m2_] * Πibar[lp_, m1p_, m2p_, sp_] :=
  -Sum[Sum[(-1)^(m1p - m2p + 2 m1 - 2 m2) * DS3[l, lp, m1p, m2p, sp, j, -m1 - m1p, -m2 -
        m2p, s] * Πibar[j, m1p + m1, m2p + m2, s], {s, {-1, 1}}], {j, 1, l + lp + 2}] +
    Sum[(-1)^(m1p - m2p + 2 m1 - 2 m2) * GS3[l, lp, m1p, m2p, sp, j, -m1 - m1p, -m2 - m2p]
      DelibarY[j, m1p + m1, m2p + m2] / (j (j + 2)), {j, 1, l + lp + 1}]
```

Figure A.10: Mathematica 8 code used to compute the spherical harmonic expansion of $Y_{l,m_1,m_2}\Pi^{\bar{i}}_{l',m_1',m_2',s'}$. (This figure is associated with appendix A.5.)

Bibliography

[1] S. Chunlen, K. Peeters, and M. Zamaklar, "Finite-size effects for jet quenching," `arXiv:1012.4677 [hep-th]`.

[2] S. Chunlen, K. Peeters, P. Vanichchapongjaroen, and M. Zamaklar, "Instability of N=2 gauge theory in compact space with an isospin chemical potential," JHEP **1301** (2013) 035, `arXiv:1210.6188 [hep-th]`.

[3] S. Chunlen, K. Peeters, P. Vanichchapongjaroen, and M. Zamaklar, *"Work in Progress,"*.

[4] P. Jacobs, D. Kharzeev, B. Muller, J. Nagle, K. Rajagopal, et al., "Phases of QCD: Summary of the Rutgers long range plan town meeting, January 12-14, 2007," `arXiv:0705.1930 [nucl-ex]`.

[5] K. Kamikado, N. Strodthoff, L. von Smekal, and J. Wambach, "Fluctuations in the quark-meson model for QCD with isospin chemical potential," Phys.Lett. **B718** (2013) 1044–1053, `arXiv:1207.0400 [hep-ph]`.

[6] V. G. Filev and M. Ihl, "Flavoured Large N Gauge Theory on a Compact Space with an External Magnetic Field," JHEP **1301** (2013) 130, `arXiv:1211.1164 [hep-th]`.

[7] J. M. Maldacena, "The Large N limit of superconformal field theories and supergravity," Adv.Theor.Math.Phys. **2** (1998) 231–252, `arXiv:hep-th/9711200 [hep-th]`.

[8] J. Polchinski, String theory. Vol. 2: Superstring theory and beyond. Cambridge University Press, 2005.

[9] M. F. Sohnius and P. C. West, "Conformal Invariance in N=4 Supersymmetric Yang-Mills Theory," Phys.Lett. **B100** (1981) 245.

[10] S. Mandelstam, "Light Cone Superspace and the Ultraviolet Finiteness of the N=4 Model," Nucl.Phys. **B213** (1983) 149–168.

[11] N. Seiberg, "Supersymmetry and Nonperturbative beta Functions," Phys.Lett. **B206** (1988) 75.

[12] J. Casalderrey-Solana, H. Liu, D. Mateos, K. Rajagopal, and U. A. Wiedemann, "Gauge/String Duality, Hot QCD and Heavy Ion Collisions," arXiv:1101.0618 [hep-th].

[13] P. Petreczky and D. Teaney, "Heavy quark diffusion from the lattice," Phys.Rev. **D73** (2006) 014508, arXiv:hep-ph/0507318 [hep-ph].

[14] D. Banerjee, S. Datta, R. Gavai, and P. Majumdar, "Heavy Quark Momentum Diffusion Coefficient from Lattice QCD," Phys.Rev. **D85** (2012) 014510, arXiv:1109.5738 [hep-lat].

[15] H. B. Meyer, "Transport Properties of the Quark-Gluon Plasma: A Lattice QCD Perspective," Eur.Phys.J. **A47** (2011) 86, arXiv:1104.3708 [hep-lat].

[16] C. Herzog, A. Karch, P. Kovtun, C. Kozcaz, and L. Yaffe, "Energy loss of a heavy quark moving through N=4 supersymmetric Yang-Mills plasma," JHEP **0607** (2006) 013, arXiv:hep-th/0605158 [hep-th].

[17] E. Witten, "Anti-de Sitter space and holography," Adv.Theor.Math.Phys. **2** (1998) 253–291, arXiv:hep-th/9802150 [hep-th].

[18] J. Erdmenger and V. Filev, "Mesons from global Anti-de Sitter space," JHEP **1101** (2011) 119, arXiv:1012.0496 [hep-th].

[19] A. Karch and E. Katz, "Adding flavor to AdS / CFT," JHEP **0206** (2002) 043, arXiv:hep-th/0205236 [hep-th].

[20] A. O'Bannon, "Holographic Thermodynamics and Transport of Flavor Fields," `arXiv:0808.1115 [hep-th]`.

[21] J. M. Maldacena, "Wilson loops in large N field theories," Phys.Rev.Lett. **80** (1998) 4859–4862, `arXiv:hep-th/9803002 [hep-th]`.

[22] S.-J. Rey and J.-T. Yee, "Macroscopic strings as heavy quarks in large N gauge theory and anti-de Sitter supergravity," Eur.Phys.J. **C22** (2001) 379–394, `arXiv:hep-th/9803001 [hep-th]`.

[23] S.-J. Rey, S. Theisen, and J.-T. Yee, "Wilson-Polyakov loop at finite temperature in large N gauge theory and anti-de Sitter supergravity," Nucl.Phys. **B527** (1998) 171–186, `arXiv:hep-th/9803135 [hep-th]`.

[24] A. Brandhuber, N. Itzhaki, J. Sonnenschein, and S. Yankielowicz, "Wilson loops in the large N limit at finite temperature," Phys.Lett. **B434** (1998) 36–40, `arXiv:hep-th/9803137 [hep-th]`.

[25] U. H. Danielsson, E. Keski-Vakkuri, and M. Kruczenski, "Vacua, propagators, and holographic probes in AdS / CFT," JHEP **9901** (1999) 002, `arXiv:hep-th/9812007 [hep-th]`.

[26] A. M. Polyakov, "Quantum Geometry of Bosonic Strings," Phys.Lett. **B103** (1981) 207–210.

[27] J. Polchinski, String theory. Vol. 1: An introduction to the bosonic string. Cambridge University Press, 2005.

[28] C. V. Johnson, "D-brane primer," `arXiv:hep-th/0007170 [hep-th]`.

[29] A. A. Tseytlin, "On nonAbelian generalization of Born-Infeld action in string theory," Nucl.Phys. **B501** (1997) 41–52, `arXiv:hep-th/9701125 [hep-th]`.

[30] A. Sevrin, J. Troost, and W. Troost, "The nonAbelian Born-Infeld action at order F**6," Nucl.Phys. **B603** (2001) 389–412, `arXiv:hep-th/0101192 [hep-th]`.

[31] P. Di Vecchia, A. Liccardo, R. Marotta, and F. Pezzella, "Gauge / gravity correspondence from open / closed string duality," JHEP **0306** (2003) 007, `arXiv:hep-th/0305061 [hep-th]`.

[32] G. T. Horowitz and A. Strominger, "Black strings and P-branes," Nucl.Phys. **B360** (1991) 197–209.

[33] J. Erdmenger, N. Evans, I. Kirsch, and E. Threlfall, "Mesons in Gauge/Gravity Duals - A Review," Eur.Phys.J. **A35** (2008) 81–133, `arXiv:0711.4467 [hep-th]`.

[34] G. 't Hooft, "Dimensional reduction in quantum gravity," `arXiv:gr-qc/9310026 [gr-qc]`.

[35] S. Gubser, I. R. Klebanov, and A. M. Polyakov, "Gauge theory correlators from noncritical string theory," Phys.Lett. **B428** (1998) 105–114, `arXiv:hep-th/9802109 [hep-th]`.

[36] V. G. Filev, "Aspects of the Holographic Study of Flavor Dynamics," `arXiv:0809.4701 [hep-th]`.

[37] D. Z. Freedman, S. D. Mathur, A. Matusis, and L. Rastelli, "Correlation functions in the CFT(d) / AdS(d+1) correspondence," Nucl.Phys. **B546** (1999) 96–118, `arXiv:hep-th/9804058 [hep-th]`.

[38] S. Lee, S. Minwalla, M. Rangamani, and N. Seiberg, "Three point functions of chiral operators in D = 4, N=4 SYM at large N," Adv.Theor.Math.Phys. **2** (1998) 697–718, `arXiv:hep-th/9806074 [hep-th]`.

[39] E. Witten, "Anti-de Sitter space, thermal phase transition, and confinement in gauge theories," Adv.Theor.Math.Phys. **2** (1998) 505–532, `arXiv:hep-th/9803131 [hep-th]`.

[40] S. Gubser, I. R. Klebanov, and A. Peet, "Entropy and temperature of black 3-branes," Phys.Rev. **D54** (1996) 3915–3919, `arXiv:hep-th/9602135 [hep-th]`.

[41] S. Hawking and D. N. Page, "Thermodynamics of Black Holes in anti-De Sitter Space," Commun.Math.Phys. **87** (1983) 577.

[42] M. Grana and J. Polchinski, "Gauge / gravity duals with holomorphic dilaton," Phys.Rev. **D65** (2002) 126005, `arXiv:hep-th/0106014 [hep-th]`.

[43] M. Bertolini, P. Di Vecchia, M. Frau, A. Lerda, and R. Marotta, "N=2 gauge theories on systems of fractional D3/D7 branes," Nucl.Phys. **B621** (2002) 157–178, `arXiv:hep-th/0107057 [hep-th]`.

[44] C. Johnson, D-branes. Cambridge University Press, 2003.

[45] K. Becker, M. Becker, and J. Schwarz, String theory and M-theory: A modern introduction. Cambridge University Press, 2007.

[46] E. Bergshoeff, E. Eyras, R. Halbersma, J. van der Schaar, C. Hull, et al., "Space-time filling branes and strings with sixteen supercharges," Nucl.Phys. **B564** (2000) 29–59, `arXiv:hep-th/9812224 [hep-th]`.

[47] A. Karch, A. O'Bannon, and K. Skenderis, "Holographic renormalization of probe D-branes in AdS/CFT," JHEP **0604** (2006) 015, `arXiv:hep-th/0512125 [hep-th]`.

[48] A. Karch and A. O'Bannon, "Chiral transition of N=4 super Yang-Mills with flavor on a 3-sphere," Phys.Rev. **D74** (2006) 085033, `arXiv:hep-th/0605120 [hep-th]`.

[49] C. Fefferman and C. R. Graham, "Conformal Invariants," Astrisque Numero Hors Serie (1985) 95–116.

[50] A. Karch, A. O'Bannon, and L. G. Yaffe, "Critical Exponents from AdS/CFT with Flavor," JHEP **0909** (2009) 042, `arXiv:0906.4959 [hep-th]`.

[51] **BRAHMS Collaboration** Collaboration, I. Arsene et al., "Quark gluon plasma and color glass condensate at RHIC? The Perspective from the BRAHMS experiment," Nucl.Phys. **A757** (2005) 1–27, `arXiv:nucl-ex/0410020 [nucl-ex]`.

[52] **PHENIX Collaboration** Collaboration, K. Adcox et al., "Formation of dense partonic matter in relativistic nucleus-nucleus collisions at RHIC: Experimental evaluation by the PHENIX collaboration," Nucl.Phys. **A757** (2005) 184–283, `arXiv:nucl-ex/0410003 [nucl-ex]`.

[53] B. Back, M. Baker, M. Ballintijn, D. Barton, B. Becker, et al., "The PHOBOS perspective on discoveries at RHIC," Nucl.Phys. **A757** (2005) 28–101, `arXiv:nucl-ex/0410022 [nucl-ex]`.

[54] **STAR Collaboration** Collaboration, J. Adams et al., "Experimental and theoretical challenges in the search for the quark gluon plasma: The STAR Collaboration's critical assessment of the evidence from RHIC collisions," Nucl.Phys. **A757** (2005) 102–183, `arXiv:nucl-ex/0501009 [nucl-ex]`.

[55] A. Mischke, "Overview on heavy flavour measurements in lead-lead collisions at the CERN-LHC," `arXiv:1301.7550 [hep-ex]`.

[56] S. S. Gubser, "Drag force in AdS/CFT," Phys.Rev. **D74** (2006) 126005, `arXiv:hep-th/0605182 [hep-th]`.

[57] M. Kruczenski, L. A. Pando Zayas, J. Sonnenschein, and D. Vaman, "Regge trajectories for mesons in the holographic dual of large-N(c) QCD," JHEP **0506** (2005) 046, `arXiv:hep-th/0410035 [hep-th]`.

[58] A. Nata Atmaja and K. Schalm, "Anisotropic Drag Force from 4D Kerr-AdS Black Holes," JHEP **1104** (2011) 070, `arXiv:1012.3800 [hep-th]`.

[59] G. Gibbons, M. Perry, and C. Pope, "The First law of thermodynamics for Kerr-anti-de Sitter black holes," Class.Quant.Grav. **22** (2005) 1503–1526, `arXiv:hep-th/0408217 [hep-th]`.

[60] I.-D. Chang, "On the wall effect correction of the Stokes drag formula for axially symmetric bodies moving inside a cylindrical tube," Z. Ang. Math. Phys. **12** (1961) 6–14.

[61] D. Song and R. K. Gupta, "Wall Effects on a Sphere Falling in Quiescent Power Law Fluids in Cylindrical Tubes," Ind. Eng. Chem. Res. **48** (2009) 5845–5856.

[62] Q. Zhang, "Constraints on the size of the quark gluon plasma," `arXiv:hep-ph/0106242 [hep-ph]`.

[63] A. Ayala, E. Cuautle, J. Magnin, L. M. Montano, and A. Raya, "Finite size effects on pion spectra in relativistic heavy-ion collisions," Phys.Lett. **B634** (2006) 200–204, `arXiv:hep-ph/0510233 [hep-ph]`.

[64] A. Ayala, E. Cuautle, J. Magnin, and L. M. Montano, "Proton and pion transverse spectra at RHIC from radial flow and finite size effects," Phys.Rev. **C74** (2006) 064903, `arXiv:nucl-th/0603039 [nucl-th]`.

[65] S. P. Kumar, "Spinning flavour branes and fermion pairing instabilities," Phys.Rev. **D84** (2011) 026003, `arXiv:1104.1405 [hep-th]`.

[66] O. Aharony, K. Peeters, J. Sonnenschein, and M. Zamaklar, "Rho meson condensation at finite isospin chemical potential in a holographic model for QCD," JHEP **0802** (2008) 071, `arXiv:0709.3948 [hep-th]`.

[67] S. Kobayashi, D. Mateos, S. Matsuura, R. C. Myers, and R. M. Thomson, "Holographic phase transitions at finite baryon density," JHEP **0702** (2007) 016, `arXiv:hep-th/0611099 [hep-th]`.

[68] J. Erdmenger, M. Kaminski, P. Kerner, and F. Rust, "Finite baryon and isospin chemical potential in AdS/CFT with flavor," JHEP **0811** (2008) 031, `arXiv:0807.2663 [hep-th]`.

[69] R. C. Myers, "Dielectric branes," JHEP **9912** (1999) 022, `arXiv:hep-th/9910053 [hep-th]`.

[70] M. Ammon, J. Erdmenger, M. Kaminski, and P. Kerner, "Flavor Superconductivity from Gauge/Gravity Duality," JHEP **0910** (2009) 067, `arXiv:0903.1864 [hep-th]`.

[71] M. Kruczenski, D. Mateos, R. C. Myers, and D. J. Winters, "Meson spectroscopy in AdS / CFT with flavor," JHEP **0307** (2003) 049, `arXiv:hep-th/0304032 [hep-th]`.

[72] M. Ammon, J. Erdmenger, M. Kaminski, and P. Kerner, "Superconductivity from gauge/gravity duality with flavor," Phys.Lett. **B680** (2009) 516–520, `arXiv:0810.2316 [hep-th]`.

[73] K. Peeters, J. Powell, and M. Zamaklar, "Exploring colourful holographic superconductors," JHEP **0909** (2009) 101, `arXiv:0907.1508 [hep-th]`.

[74] T. Matsuo, D. Tomino, and W.-Y. Wen, "Drag force in SYM plasma with B field from AdS/CFT," JHEP **0610** (2006) 055, `arXiv:hep-th/0607178 [hep-th]`.

[75] V. G. Filev, C. V. Johnson, R. Rashkov, and K. Viswanathan, "Flavoured large N gauge theory in an external magnetic field," JHEP **0710** (2007) 019, `arXiv:hep-th/0701001 [hep-th]`.

[76] A. Karch and A. O'Bannon, "Metallic AdS/CFT," JHEP **0709** (2007) 024, `arXiv:0705.3870 [hep-th]`.

[77] A. O'Bannon, "Hall Conductivity of Flavor Fields from AdS/CFT," Phys.Rev. **D76** (2007) 086007, `arXiv:0708.1994 [hep-th]`.

[78] T. Albash, V. G. Filev, C. V. Johnson, and A. Kundu, "Finite temperature large N gauge theory with quarks in an external magnetic field," JHEP **0807** (2008) 080, `arXiv:0709.1547 [hep-th]`.

[79] J. Erdmenger, R. Meyer, and J. P. Shock, "AdS/CFT with flavour in electric and magnetic Kalb-Ramond fields," JHEP **0712** (2007) 091, `arXiv:0709.1551 [hep-th]`.

[80] V. Gusynin, V. Miransky, and I. Shovkovy, "Catalysis of dynamical flavor symmetry breaking by a magnetic field in (2+1)-dimensions," Phys.Rev.Lett. **73** (1994) 3499–3502, `arXiv:hep-ph/9405262 [hep-ph]`.

[81] V. Gusynin, V. Miransky, and I. Shovkovy, "Dimensional reduction and dynamical chiral symmetry breaking by a magnetic field in (3+1)-dimensions," Phys.Lett. **B349** (1995) 477–483, `arXiv:hep-ph/9412257 [hep-ph]`.

[82] D. K. Hong, Y. Kim, and S.-J. Sin, "RG analysis of magnetic catalysis in dynamical symmetry breaking," Phys.Rev. **D54** (1996) 7879–7883, `arXiv:hep-th/9603157 [hep-th]`.

[83] K. Klimenko, "Three-dimensional Gross-Neveu model in an external magnetic field," Theor.Math.Phys. **89** (1992) 1161–1168.

[84] K. Klimenko, "Three-dimensional Gross-Neveu model at nonzero temperature and in an external magnetic field," Z.Phys. **C54** (1992) 323–330.

[85] K. Klimenko, "Three-dimensional Gross-Neveu model at nonzero temperature and in an external magnetic field," Theor.Math.Phys. **90** (1992) 1–6.

[86] A. Ballon-Bayona, K. Peeters, and M. Zamaklar, "A chiral magnetic spiral in the holographic Sakai-Sugimoto model," JHEP **1211** (2012) 164, `arXiv:1209.1953 [hep-th]`.

[87] M. Ammon, J. Erdmenger, P. Kerner, and M. Strydom, "Black Hole Instability Induced by a Magnetic Field," Phys.Lett. **B706** (2011) 94–99, `arXiv:1106.4551 [hep-th]`.

[88] J. Stoer and R. Bulirsch, Introduction to Numerical Analysis. Springer-Verlag, New York, 1980.

[89] K.-j. Hamada and S. Horata, "Conformal algebra and physical states in noncritical three-brane on R x S**3," Prog.Theor.Phys. **110** (2004) 1169–1210, `arXiv:hep-th/0307008 [hep-th]`.